RHIC Beam Use Request For Runs 18 and 19

The STAR Collaboration

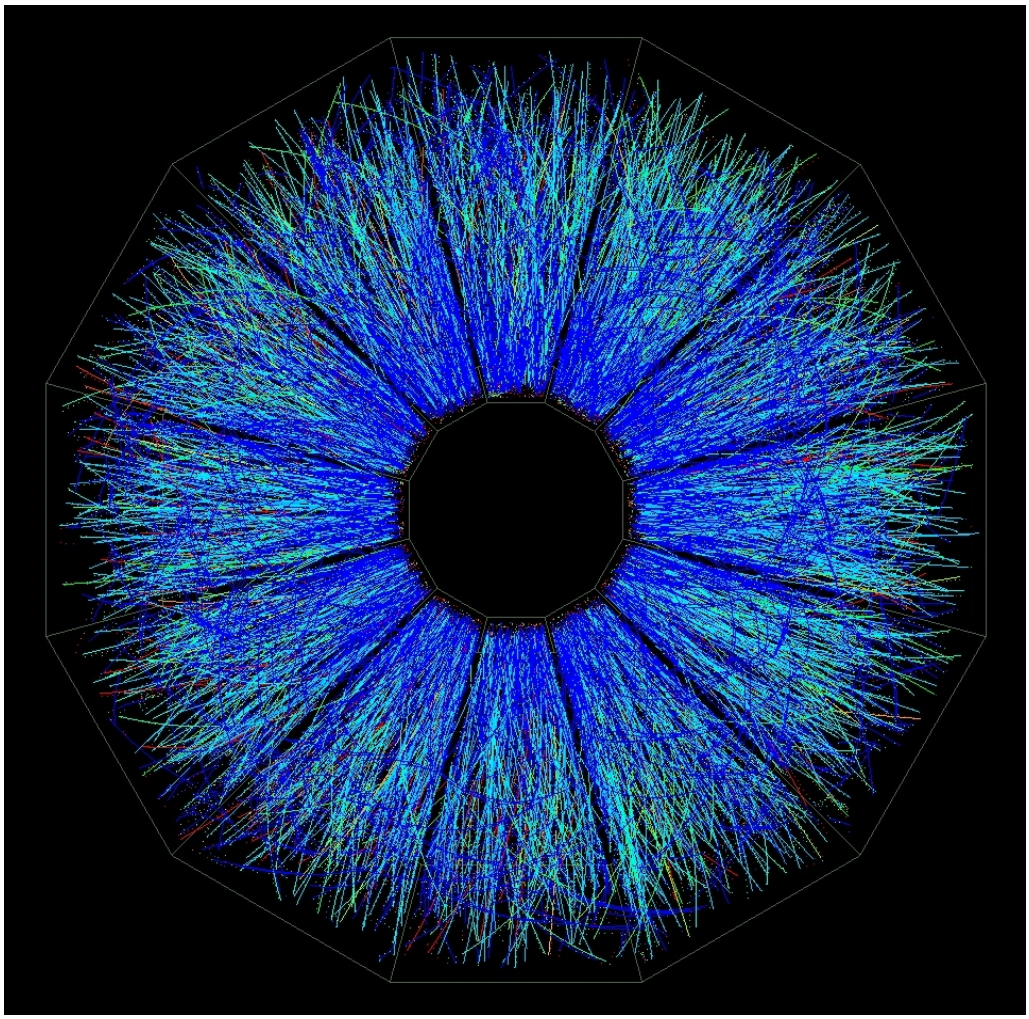

May 15, 2017

Executive Summary

This Beam Use Request from the STAR collaboration for RHIC Runs 18 and 19 is focused on two compelling programs that are key to the completion of the RHIC mission. In Run 18 Isobaric collisions will provide enhanced clarity as to the role of the magnetic field in the charge separation measurements. While for Run 19 STAR proposes to embark on the NSAC endorsed Beam Energy Scan II (BES-II) program which will dramatically enhance our understanding of the QCD phase diagram.

STAR's **highest scientific priority for Run 18** is the successful realization of the isobaric collision program. We are requesting two 3.5 week runs with collisions of Ruthenium-96 (Ru+Ru) and Zirconium-96 (Zr+Zr) at $\sqrt{s_{NN}} = 200$ GeV. Comparison of results from these events will help clarify the interpretation of measurements related to the chiral magnetic effect. Since Ru nuclei have an atomic charge of 44 compared to 40 for Zr, Ru+Ru collisions will generate a magnetic field approximately 10% larger than Zr+Zr collisions while all else remains essentially constant. Comparison of charge separation results will aid in determining the fraction of those measurements which are related to the chiral magnetic effect by isolating the magnetic field dependence. Our understanding of the chiral magnetic effect will thereby be greatly advanced and have a fundamental impact beyond the field of high-temperature QCD.

STAR's *second highest priority for Run 18* is Au+Au collisions at $\sqrt{s_{NN}} = 27$ GeV to allow for statistically significant Λ and $\bar{\Lambda}$ global polarization measurements. These measurements will take advantage of the newly installed Event Plane Detector's improved first-order reaction plane resolution.

STAR's *third highest priorities for Run 18* are Au+Au collisions at $\sqrt{s_{NN}} = 3.2$ GeV in "fixed target" mode. $\sqrt{s_{NN}} = 3.2$ GeV running will allow for a statistically significant measurement of Kurtosis at a collision energy between the HADES measurement at 2.4 GeV and STAR's lowest energy point at 7.7 GeV. This energy is accessible, and being pursued, by other international experiments, BM@N in 2019 and CBM in 2025, making a timely measurement imperative.

STAR's **highest scientific priority for Run 19** is the commencement of the RHIC Beam Energy Scan II.

Three upgrades are planned for completion prior to the BES-II. Both the inner Time Projection Chamber (iTPC) and the endcap Time of Flight (eTOF) are on schedule for full installation in Run 19; increasing the rapidity and low transverse momentum acceptance of STAR, and extending our particle identification capabilities. The event plane detector (EPD) will be fully installed for Run 18 after completing a commissioning run this year. The EPD provides enhanced event plane resolution and forward centrality measurements.

Table 1 summarizes our request for Run 18 assuming 15 cryo-weeks. Table 2 and Table 3 summarize the request for the start of the BES-II program considering two scenarios:

- Scenario 1: 24 cryo-weeks in 2019
- Scenario 2: 20 cryo-weeks from a combined run during 2019-2020

For both scenarios we assume another RHIC run occurs to allow the completion of the BES-II. Table 4 outlines the dataset STAR currently plans to collect at that time. Collection of these data will allow us to achieve our high impact physics goals on a timescale consistent with the current intense international interest while utilizing RHIC beams effectively and taking full advantage of intended improvements in machine and detector capabilities.

Table 1: Beam Use Request for Run 18 assuming 15 cryo-weeks of running (including 2 weeks for the Coherent electron Cooling test).

Beam Energy (GeV/nucleon)	$\sqrt{s_{NN}}$ (GeV)	Run Time	Species	Number Events	Priority	Sequence
100	200	3.5 weeks	Ru+Ru	1.2B MB	1	1
100	200	3.5 weeks	Zr+Zr	1.2B MB	1	2
13.5	27	3 weeks	Au+Au	1B MB	2	3
3.85	3.0 (FXT)	2 days	Au+Au	100M MB	3	4

Table 2: Beam Use Request for Run 19 assuming 24 cryo-weeks of running. We assume that the commissioning of the low-energy electron cooling will be complete by the end of the first half of the run period and perform at its design for 11.5 GeV collisions in the later period of the Run 19. A possible option is to take half of the dataset at 9.1 GeV or extend the 11.5 GeV dataset running time if cooling is not yet at design performance. We are also assessing possible isobar data-taking at a lower energy depending on the outcoming of Au+Au at 27 GeV and isobar low energy test in Run 18. We could also run Au+Au collisions at $\sqrt{s_{NN}} = 16.7$ GeV, to search for possible critical behavior assuming a narrow critical region between 14.5 and 19.6 GeV.

Beam Energy (GeV/nucleon)	$\sqrt{s_{NN}}$ (GeV)	Run Time	Species	Number Events	Priority	Sequence
9.8	19.6	4.5 weeks	Au+Au	400M MB	1	1
7.3	14.5	5.5 weeks	Au+Au	300M MB	1	3
5.75	11.5	5 weeks	Au+Au	230M MB	1	5
4.6	9.1 [1]	4 weeks	Au+Au	160M MB	1	7
9.8	4.5 (FXT)	2 days	Au+Au	100M MB	2	2
7.3	3.9 (FXT)	2 days	Au+Au	100M MB	2	4
5.75	3.5 (FXT)	2 days	Au+Au	100M MB	2	6
31.2	7.7 (FXT)	2 days	Au+Au	100M MB	2	8
19.5	6.2 (FXT)	2 days	Au+Au	100M MB	2	9
13.5	5.2 (FXT)	2 days	Au+Au	100M MB	2	10

This BUR document is outlined as follows: first, as requested, in Section 1 we report highlights from analyses completed since the last PAC meeting, with a focus on data from

[1]The complete request is for 160M MB events and will take 9.5 weeks to collect assuming design cooling performance. The remainder of the data will be collected in the second BES-II run.

Table 3: Beam Use Request for a combined Run 19+20 assuming 20 cryo-weeks of running.

Beam Energy (GeV/nucleon)	$\sqrt{s_{NN}}$ (GeV)	Run Time	Species	Number Events	Priority	Sequence
9.8	19.6	4.5 weeks	Au+Au	400M MB	1	1
7.3	14.5	5.5 weeks	Au+Au	300M MB	1	3
5.75	11.5	5 weeks	Au+Au	230M MB	1	5
9.8	4.5 (FXT)	2 days	Au+Au	100M MB	2	2
7.3	3.9 (FXT)	2 days	Au+Au	100M MB	2	4
5.75	3.5 (FXT)	2 days	Au+Au	100M MB	2	6
31.2	7.7 (FXT)	2 days	Au+Au	100M MB	2	7
19.5	6.2 (FXT)	2 days	Au+Au	100M MB	2	8
13.5	5.2 (FXT)	2 days	Au+Au	100M MB	2	9

Table 4: Plans for Run 20 or Run 21 assuming 24 cryo-weeks of running.

Beam Energy (GeV/nucleon)	$\sqrt{s_{NN}}$ (GeV)	Run Time	Species	Number Events	Priority	Sequence
4.6	9.1[1]	9.5 weeks	Au+Au	160M MB	1	1
3.85	7.7	12 weeks	Au+Au	100M MB	1	2
3.85	3.0 (FXT)	2 days	Au+Au	100M MB	2	3

Runs 14-16. Sections 2 and 3 detail the STAR Collaboration's physics program which motivates our Run 18 and Run 19 beam use request. Next in Section 4 we outline the status of the upgrades intended for Runs 18 and 19. Finally, in Section 5 we provide a short summary of the status of our data production and plans that will ensure that data collected in Runs 18 and 19 are produced in a timely manner and stored in a cost-efficient fashion.

Contents

1 Highlights from STAR Program

Since the last Beam Use Request and PAC meeting in June of 2016, STAR has published, or had accepted for publication, 11 papers in refereed journals: Nature (1), Physics Review Letters (2), Physics Letters B (3) and others (5). Another 6 papers have been submitted for publication and we are awaiting the editors decision. In addition, STAR collaborators have made numerous contributions at conferences and workshops presenting preliminary results, including more than 60 talks and posters at SPIN16, DIS17, SQM16, HP2016, and QM2017.

Below highlights from these publications and preliminary analyses are presented, first those from the Spin and Cold QCD program and then from the heavy-ion program.

1.1 STAR Spin Highlights

The STAR spin physics program seeks to advance our understanding of the spin and flavor structure of the proton in terms of its constituent quarks and gluons, exploiting the unique capability of RHIC to provide longitudinally and transversely polarized p+p collisions at multiple collision energies. Using longitudinally polarized beams, one can probe the helicity preferences of the gluons and of up and down (anti-)quarks, to determine the contribution of each to the total spin of the proton. With spins transverse to their momentum direction, the p+p collisions exhibit kinematic and dynamical effects that are directly sensitive to quark transversity and partonic motion within the proton. This program is complemented by studies of polarized p+p elastic scattering and central exclusive production, in which a far-forward proton is detected intact.

Since 2009 RHIC STAR has completed several highly successful polarized p+p runs both at $\sqrt{s} = 200$ GeV and $\sqrt{s} = 510$ GeV. The STAR sampled luminosity and the luminosity averaged beam polarization as measured by the H-jet polarimeter are summarized in Table 5. These data sets formed the basis for papers and new preliminary results, which are highlighted in the following sections.

Year	$\sqrt{s}$ (GeV)	Recorded Luminosity (pb^{-1})	Spin Orientation	$B/Y < Pol >$
2009	200	25	longitudinal	55
2009	500	10	longitudinal	39
2011	500	12	longitudinal	48
2011	500	25	transverse	48
2012	200	22	transverse	61/56
2012	510	82	longitudinal	50/53
2013	510	300	longitudinal	51/52
2015	200	52	longitudinal	53/57
2015	200	52	transverse	53/57
2017	500	280	transverse	55/55

Table 5: Center-of-mass energy, integrated luminosity collected at STAR and average beam polarizations from the H-jet polarimeter for recent p+p running periods at RHIC. Run 17 numbers are the projected goals.

1.1.1 Longitudinal Spin Program

Since the last PAC meeting the STAR spin-working group has published one longitudinal spin paper in Rapid Communications Physical Review D [1]. This paper presents the di-jet cross-section and double spin asymmetry, A_{LL}, extracted from 21 pb^{-1} of $\sqrt{s}$ = 200 GeV longitudinally polarized p+p collisions collected in Run 9. This is the first mid-rapidity di-jet analysis to be published by STAR and the results support the previously published inclusive jet analysis which showed gluon polarization to be at the level of 0.2 in the region x > 0.05. Figure 1 shows the particle level di-jet differential cross-section and A_{LL}.

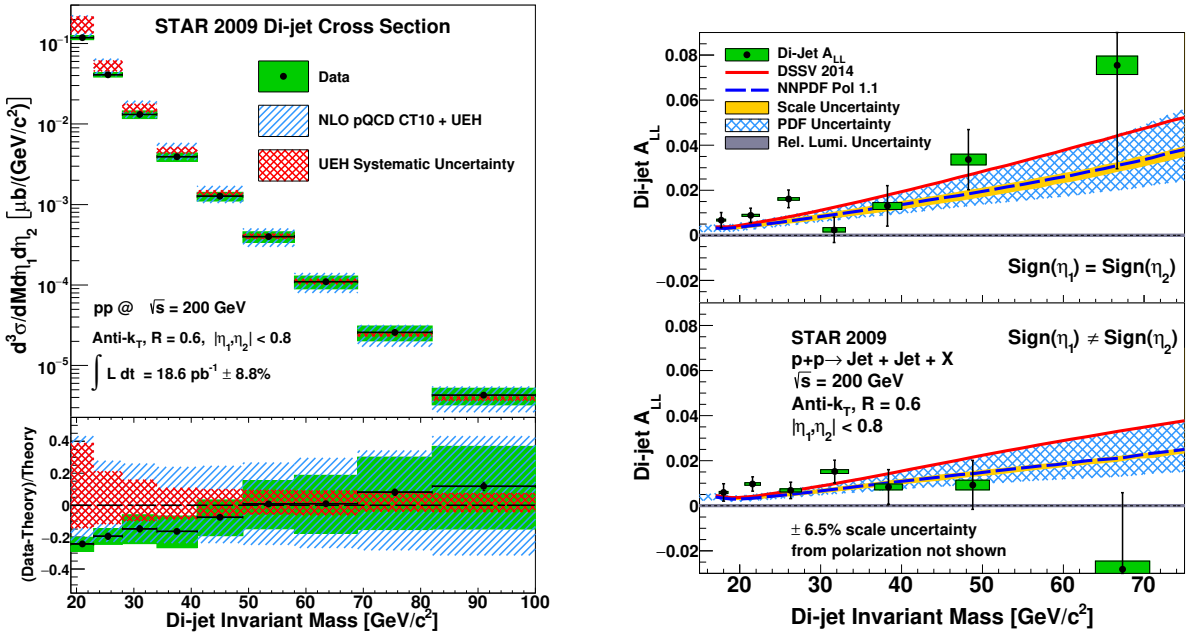

Figure 1: Di-jet cross section (left) and double helicity asymmetry (right) as function of invariant mass at $\sqrt{s}$ = 200 GeV.

While inclusive channels maximize statistical power, they do not permit event-by-event reconstruction of the underlying partonic kinematics in p+p collisions. Instead they sample an x range amounting to a fraction of the total integral $\Delta G(Q^2)$ and provide only coarse constraints on the functional form of the underlying shape of $\Delta g(x, Q^2)$, which in turn produces a large theoretical uncertainty in the determination of the total integral. The x dependence can be mapped via correlation measurements, such as di-jets. At leading order it is possible to determine the kinematics, such as the momentum fraction of the colliding partons, from the invariant mass of the di-jet pair (M_{inv}) and pseudorapidity of the individual jets. At low x<0.05, the gluon polarization $\Delta g(x, Q^2)$ is largely unconstrained by experimental data and in an effort to extend our knowledge to smaller x, STAR is using the Endcap Electromagnetic Calorimeter to push di-jet reconstruction into the forward region ($1 < \eta < 2$). The first forward di-jet A_{LL}, reconstructed from one jet at mid-rapidity and one at forward rapidity, was given preliminary release for the 22^{nd} International Spin Symposium in the fall of 2016 (SPIN16). Figure 2 shows the forward di-jet A_{LL} corrected back to the particle level. The data show good agreement with theoretical asymmetries extracted from the DSSV [2] and NNPDF [3] NLO QCD global analyses.

The STAR spin working group also released the W$^{\pm}$ longitudinal single spin (A_L) asymmetries from the high statistics of Run 13 at $\sqrt{s}$ = 510 GeV. Figure 3 plots these pre-

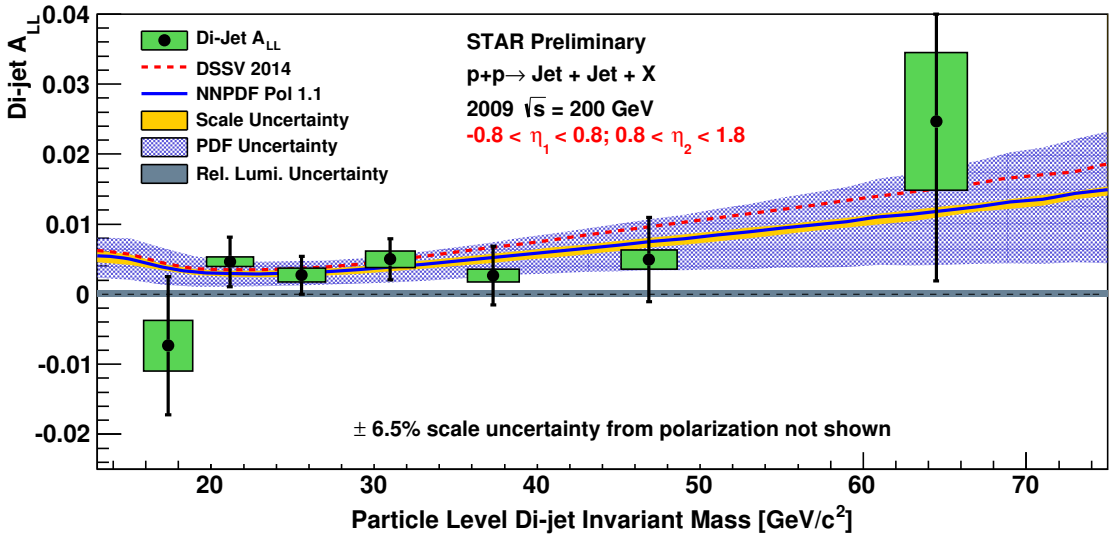

Figure 2: Double helicity asymmetries in di-jet production at moderately forward pseudorapidities as function of invariant mass [4].

liminary results (red circles), along with the published Run 11+12 results (black squares) [5], as a function of the pseudorapidity of the decay $e^{\pm}$. The most recent results agree with the published asymmetries, again showing increased W^- asymmetries compared to the central value of DSSV fits to semi-inclusive and inclusive data. Recent fits from the DSSV [6] and NNPDF [3] global analyses that incorporate the published results demonstrate the significant constraints these data place on the $\bar{u}$ and $\bar{d}$ quark helicity distributions. Compared to the Run 11+12 results the statistical uncertainty on the recently released data is reduced by 40% and is expected to place the tightest constraints to date on the $\bar{u}$ and $\bar{d}$ distributions.

1.1.2 Transverse Spin Program

STAR has released new preliminary results of the transverse spin transfer, D_{TT}, of Λ and $\bar{\Lambda}$ hyperons from transversely polarized p+p collisions at $\sqrt{s} = 200$ GeV in Run 12 with an integrated luminosity of 18 pb^{-1}. The $\Lambda(\bar{\Lambda})$ D_{TT} measurements provide unique access to the virtually unconstrained s($\bar{s}$) quark transversity and spin dependent fragmentation distributions in a collinear factorization framework. This is the first observation of Λ spin transfer in proton collisions at midrapidity ($|\eta| < 1.2$) with transverse momenta up to 8 GeV/c [7]. The results, as shown in Fig. 4, of hyperons and anti-hyperons are so far consistent with zero. In the analysis, the Λ hyperons are reconstructed through their weak decay into protons and pions ($\Lambda \rightarrow p + \pi^-$, $\bar{\Lambda} \rightarrow \bar{p} + \pi^+$) and the direction of reconstructed jets is used as a proxy for the quark direction, which is needed to determine the hyperon polarization direction. The hyperon polarization is then calculated from the azimuthal modulation of the decay products in the Λ rest frame, similar to [8], such that acceptance effects are canceled. Asymmetries are corrected for background contributions determined from sidebands below and above the Λ mass peak. Systematic uncertainties include the uncertainty of the decay parameter, α_Λ, the relative luminosity, pile-up effects, and the trigger bias. Relative luminosity is the main contribution at low p_T, the trigger

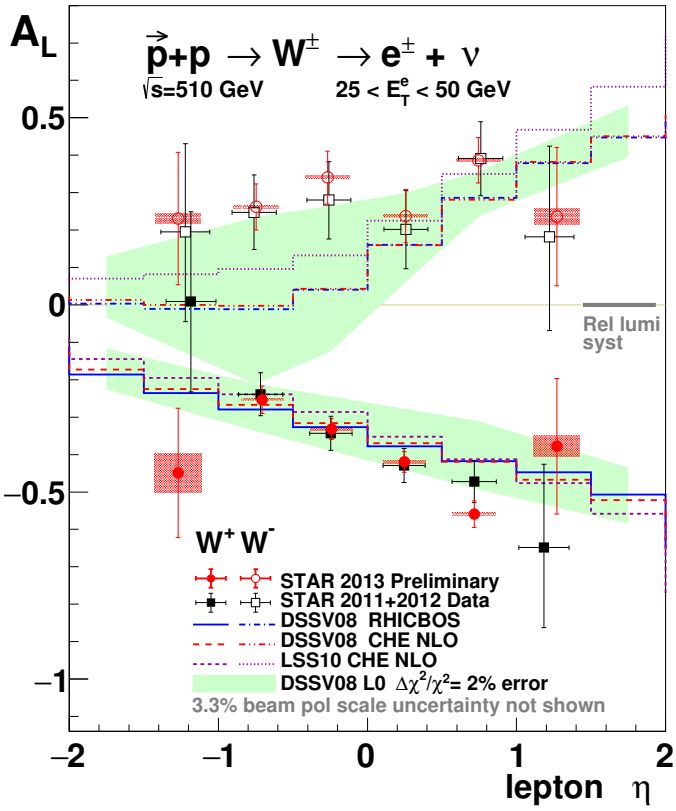

Figure 3: Parity violating single spin asymmetry A_L of $W^{\pm}$ bosons as function of pseudorapidity from Run 11+12 and Run 13.

bias dominates at high p_T.

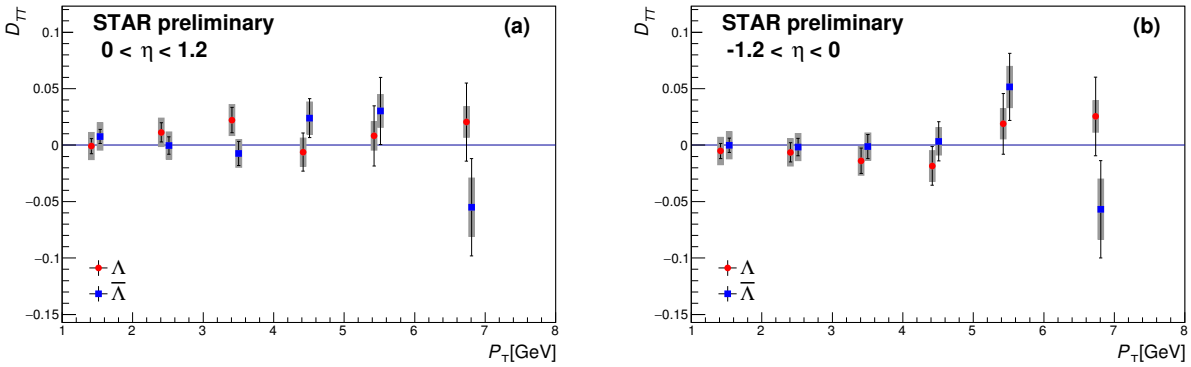

Figure 4: The transverse spin transfer D_{TT} as function of p_T for Λ and $\bar{\Lambda}$ (a) at forward ($\eta > 0$) and (b) at backward ($\eta < 0$) directions with respect to the polarized beam. $\bar{\Lambda}$ points have been shifted in p_T for clarity.

1.1.3 Status of Run 17

The major goals for the current Run 17 are the transverse single spin asymmetries of $W^{\pm}/Z^0$-bosons at midrapidity as well as Drell-Yan and direct photon production at forward rapidity. The BUR for 400 pb^{-1} of delivered luminosity with an average beam polarization of 55%, driven by the small cross sections for $W^{\pm}/Z^0$-boson and Drell-Yan production, allows for a decisive measurement of the sign change of the Sivers effect as compared to existing data from semi-inclusive deep inelastic scattering. These measurements are highly anticipated especially in the context of recently released final results of

pion induced Drell-Yan production from the COMPASS experiment [9]. The COMPASS results, shown in Fig. 5 agree at the 2σ level with the predicted sign change and are consistent with the previously published STAR results[10], also shown in Fig. 5. In addition, STAR will provide observables at different Q^2 scales from direct photons and medium mass Drell-Yan ($4 < M_{inv} < 9$ GeV/c^2) to the very high masses of the $W^{\pm}/Z^0$-bosons. In this approach, the reconstruction of the Z^0 at midrapidity is virtually background free and does not require additional information from Monte Carlo simulations.

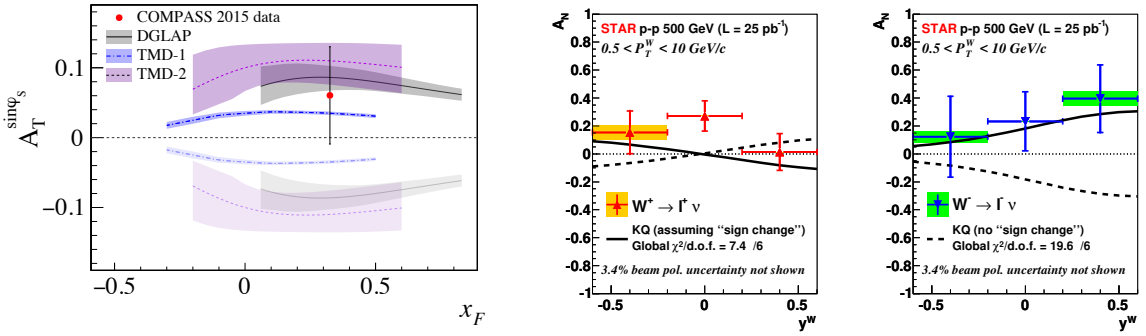

Figure 5: The COMPASS Sivers asymmetry (left) plotted with theoretical predictions for different Q^2 evolution schemes. The dark-shaded (light-shaded) predictions are evaluated with (without) the sign-change hypothesis. The error bar represents the total experimental uncertainty. Transverse single-spin asymmetry amplitude for W^+ (middle) and W^- (right) vs $y^{W^{\pm}}$ as measured by STAR in p+p collisions at $\sqrt{s} = 500$ GeV. The $W^{\pm}$ boson asymmetries are compared with the non TMD-evolved KQ model[11], assuming (solid line) or excluding (dashed line) a sign change in the Sivers function.

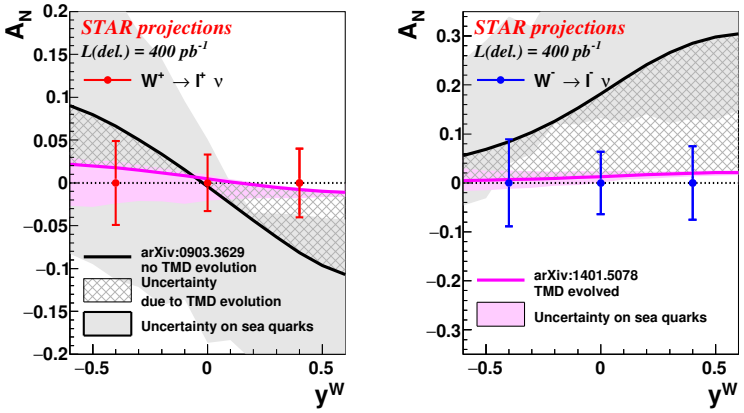

Figure 6: The projected uncertainties for transverse single spin asymmetries of W- bosons as a function of rapidity for a delivered integrated luminosity of 400 pb^{-1} and an average beam polarisation of 55%. The projections are compared to theoretical predictions with (pink) and without (black) TMD evolution included. The solid light gray and pink bands represent the uncertainty on the KQ [11] and EIKV [12] results, respectively, due to the unknown sea-quark Sivers function. The crosshatched dark grey region indicates the current uncertainty in the theoretical predictions due to TMD evolution.

The Run 17 $W^{\pm}/Z^0$-program relies on a calorimeter trigger with high energies in single towers, BHT3/EHT2. From existing Run 13 data, it has been shown that the

reconstruction efficiency with a modified tracking algorithm is optimal at luminosities around $1.5 \cdot 10^{32}\text{cm}^{-2}\text{s}^{-1}$. After reaching the required luminosity, the RHIC collider has achieved a leveling of the collision rate around the best value by adjusting the β^* function at STAR during a fill. With stable beam polarizations, measured with the hydrogen jet polarimeter, the goal for the recorded figure of merit in Run 17 was reached on May 14 as shown in the projections in Figure 6. Using a preliminary calibration of the TPC and only a first pass of the EMC QA, the reconstruction efficiency has been confirmed in the fast offline production and the number of $W^{\pm}$-bosons is within the expected range. The data provided by Run 17 are essential input for the framework of Q^2 evolution of transverse momentum dependent parton distribution functions.

The Drell-Yan and direct photon measurements are based on the forward calorimeter, FMS, which has been equipped with an additional preshower, FPS (already in Run 15), and a postshower, FPOST. These new detectors are scintillator hodoscopes with a granularity that matches the FMS. FPS and FPOST each consist of about 240 channels that allow a spacial correlation with the FMS clusters in x and y direction. Scintillators are 1 cm thick and read out with SiPM sensors. The FPOST was commissioned before the start of Run 17. Radiation damage, mainly from neutrons of a few MeV, in the SiPM readout of both FPS and FPOST is monitored on a daily basis. This is particularly important for the high luminosities at $\sqrt{s} = 500$ GeV.

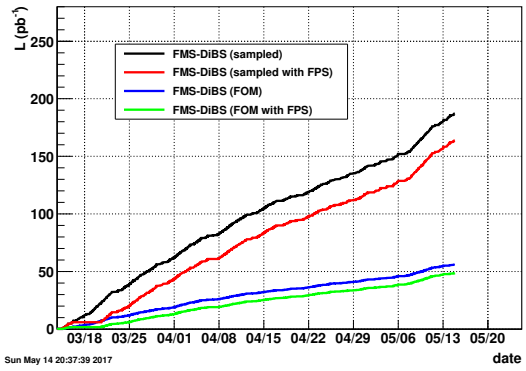

Figure 7: Sampled luminosity and figure of merit for the Drell-Yan trigger with FMS and FPS/FPOST. A new UV-LED system was installed and commissioned for Run 17 which eliminates subsequent adjustments of the PMT high voltages due to loss of light transparency of the lead glass towers.

The FMS has been outfitted with a new UV-LED system in order to be able to cure radiation damage throughout the running time. With this system in operation, the Pb glass towers do not suffer from deteriorating conditions of light transparency which in turn lead to shifting gains of the phototubes and subsequently required changes to the high voltages every few weeks. Triggering is based on particle p_T by summing over a few towers which reflect about the size of electromagnetic showers. The voltage settings for gain matching were fine tuned during the initial setup of p+p collisions. The full system of FMS in combination with FPS and FPOST and the triggering was commissioned by mid March. Figure 7 shows the recorded luminosity from the Drell-Yan trigger after folding in the preliminary efficiency of the pre- and postshower detectors. After careful balancing of the available bandwidth of the data acquisition system among all physics goals, the trigger is essentially sampling the full luminosity and we expect to be within 80% or more of the original goal by late May.

1.2 STAR Heavy-Ion Highlights

1.2.1 Open Heavy Flavor

Heavy (charm and bottom) quarks are primarily produced in initial hard scatterings in heavy-ion collisions. They are suggested as an excellent probe to study the properties of QGP. The Heavy Flavor Tracker (HFT), which was designed to improve the measurement precision of open heavy flavor production, recorded data in p+p, p/d+Au, and Au+Au collisions at $\sqrt{s_{NN}}$ = 200 GeV in Run 14-Run 16. Data analyses with the Run 14 Au+Au data and a part of the Run 16 Au+Au data have been performed to study heavy quark flow, hadronization, and energy loss in the medium. After fixing an offline software bug in the HFT-Pixel detector data decoder, the HFT matching efficiency has been greatly improved, leading to significantly better results in D^0 and D_s measurements, as well as the first measurement of Λ_c production in heavy-ion collisions. These results were reported at the QM2017 conference and are summarized below.

STAR has a paper [13] recently accepted for publication on Physics Review Letters on the elliptic flow coefficient (v_2) of D^0 mesons in Au+Au collisions at $\sqrt{s_{NN}}$ = 200 GeV, measured from about 900M minimum-bias (MB) events in Run 14. As can be seen in Fig. 8, the measured v_2 as a function of p_T in the 10-40% centrality bin shows a clear mass ordering for $p_T < 2$ GeV/c, and follows those of light mesons for $p_T > 2$ GeV/c. The measured v_2/n_q as a function of $(m_T - m_0)/n_q$ falls onto the same universal trend as the light hadrons, where n_q is the number of constituent quarks (NCQ) of the hadron, m_0 the rest mass and $m_T = \sqrt{p_T^2 + m_0^2}$. This suggests that charm quarks have gained flow through interactions with the QGP medium. The measured D^0 v_2 in the 0-80% centrality bin is compared with several model calculations. The v_2 predicted by the TAMU model with no charm quark diffusion is different from our data, while the same model with charm quark diffusion describes the data. A 3D viscous event-by-event hydrodynamic simulation with $\eta/s = 0.12$, using the AMPT initial condition and tuned to describe light hadron v_2, is consistent with our data for $p_T < 4$ GeV/c. This suggests that charm quarks may have achieved thermal equilibrium in these collisions. Several theoretical calculations with temperature-dependent, dimensionless charm quark spatial diffusion coefficients ($2\pi TD_s$) in the range of 2-12 can reproduce our D^0 v_2 result, while the values from lattice QCD calculations fall in the same range.

Quark coalescence has been proposed as a candidate to explain the above-mentioned NCQ scaling for elliptic flow, as well as the enhancement in the baryon-to-meson ratio for both light and strange flavor hadrons for $2 < p_T < 6$ GeV/c in heavy-ion collisions [14, 15]. It is very interesting to examine if coalescence plays a similar role in charm quark hadronzation. With the Run 14 data, STAR has obtained the first result on Λ_c baryon production and significantly improved the measurement of D_s meson production in Au+Au collisions, shown in Fig. 9. Both the Λ_c/D^0 and D_s/D^0 yield ratios are found to be significantly enhanced in Au+Au collisions with respect to those in p+p collisions predicted by PYTHIA. It is interesting to note that the Λ_c/D^0 ratio has a similar amplitude as the light/strange baryon-to-meson ratio measured by STAR, hinting for similar hadronization behavior for different flavor quarks at the measured kinematic range. A model calculation including coalescence hadronization and thermalized charm quarks [16] is consistent with the measured Λ_c/D^0 ratio. On the other hand, the TAMU model [17] underestimates the measured D_s/D^0 ratio, warranting new theoretical investigation.

An important signature of the QGP formation is the jet quenching, where energetic partons lose a significant amount of their energy in the medium. It is expected that such

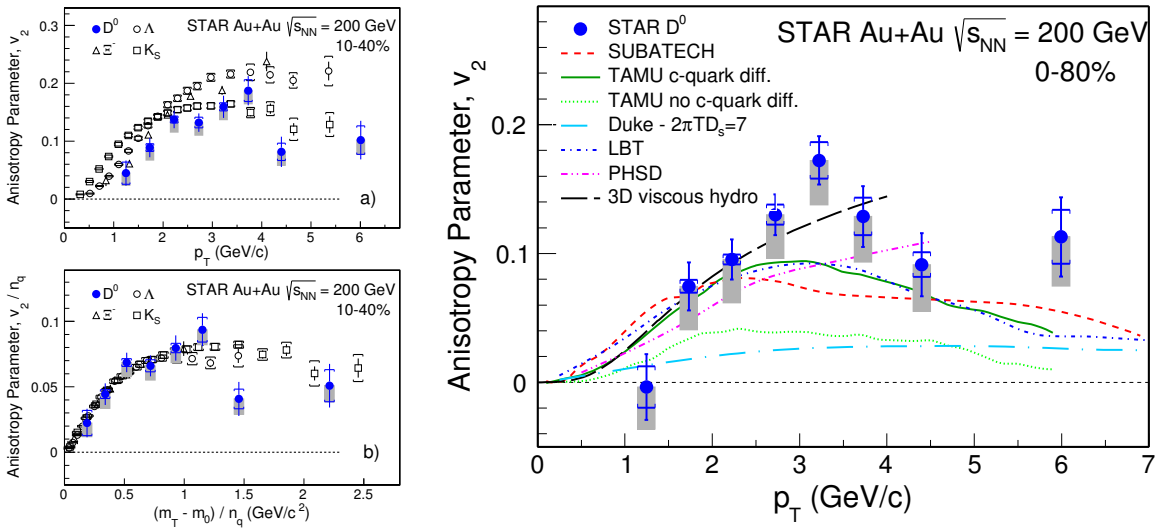

Figure 8: D^0 v_2 measurements in Au+Au collisions at $\sqrt{s_{NN}}$ = 200 GeV. left-top (left-bottom): D^0 v_2 (v_2/n_q) in 10-40% centrality interval. The vertical bars and brackets represent statistical and systematic uncertainties, and the grey bands represent the estimated non-flow contribution. Also shown are v_2 for K_s, Λ and Ξ. Right: D^0 v_2 as a function of p_T in 0-80% centrality interval. Model predictions are also shown in comparison.

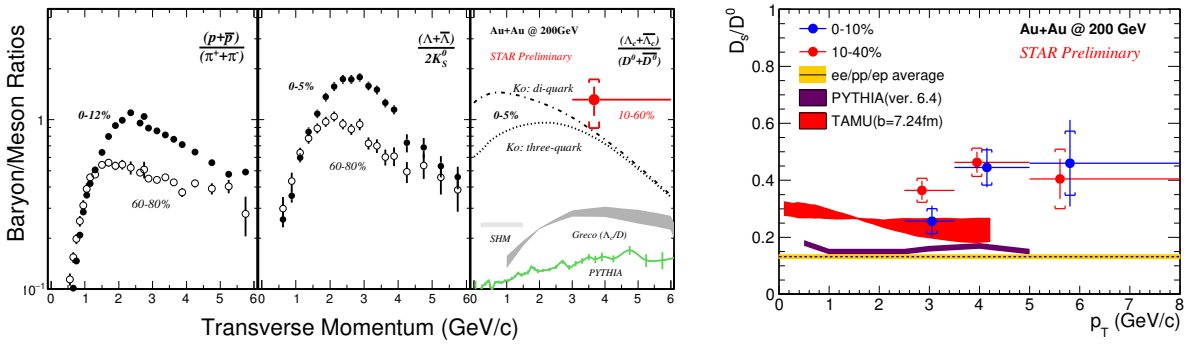

Figure 9: The Λ_c /D^0 (left) and D_s /D^0 (right) yield ratios as a function of p_T in Au+Au collisions at $\sqrt{s_{NN}}$ = 200 GeV. Model predictions are also shown in comparison.

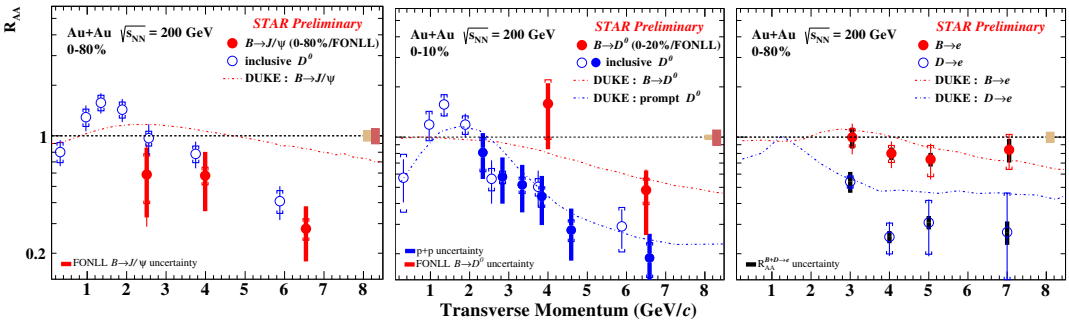

Figure 10: $R_{\rm AA}$ of non-prompt J/ψ (left), non-prompt D^0 (middle) and B-/D-decayed electrons (right) as a function of p_T in 0-80%, 0-10% and 0-80% Au+Au collisions at $\sqrt{s_{NN}}$ = 200 GeV, respectively. Error bars and brackets are statistical and systematic uncertainties, respectively. Shaded boxes at unity are the uncertainties from reference p+p measurements. Also shown are the $R_{\rm AA}$ for inclusive D^0 and the predictions from the DUKE model (dashed lines).

energy losses depend on the color charge and mass of the partons, i.e., $\Delta E_g > \Delta E_l > \Delta E_c > \Delta E_b$. Measurements of such flavor-dependent energy loss in the medium can help understand the energy loss mechanisms and ultimately properties of the QGP. STAR has measured open bottom and charm hadron production through multiple decay channels (Fig. 10). With the excellent track pointing resolution provided by the HFT, non-prompt J/ψ and non-prompt D^0 from open bottom hadron decays have been measured in Au+Au collisions at $\sqrt{s_{NN}} = 200$ GeV from Run 14+Run 16 and Run 14 data, respectively. They are found to be significantly suppressed at high p_T, suggesting sizable energy loss by bottom quarks in the QGP. Electrons from open bottom and charm hadron decays are also separately measured in Au+Au collisions and compared to those in p+p collisions. It has been found that the yield of bottom-decayed electrons are less suppressed than that of charm-decayed electrons in Au+Au collisions, consistent with the expected mass hierarchy of $\Delta E_c > \Delta E_b$.

Studies are underway with the Run 15 p+p and p+Au, and Run 16 Au+Au and d+Au data taken with the HFT. An issue in the HFT-Pixel detector firmware led to low matching efficiency in Run 15 data, and thus only hits from the HFT-IST and HFT-SSD detectors are included in track reconstruction for these data, which can significantly reduce the pile-up track contribution. The combined Run 15 p+p and p+Au data, and Run 16 d+Au data not affected by the firmware issue are expected to provide useful references for the open heavy flavor measurements in Au+Au collisions, for which improved results are expected from the full Run 14 and Run 16 Au+Au data.

1.2.2 Quarkonia

Quarkonium dissociation due to color-screening of the quark-antiquark potential in the deconfined medium was proposed as a direct signature of the QGP formation in heavy-ion collisions. Moreover, the dissociation of a quarkonium state depends on its binding energy and the temperature of the medium. Thus quarkonium suppression could be used to constrain the medium's temperature. However, other effects, such as regeneration from the coalescence of uncorrelated heavy quark pairs in the medium and Cold Nuclear Matter (CNM) effects, need to be understood in order to correctly interpret experimental results. The regeneration effect has been studied in a recent STAR Physics Letter B article on J/ψ production in Au+Au collisions at $\sqrt{s_{NN}} = 39$, 62.4 and 200 GeV from Run 10 and Run 11 data [18]. The left panel of Fig. 11 shows the results from STAR, NA50 and ALICE [18, 19, 20]. The dependence of J/ψ $R_{\rm AA}$ on $\sqrt{s_{NN}}$ can be described by theoretical calculations taking into account both the color-screening and regeneration effects [21]. New results on J/ψ production from Run 14 Au+Au, and Run 15 p+p and p+Au data in the di-muon channel (see below) were reported by STAR at the QM2017 conference, shedding light on color-screening, regeneration and CNM effects.

Compared to charmonia, bottomonia receive much less regeneration contributions due to the small bottom production cross section, and thus are suggested as a cleaner probe to study the QGP. The Muon Telescope Detector (MTD) has been fully installed in STAR since 2014, opening the door to study quarkonium production in the di-muon channel. Covering 45% in azimuth for $|y| < 0.5$, the MTD provides a better invariant mass resolution than the di-electron channel, which is crucial for separating different Υ states. The MTD recorded data of about 14 and 13 nb^{-1} in Au+Au collisions in Run 14 and Run 16, 122 pb^{-1} in p+p and 409 nb^{-1} in p+Au collisions in Run 15 at $\sqrt{s_{NN}} = 200$ GeV, respectively. New results on Υ production from Run 14 Au+Au data in the di-muon channel, and from Run 11 Au+Au, Run 15 p+p and p+Au data in the di-electron channel

were reported at the QM2017 conference and are summarized below.

With the MTD data in Run 14 and Run 15, STAR has measured the inclusive J/ψ production at mid-rapidity in Au+Au, p+p and p+Au collisions at $\sqrt{s_{NN}}$ = 200 GeV, respectively, shown in Figs. 11 and 12. It is found that the p_T-integrated $R_{\rm AA}$ decreases towards more central Au+Au collisions, while that in Pb+Pb collisions at $\sqrt{s_{NN}}$ = 2.76 TeV has a much weaker dependence on $N_{\rm part}$ and is significantly larger. This can be explained, similarly as the dependence of the J/ψ $R_{\rm AA}$ on $\sqrt{s_{NN}}$, by the larger regeneration contribution to low p_T J/ψ at the LHC than at RHIC. On the other hand, the $R_{\rm AA}$ for p_T > 5 GeV/c in Au+Au collisions at $\sqrt{s_{NN}}$ = 200 GeV is larger than that for p_T > 6.5 GeV/c in Pb+Pb collisions at $\sqrt{s_{NN}}$ = 2.76 TeV. This can be explained by the stronger color-screening effect at the LHC with higher temperature. Theoretical models [21, 22, 23, 24] including both the color-screening and regeneration effects can qualitatively describe the RHIC and LHC data. The production cross section as a function of p_T in p+p collisions in the di-muon channel from Run 15 data is consistent with that in the di-electron channel from Run 12 data, and can be described by the CGC+NRQCD calculation [25] at low p_T and NLO NRQCD calculation [26] at high p_T for prompt J/ψ production, but not by the improved CEM calculation [27] including only direct J/ψ production. The $R_{\rm pA}$ is found to be less than unity at low p_T, and consistent with unity at high p_T. This result favors the model calculation including an additional co-mover absorption effect [28] over those including the nuclear PDF effect only [29].

A significant excess of J/ψ yield at very low p_T (< 0.3 GeV/c) at forward-rapidity has been observed in peripheral hadronic Pb+Pb collisions at $\sqrt{s_{NN}}$ = 2.76 TeV [30], which cannot be explained by the hadronic J/ψ production modified by the cold or hot medium effects. STAR has observed a similar excess at mid-rapidity in peripheral hadronic Au+Au collisions at $\sqrt{s_{NN}}$ = 200 GeV and U+U collisions at $\sqrt{s_{NN}}$ = 193 GeV from Run 10 and Run 12 data. The excess shows no significant centrality dependence over the 30-80% centrality range, which is beyond the expectation from hadronic production, and is consistent with coherent photon-nucleus interactions. Shown in the right panel of Fig. 12 is the J/ψ yield as a function of $t = p_T^2$ in 40-80% Au+Au collisions. The structure of the distribution is very similar to that observed in ultra-peripheral collisions where the impact parameter of the collision is larger than the diameter of Au nuclei. An exponential fit has been applied to the distribution for $0.002 < t < 0.015$ GeV^2/c^2, and the extracted slope parameter is 196 ± 31 GeV^{-2}/c^{-2}, which is consistent with that of a Au nucleus (199 GeV^{-2}/c^{-2}).

Υ production has been measured in the di-electron channel in p+p and p+Au collisions at $\sqrt{s_{NN}}$ = 200 GeV via the Run 15 data, corresponding to integrated luminosities of about 100 pb^{-1} and 300 nb^{-1}, respectively (Fig. 13 left panel). The production cross section as a function of rapidity in p+p collisions have been measured with a factor of two smaller uncertainty than the previously published STAR results [31], providing a greatly improved p+p reference for studying the CNM and hot nuclear matter effects. The $R_{\rm pA}$ is measured with a factor of two smaller relative uncertainty than the previously published $R_{\rm dA}$ result by STAR [31]. The result indicates the presence of CNM effects for Υ production at RHIC. The $R_{\rm AA}$ has been measured in Au+Au collisions at $\sqrt{s_{NN}}$ = 200 GeV in the di-electron channel with Run 11 data and in the di-muon channel with Run 14 data (Fig. 13 middle and right panels). The combined $R_{\rm AA}$ result for Υ(1S) is found to be similar to that in Pb+Pb collisions at $\sqrt{s_{NN}}$ = 2.76 TeV, having no strong p_T dependence, and decreasing towards more central collisions. The Υ(2S+3S) $R_{\rm AA}$ is reported for the first time, which is significantly more suppressed than that of Υ (1S) in the most central Au+Au collisions, consistent with the expected sequential melting

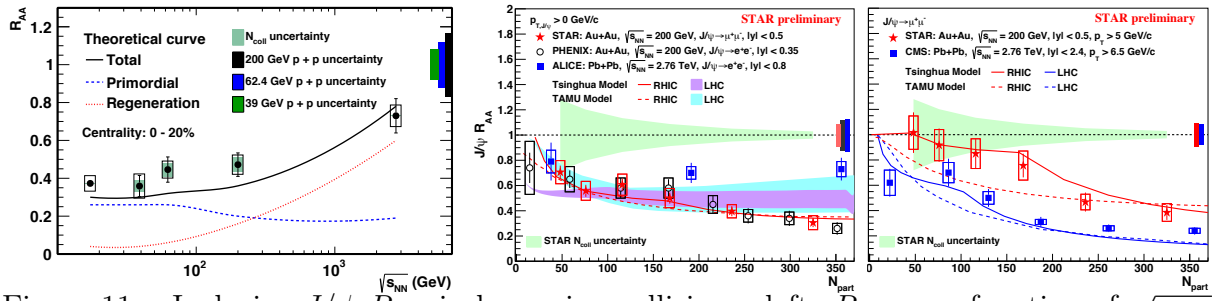

Figure 11: Inclusive J/ψ $R_{\rm AA}$ in heavy-ion collisions. left: $R_{\rm AA}$ as a function of $\sqrt{s_{NN}}$ in 0-20% centrality interval at SPS-RHIC-LHC energies. middle (right): $R_{\rm AA}$ for $p_T > 0$ (5 or 6.5) GeV/c as a function of $N_{\rm part}$ in Au+Au collisions at $\sqrt{s_{NN}}$ = 200 GeV and Pb+Pb collisions at $\sqrt{s_{NN}}$ = 2.76 TeV.

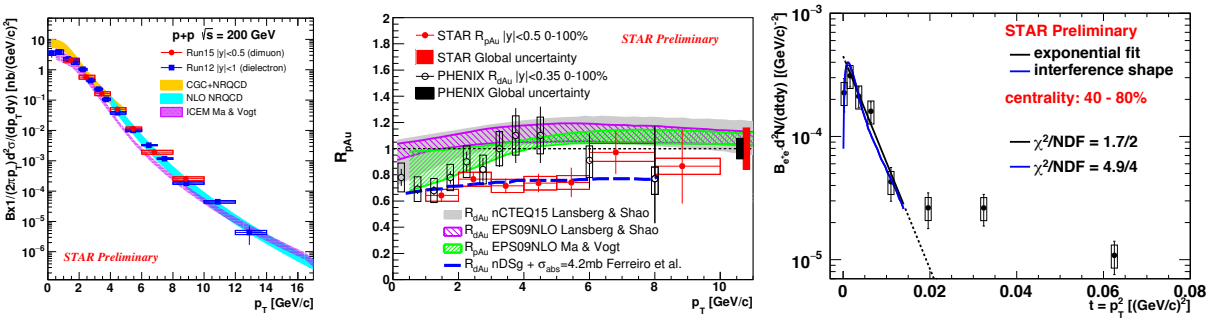

Figure 12: Inclusive J/ψ measurements in p+p, p+Au and Au+Au collisions at $\sqrt{s_{NN}}$ = 200 GeV. left: production cross section scaled by the branching ratio as a function of p_T in the di-muon (red circles) and di-electron decay channels (blue squares) in p+p collisions. middle: Nuclear modification factor $R_{\rm pA}$ (solid circles) as a function of p_T in the di-muon decay channel in p+Au collisions. Also shown are the $R_{\rm dA}$ from PHENIX (open circles) and theoretical model calculations. right: Low-p_T J/ψ yield as a function of $t = p_T^2$ in the di-electron decay channel in 40-80% Au+Au collisions.

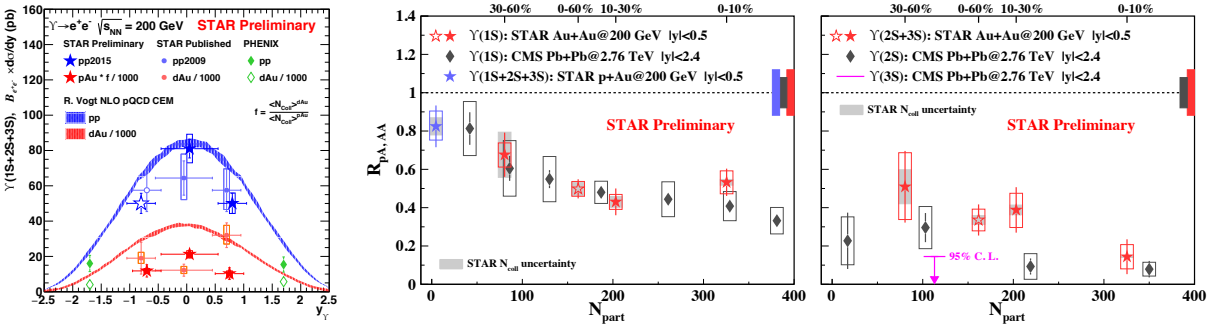

Figure 13: Upsilon measurements in p+p, p+Au and Au+Au collisions at $\sqrt{s_{NN}}$ = 200 GeV. left: Υ (1S+2S+3S) production cross section as a function of rapidity in the di-electron decay channel in p+p (blue stars) and p+Au (red stars) collisions. Also shown are the previously published p+p and d+Au results by STAR and PHENIX, and NLO CEM calculations (shaded bands). middle (right): Υ (1S) (Υ (2S+3S)) $R_{\rm AA}$ from the di-electron and di-muon channels as a function of $N_{\rm part}$ for $|y| < 0.5$. Also shown are the $R_{\rm pA}$ of Υ (1S+2S+3S) for $|y| < 0.5$ in the di-electron channel, and the latest CMS result for $|y| < 2.4$ in Pb+Pb collisions at $\sqrt{s_{NN}}$ = 2.76 TeV (black rhombus).

phenomenon. Analyses are underway with the combined Run 10 and Run 11 data in the di-electron channel as well as Run 14 and Run 16 data in the di-muon channel, which are expected to improve the Υ $R_{\rm AA}$ measurement precision in Au+Au collisions at $\sqrt{s_{NN}}$ = 200 GeV.

1.2.3 Jets

Jets are an important probe to study properties of the QGP. Measurement of di-jet imbalance [32] and semi-inclusive hadron+jets [33] were submitted for publication by STAR. With respect to those in p+p collisions, di-jet pairs reconstructed from constituents with $p_T > 2$ GeV/c are found to be significantly imbalanced in Au+Au collisions, while the lost energy can be recovered in soft constituents ($p_T > 0.2$ GeV/c) with signs of broadening of the jet structure within a jet radius of $R = 0.4$ [32]. This is consistent with the measurement of semi-inclusive hadron+jets, where the yield of jets recoiling from a high-p_T trigger hadron is suppressed in central Au+Au collisions, corresponding to medium-induced energy transport to large angles relative to the jet axis of $\sim 3-5$ GeV/c [33]. Recently, new measurements have been performed on the Jet Splitting Function $z_g = \frac{min(p_{T,1},p_{T,2})}{p_{T,1}+p_{T,2}}$ through the SoftDrop grooming process in p+p and Au+Au collisions at $\sqrt{s_{NN}}$ = 200 GeV from 2006 and 2007 data (Fig. 14). Modification of the z_g function is predicted in some energy loss models, and thus the measurement of z_g gives qualitative constraints for theoretical treatment. As can be seen in Fig. 14, the measured z_g for $10 < p_T^{part} < 30$ GeV/c in p+p collisions at 200 GeV are in good agreement with PYTHIA simulations. Here p_T^{part} is the jet p_T corrected to particle level. In Au+Au collisions, di-jet pairs used in the previous momentum imbalance measurement [32] are used in the z_g measurement. It is found that within uncertainties there are no signs of a modified Jet Splitting Function on trigger or recoil side of this di-jet selection. In a similar study, the CMS collaboration first reported significant modifications of the Jet Splitting Function in central Pb+Pb collisions at 5 TeV. Close collaboration with the theory community will be needed to interpret these findings. Also shown for the first time at QM2017 were first studies of semi-inclusive recoil jets coincident to a high p_T π^0 and hadron correlations with respect to reconstructed di-jets. The π^0-jet distributions show agreement, within uncertainties, with the submitted $h^{\pm}$+jet distributions. The larger statistics from Runs 14 and 16 should allow precise comparisons of direct photon-jet and π^0-jet recoil spectra potentially revealing further details of partonic interactions with the medium. The di-jet+hadron correlations study supports the picture that this selected "hard core" di-jet sample is mostly tangential to the fireball, and that the modification seen primarily affects the recoil jet.

1.2.4 Exploration of the Phase Diagram in BES-I

An important goal of high-energy heavy-ion collision experiments is to explore the Quantum Chromodynamics (QCD) phase diagram, usually spanned by temperature (T) versus baryon chemical potential (μ_B). If a thermalized system is created in heavy-ion collisions, both T and μ_B can be varied by changing the collision energy [34, 35, 36, 37], as at RHIC for the Beam Energy Scan phase I (BES-I) program. In order to estimate the T and μ_B regions of the phase diagram for a given collision energy, one can study the hadron spectra. These spectra reflect the properties of the bulk matter at the kinetic freeze-out that takes place after all the elastic scatterings have ceased. Information on the earlier stages can be deduced from the integrated yields of different hadron species, which change

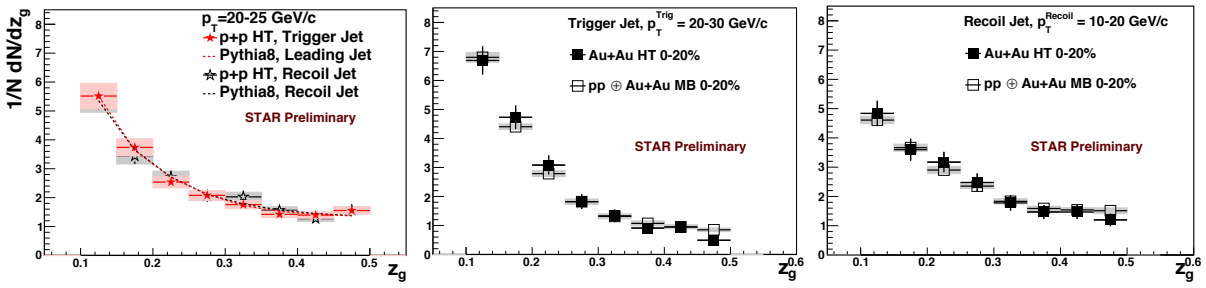

Figure 14: Left: z_g distributions for trigger (filled symbols) and recoil (open symbols) jets independently binned in p_T^{part} in p+p HT compared to PYTHIA8 (dashed lines). Middle (Right): z_g in Au+Au HT (filled symbols) data and p+p HT plus Au+Au MB (open symbols) for trigger (recoil) jets. Shaded bands indicate systematic uncertainty estimate due to the jet energy scale.

only via inelastic scatterings. The point when the inelastic scatterings cease is called the chemical freeze-out.

Recently STAR has submitted a paper [38] on the measurement of bulk properties of the medium produced in relativistic Au+Au collisions from BES-I. This paper presents thermal fits to the data for collision energies from $\sqrt{s_{NN}}$= 200 to 7.7 GeV and shows that the μ_B extracted range from $\sim$ 20 to $\sim$ 400 MeV as expected.

In addition, a Blast-Wave model fit to pion, kaon, proton, and antiproton p_T spectra allowed the extraction of the common temperature, T_{kin}, and average transverse radial flow velocity, β, at kinetic freeze-out.

Figure 15 (left plot) shows the energy dependence of the kinetic and chemical freeze-out temperatures for central heavy-ion collisions. The values of the kinetic and chemical freeze-out temperatures are similar around $\sqrt{s_{NN}}$ = 4–5 GeV. Above $\sqrt{s_{NN}}$ = 11.5 GeV, the chemical freeze-out temperature increases with increasing the collision energy, whereas the kinetic freeze-out temperature becomes constant. Figure 15 (right plot) shows the average transverse radial flow velocity plotted as a function of $\sqrt{s_{NN}}$. The $\langle\beta\rangle$ shows a rapid increase at very low energies, and then a steady increase up to LHC energies.

T_{kin} increases from central to peripheral collisions suggesting a longer lived fireball in central collisions, while $\langle\beta\rangle$ decreases from central to peripheral collisions suggesting stronger expansion in central collisions. The separation between T_{ch} and T_{kin} increases with increasing energy. This suggests the effect of increasing hadronic interactions between chemical and kinetic freeze-out at higher energies.

1.2.5 Search for the First-Order Phase Transition

A first-order phase transition is characterized by a discontinuity in one of the equation-of-state (EOS) variables. Lattice QCD predicts that there should be a discontinuity in the density below T_C [39]. A first-order phase transition is also characterized by an unstable coexistence region. This region will exhibit a change in compressibility, i.e. a softening of the EOS. In the scenario of nuclear collisions at the optimum beam energy for a first-order phase transition, various models have predicted characteristic azimuthal anisotropy signals [40, 41]. These patterns can be studied via measurement of the Fourier expansion of the final-state momentum-space azimuthal distribution relative to the reaction plane [42]. For example, the directed and elliptic flow can be quantified by the first (v_1) and second (v_2) Fourier coefficients of the expansion.

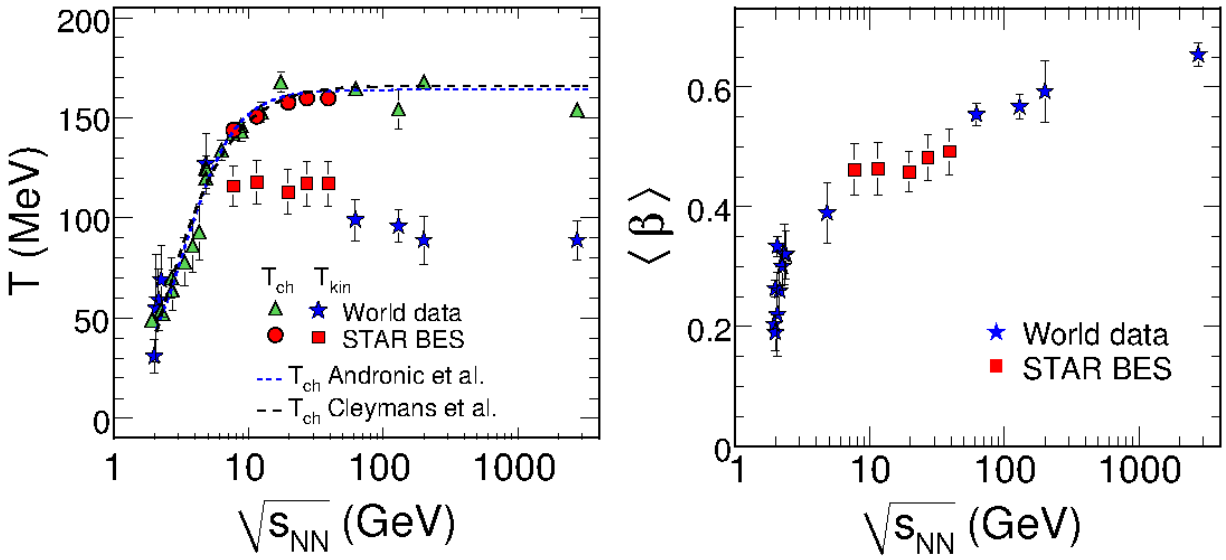

Figure 15: (left plot) Energy dependence of the kinetic and chemical freeze-out temperatures for central heavy-ion collisions. The curves represent various theoretical predictions. (right plot) Energy dependence of average transverse radial flow velocity for central heavy-ion collisions. Uncertainties represent systematic uncertainties.

Directed flow in BES-I: Recently, STAR published the beam energy dependence of the slope of directed flow (dv_1/dy) for protons and net protons near mid-rapidity [43]. The observation of a minimum in the slope of directed flow for protons and net-protons around $\sqrt{s_{NN}}$ = 10–20 GeV, and a double sign change in this observable for net-protons, suggest a possible softening of the QCD equation of state [44]. Recent model calculations, with and without crossover and first-order phase transitions, show large discrepancies with the STAR measurements [45, 46, 47].

The left plot of Figure 16 shows the dv_1/dy for all the measured strange hadrons, protons and antiprotons. The dv_1/dy slope of Λ is consistent with that of protons at all beam energies, while the $\bar{\Lambda}$ follows the trend of antiprotons. The dv_1/dy for K^+ is closer to zero than that for K^- for $\sqrt{s_{NN}}$ >14.5 GeV. The neutral kaon dv_1/dy follows charged kaon trend and lays between positive and negative kaons. The dv_1/dy for ϕ meson shows similar trends as $\bar{\Lambda}$ and $\bar{p}$ for $\sqrt{s_{NN}}$ >14.5 GeV, while at 11.5 GeV it is consistent with zero within large uncertainty.

This new set of measurements with different hadron species (Λ, $\bar{\Lambda}$, $K^{\pm}$, K^0_s and ϕ) [48, 49], and hence different constituent quarks, will not only help to understand the QCD phase transition, but in addition will allow to disentangle the role of produced and transported quarks in heavy-ion collisions. The ϕ meson offers a unique advantage because its mass is similar to the proton mass, yet it is a vector meson. Moreover, ϕ meson is minimally affected by late-stage hadronic interactions.

The right plot of Figure 16 shows a comparison between the measurements and UrQMD [50] for ϕ, Λ and p. UrQMD seems to follow the trend of the data for higher beam energies, but deviates at lower energies.

Directed flow in asymmetric systems: Recent theoretical studies suggest that an asymmetric colliding system can provide new insights regarding the properties of a QGP, such as the electric conductivity [51] and the time evolution of the quark densities [52]. Due to the difference in the number of protons in the two nuclei, a strong electric field is created at the initial stage. The electric charges from quarks and antiquarks that are present

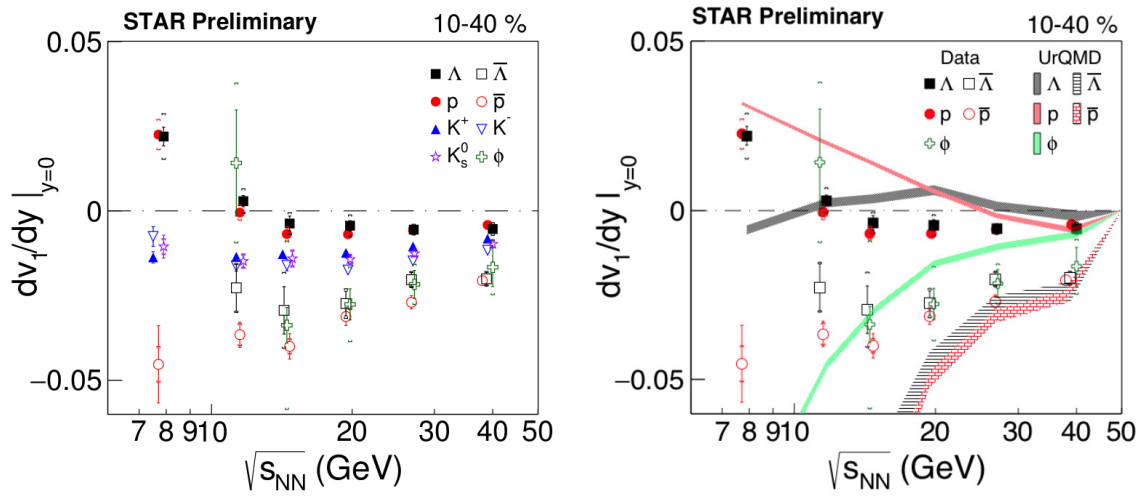

Figure 16: (left plot) Beam energy dependence of dv_1/dy for p, $\bar{p}$, $K^{\pm}$, K^0_s, ϕ, Λ and $\bar{\Lambda}$ in 10–40% Au+Au collisions. (right plot) Beam energy dependence of dv_1/dy for p, $\bar{p}$, ϕ, Λ and $\bar{\Lambda}$ in 10–40% Au+Au collisions. STAR data are compared with UrQMD model [50].

in the early stage of the collision would experience the Coulomb force and so would be pushed along or opposite to the field direction depending on the particle charge.

STAR recently published in PRL measurements of positive and negative particle v_1 as a function of p_T in Cu+Au and Au+Au collisions at top RHIC energy [53]. Figure 17 shows the dependencies of v_1 and Δv_1 on p_T. A finite difference in v_1 between positive and negative charged particles was observed in the transverse momentum range of $0.15 < p_T < 2$ GeV/c for Cu+Au collisions, meanwhile, the same difference is absent for Au+Au collisions (within uncertainties).

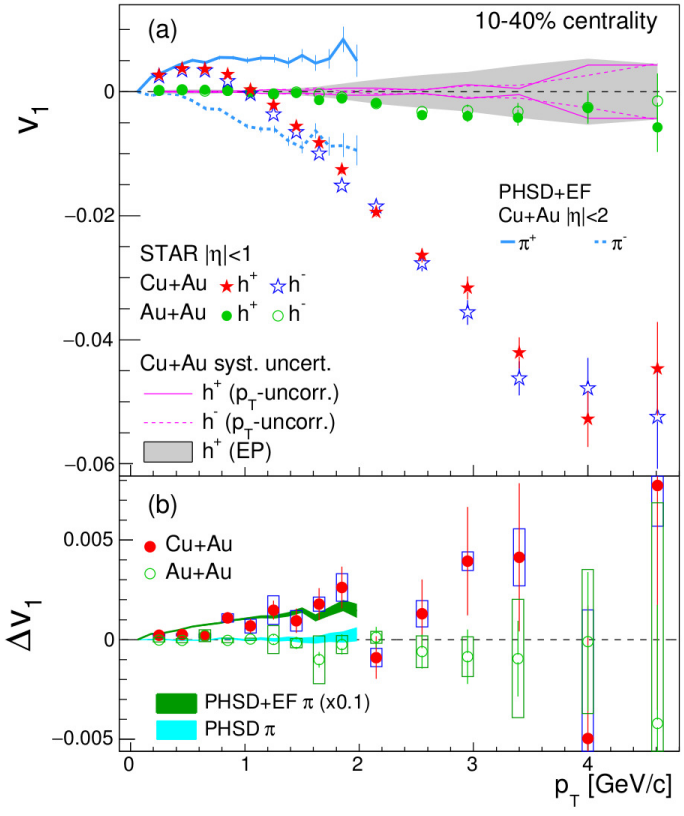

Figure 17: Directed flow of positive and negative particles and the difference between the two spectra as a function of p_T in 10%–40% centrality in Cu+Au and Au+Au collisions. The PHSD model calculations [52] for charged pions with and without the initial electric field (EF) in the same centrality region are presented for comparison. Note that the charge difference of v_1 with the EF-on is scaled by 0.1.

These results are consistent with the presumption of a strong, initial, electric field in asymmetric collisions. The observed Δv_1 was compared to the PHSD model calculations that includes the effect of an electric field. The p_T dependence of Δv_1 is qualitatively described by the model in the region less than 2 GeV/c, but the magnitude of Δv_1 is smaller by a factor of 10 than the model predictions, assuming that all quarks are created at the initial time. This may indicate that most of quarks and antiquarks have not yet been created within the lifetime of the electric field ($t \leq 0.25$ fm/c).

1.2.6 Elliptic Flow of the QCD Medium

The study of collective flow in relativistic nuclear collisions could provide insights into the EOS of the matter created during heavy-ion collisions. The v_2 coefficient has proven to be one of the most discussed probes of the dynamics in nuclear collisions.

Multistrange particle v_2: As recently reported in PRL, STAR measured the centrality and transverse momentum dependence of elliptic flow of multistrange hadrons and ϕ meson in Au+Au collisions at top RHIC energy [54]. It was found that unlike π and p, the ϕ and Ω do not participate strongly in the hadronic interactions, which suggests that the major part of collectivity is developed during the partonic phase in Au+Au collisions at $\sqrt{s_{NN}} = 200$ GeV.

Figure 18 shows the ratios of ϕ meson v_2 to proton v_2. The ratios are larger than unity at p_T ~0.5 GeV/c for 0%–30% centrality showing an indication of the breakdown of the expected mass ordering in that momentum range. This could be due to a large effect of hadronic rescattering on the proton v_2, indicated by the shaded red band in Figure 18(a).

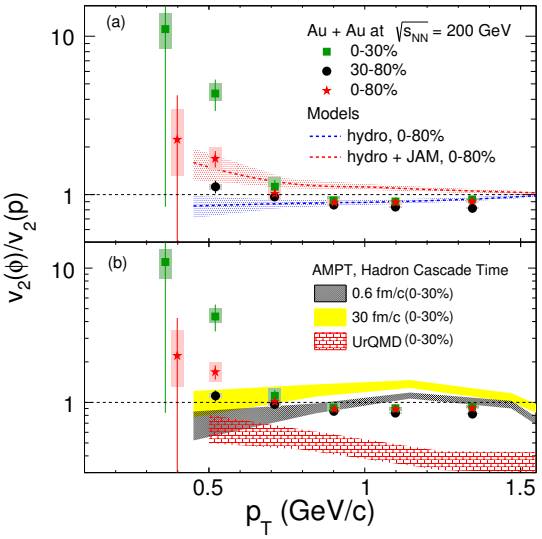

Figure 18: $v_2(\phi)/v_2(p)$ ratio as a function of p_T for 0%–30%, 30%–80%, and 0%–80% centrality in Au+Au collisions at $\sqrt{s_{NN}} =$ 200 GeV. Shaded boxes are the systematic uncertainties and vertical lines are the statistical uncertainties. The first data point of 0%–80% centrality is shifted to the right by 400 MeV/c. The bands in (a) and (b) represent the Hydrodynamics model [55] and transport model calculations, respectively, for $v_2(\phi)/v_2(p)$.

The effect is more pronounced in the 0%–30% than in 30%–80% centrality. In the central events, both hadronic and partonic interactions are larger than in peripheral events. Therefore, the combined effects of large partonic collectivity on the ϕ meson v_2 and significant late-stage hadronic interactions on the proton v_2 produce a greater breakdown of the mass ordering in the 0%–30% centrality data than in the 30%–80%. This observation indirectly supports the idea of a small hadronic interaction cross section for the ϕ meson. The ratio of ϕ v_2 to proton v_2 has been also studied using transport models AMPT [56] and UrQMD [50]. Figure 18(b) shows ratios for 0%–30% centrality from the AMPT and UrQMD models. The black shaded band is from AMPT with a hadronic cascade time of 0.6 fm/c, while the yellow band is for a hadronic cascade time of 30 fm/c. It becomes clear

that with increasing hadronic cascade time (and therefore more hadronic rescattering), the $v_2(\phi)/v_2(p)$ ratio increases. This is attributed to a decrease in the proton v_2 due to an increase in hadronic rescattering, while the ϕ v_2 remains unaffected.

Elliptic flow of light nuclei: STAR has measured the centrality dependence of the relative difference of baryon and antibaryon elliptic flow [57, 58]. It was found that the difference becomes larger with decreasing collision energy.

In a relativistic heavy-ion collision, light (anti-)nuclei can be formed by coalescence of produced (anti-)nucleons or from transported nucleons. The binding energies of light nuclei are very small (∼few MeV), making it likely that surviving light nuclei are formed at a later stage of the evolution. This phenomenon is called final-state coalescence.

STAR studied the p_T dependence of v_2 of p, $\bar{p}$, d, $\bar{d}$, t, ^3He and $^3\bar{H}e$ from Au+Au collisions in BES-I [59]. Figure 19 shows the light-nuclei v_2/A as a function of p_T/A where A is the atomic mass number of the corresponding light nuclei. It is observed that the (anti)nuclei v_2/A closely follows v_2/A of p ($\bar{p}$) for p_T/A up to 1.5 GeV/c within 5%–20% or all beam energy range presented. The scaling behavior of these nuclei suggest that d ($\bar{d}$) within $p_T < 3.0$ GeV/c and t, ^3He ($^3\bar{H}e$) within $p_T < 4.5$ GeV/c might have formed via the coalescence of nucleons (antinucleons).

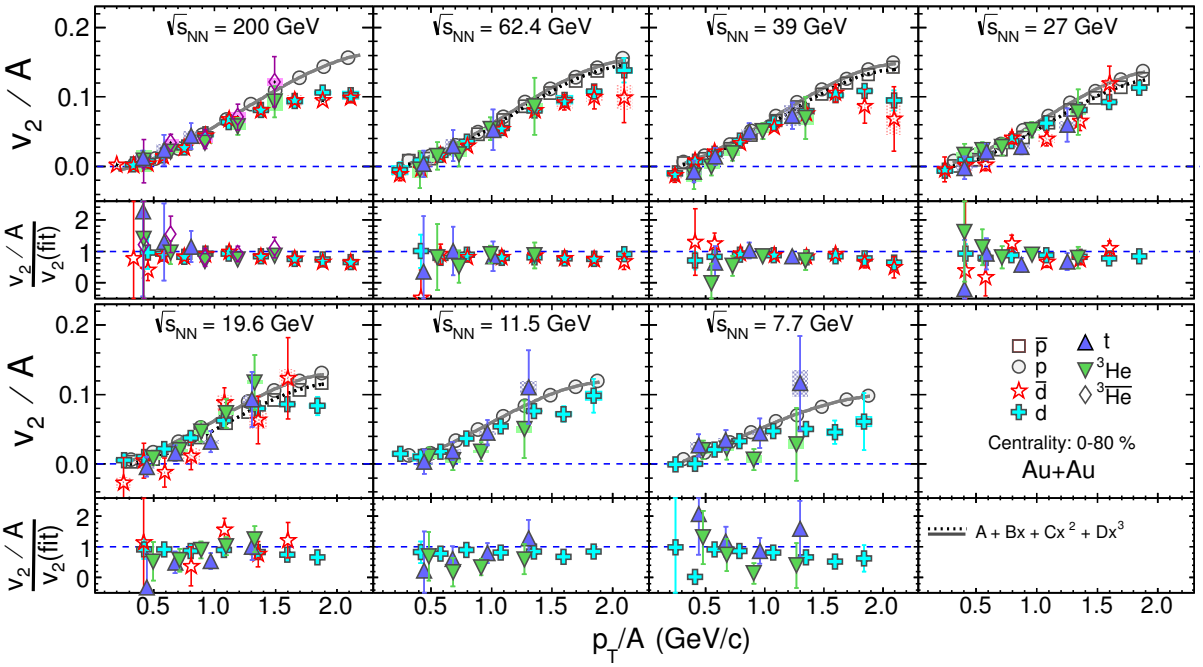

Figure 19: Atomic mass number (A) scaling of the midrapidity v_2 of p, $\bar{p}$, d, $\bar{d}$, t, ^3He and $^3\bar{H}e$ from minimum-bias Au+Au collisions at $\sqrt{s_{NN}}$ = 200, 62.4, 39, 27, 19.6, 11.5, and 7.7 GeV. Gray solid (black dotted) lines correspond to third order polynomial fits to the p ($\bar{p}$) v_2 data. The ratios of (v_2/A/fit) for d, $\bar{d}$, t and ^3He are shown in the lower panels at each corresponding collision energy.

The low relative production of light nuclei and the scaling behavior of their elliptic flow seems to be favored by the coalescence formalism over the other methods, such as thermal production which can reproduce the measured particle ratios in data [60]. Although simple A scaling seems to hold for the collision energies presented, the actual mechanism might be a more dynamic process including production and coalescence of nucleons in the local rest frame of the fluid cell.

In addition, STAR presented at QM2017 the dependence of the coalescence factor of

deuterons and antideuterons, B_2, as a function of m_T and collision energy. It was found that B_2 decreases with increasing m_T . The B_2 decreases with decreasing energy showing the minimum at around $\sqrt{s_{NN}}$ =20 GeV. The $B_2(\bar{d})$ is systematically lower that those of $B_2(d)$. This suggests that the emitting source of antibaryons is larger that for baryons.

1.2.7 Rapidity Correlations

Initial state density fluctuations and the pressure gradient of the strongly interacting medium in the transverse plane result in azimuthal anisotropies of the emitted particles in the final state. The density fluctuations can be studied in terms of correlations of particles in the longitudinal direction, i.e. in (pseudo)rapidity [61]. Long-range rapidity correlations, and other "short range" mechanisms such as resonance decays, jet fragmentation, and quantum statistical effects, appear in specific ways in the correlation function [62]. The shape of the longitudinal correlations can be characterized by Legendre polynomials with magnitudes given by prefactors a_{nm}.

Rapidity correlations were studied and reported for the first time at QM2017 in Au+Au collisions at eight different beam energies from 7.7 to 200 GeV (0%–5% centrality) as measured by STAR for the BES-I program [63]. It was observed that the magnitude of the coefficients decreases with increasing beam energy, indicating decreased two-particle correlations per pair as $\sqrt{s_{NN}}$ increases. A significant increase in the magnitude of the $\langle a_{nm} \rangle$ coefficients for pions at 19.6 and 27.0 GeV was observed. In order to understand the observed structure, the averaged correlation functions for pions versus Δy were calculated in three different ranges of the azimuthal angle $\Delta\phi$: near-side (-30° < $\Delta\phi$ < 30°), far-side (150° < $\Delta\phi$ < 210°) and transverse (30° < $\Delta\phi$ < 150° and 210° < $\Delta\phi$ < 330°) for 19.6 and 27 GeV and their neighboring energies (14.5 and 39 GeV) as shown in Figure 20.

In the near-side projection there is a peak around $\Delta y \sim 0$ which is stronger in unlike-sign pions than like-sign pions. This is an expected feature of the short-range correlation mechanisms that are dominant in this $\Delta\phi$ range. There is no significant structure in the far-side projection of both like-sign and unlike-sign pions at these energies. However, the transverse projection shows a significant and unexpected peak around $\Delta y \sim 0$ at 19.6 and 27 GeV. This structure has the same magnitude for both like-sign and unlike-sign pions.

1.2.8 Global Hyperon Polarization

Non-central collisions have angular momentum on the order of $1000\hbar$, and shear forces generated by the interpenetrating nuclei may generate a clear vortical structure [64, 65, 66]. A slight sideward deflection of the forward- and backward-traveling fragments from a given collision allows experimental determination of the direction of the overall angular momentum, $\hat{J}_{sys}$. Spin-orbit coupling can generate a spin alignment, or polarization, along the direction of the vorticity which is on average parallel to $\hat{J}_{sys}$. Hence, polarization measurements of hadrons emitted from the fluid can be used to determine the vorticity.

STAR used Λ and $\bar{\Lambda}$ to measure the global hyperon polarization in non-central Au+Au collisions [67]. The advantage of using Λ-hyperons is that due to the weak decay into p and π^-, the proton tends to be emitted along the spin direction of the parent Λ. The polarization ($\vec{P}_H$) may depend on the momentum of the emitted hyperons. However, when averaged over all phase space, symmetry demands that $\vec{P}_H$ is parallel to $\hat{J}_{sys}$. Due to the limited statistics, only the average projection ($\bar{P}_H$) of $\vec{P}_H$ on $\hat{J}_{sys}$ was extracted.

Figure 21 shows the measurements of the global polarization as a function of collision energy. At each energy, a positive polarization at the level of 1.1–3.6 times statistical

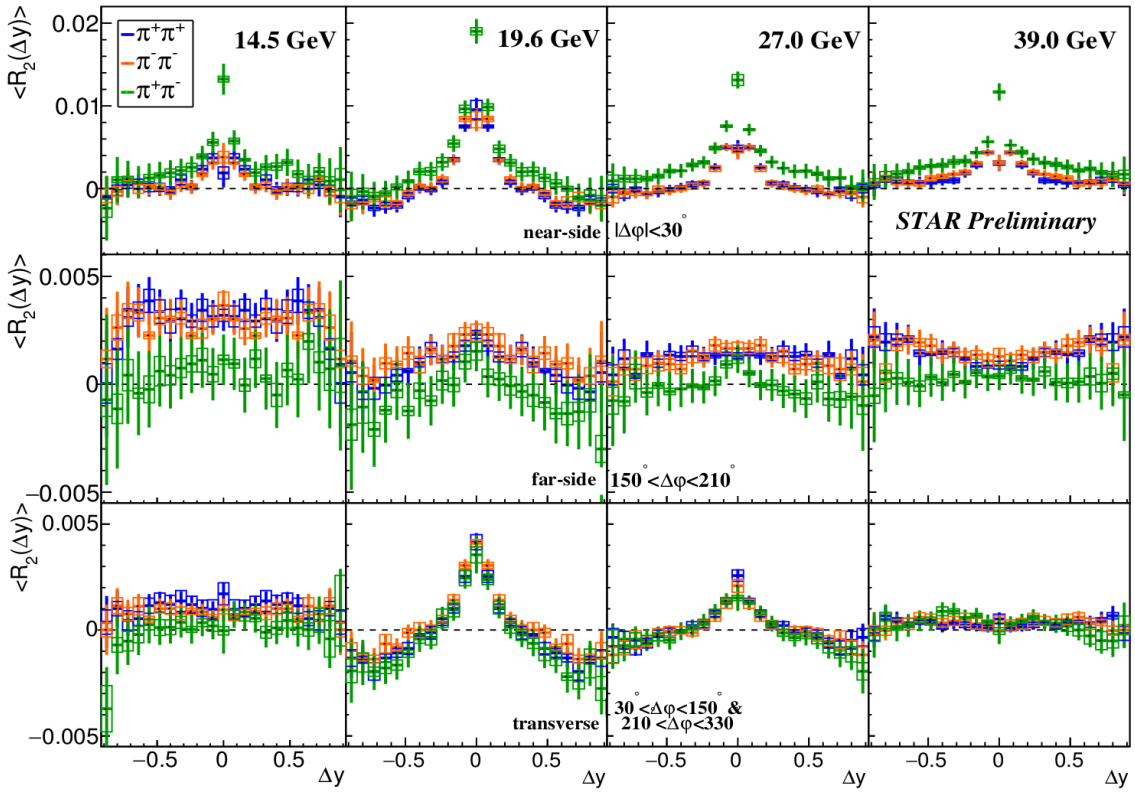

Figure 20: The averaged correlation function for pions as a function of Δy for 14.5, 19.6, 27, and 39 GeV (from left to right respectively) beam energies in 0%–5%

uncertainty is observed for both Λ and $\bar{\Lambda}$. The data are statistically consistent with the hypothesis of energy-independent polarizations of 1.08 ± 0.15 and 1.38 ± 0.30 percent for Λ and $\bar{\Lambda}$, respectively.

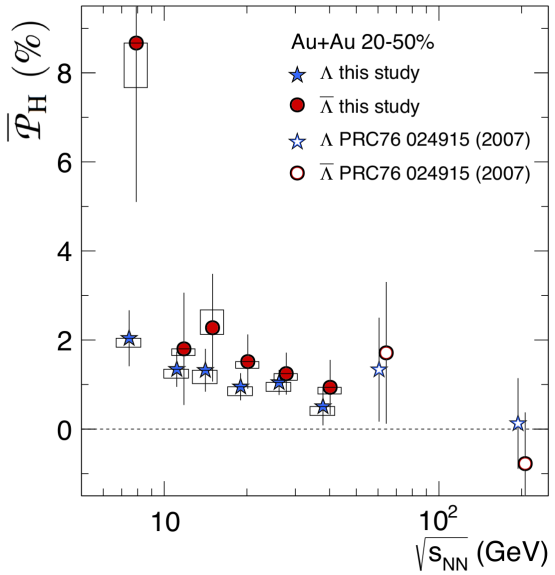

Figure 21: The average polarization $\bar{P}_H$ (where H = Λ or $\bar{\Lambda}$) from 20%–50% central Au+Au collisions as a function of collision energy. The results of the present study ($\sqrt{s_{NN}}$ <40 GeV) are shown together with those reported earlier [68] for 62.4 and 200 GeV collisions, for which only statistical errors are plotted. Boxes indicate systematic uncertainties.

Previously published measurements at $\sqrt{s_{NN}}$ = 62.4 GeV and 200 GeV are shown by open symbols [68]. The null result reported in that paper may be considered to be consistent with the trend of our measurements, within reported statistical uncertainty.

The $\sqrt{s_{NN}}$-averaged polarizations indicate a vorticity of $\omega \approx (9 \pm 1) \times 10^{21}$ s^{-1}, which is estimated using the hydrodynamic relations and takes into account the "feed-down" contributions [69]. The discovery of the global Λ polarization in non-central heavy-ion collisions opens new directions in the study of the hottest, least viscous – and now, most vortical – fluid ever produced in the laboratory. These results have been accepted for publication in Nature.

1.2.9 First Fixed Target Results

The test run for the fixed target (FXT) program performed in Run 15 while primarily a technical test also resulted in 1.3 millions Au+Au events being acquired at $\sqrt{s_{NN}} = 4.5$ GeV. Analysis of these events has been completed and were reported at the QM2017 meeting. The new results were compared to previously published data from the AGS program to demonstrate consistency. Results were presented for spectra of π, K^0_S, and Λ, directed flow of π, K^0_S, p, and Λ, elliptic flow of π and p, HBT, and particle ratio fluctuations. Some results of this test run are shown in Fig. 22. Further details of the proposed fixed target program and its science case are given in Section 3.4.

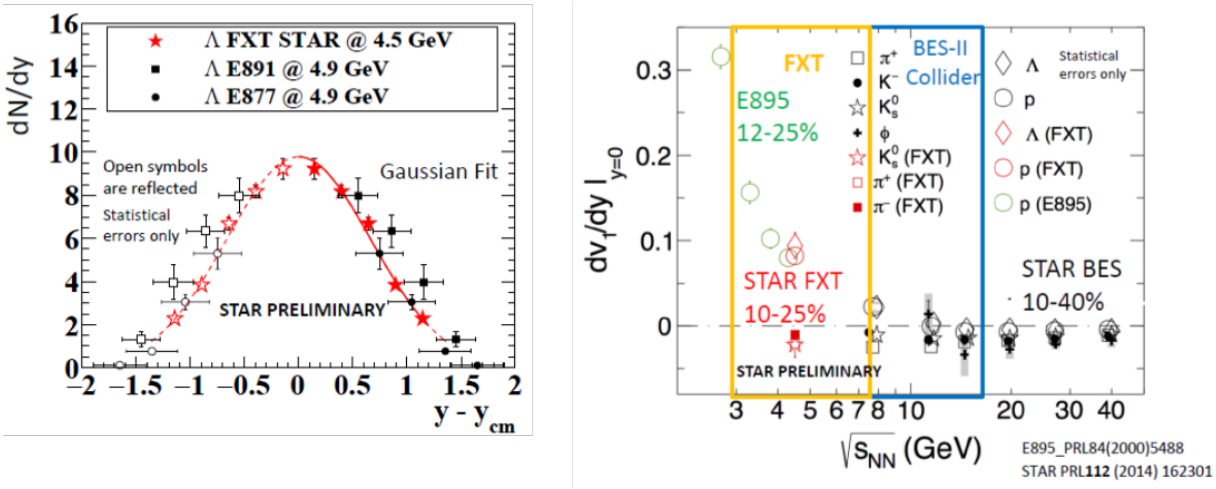

Figure 22: Sample results from the Run 15 $\sqrt{s_{NN}} = 4.5$ GeV Au+Au test run. The Λ rapidity distribution (left) and directed flow measurements for several particle identified species in 10-25% central events (right). The FXT data are compared to other results.

1.2.10 Chiral Magnetic Effect

The chiral magnetic effect (CME) [70, 71] refers to the induction of an electric current ($\vec{J_e}$) by the magnetic field ($\vec{B}$) in a *chiral* system: $\vec{J_e} \propto \mu_5 \vec{B}$. A chiral system bears a nonzero μ_5, which characterizes the imbalance of right-handed and left-handed fermions in the system. The discovery of the CME in high-energy heavy-ion collisions would confirm the simultaneous existence of ultra-strong magnetic fields, chiral symmetry restoration and topological charge changing transitions in these collisions. On average, $\vec{B}$ is perpendicular to the reaction plane ($\Psi_{\rm RP}$) that contains the impact parameter and the beam momenta. Hence the CME will manifest a charge transport across the reaction plane.

In the presence of the CME and other modes of collective motions, we can Fourier decompose the azimuthal distribution of particles of given transverse momentum (p_T) and

pseudorapidity (η):

$$\frac{dN_\alpha}{d\phi} \propto 1 + 2v_{1,\alpha}\cos(\Delta\phi) + 2v_{2,\alpha}\cos(2\Delta\phi) + ... + 2a_{1,\alpha}\sin(\Delta\phi) + ..., \quad (1)$$

where ϕ is the azimuthal angle of a particle, and $\Delta\phi = \phi - \Psi_{\rm RP}$. Here the subscript α (+ or −) denotes the charge sign of the particle. Conventionally v_1 is called "directed flow" and v_2 "elliptic flow" [42]. The parameter a_1 (with $a_{1,-} = -a_{1,+}$) quantifies the electric charge separation due to the CME.

Experimentally the CME has been searched for via charge-separation fluctuations perpendicular to the reaction plane, e.g., with a three-point correlator [72], $\gamma \equiv \langle\cos(\phi_\alpha + \phi_\beta - 2\Psi_{\rm RP})\rangle$, where the averaging is done over all particles in an event and over all events. In practice, the reaction plane is approximated with the "event plane" ($\Psi_{\rm EP}$) reconstructed with measured particles, and then the measurement is corrected for the finite event plane resolution. The expansion of the γ correlator,

$$\begin{aligned}\langle\cos(\phi_\alpha + \phi_\beta - 2\Psi_{\rm RP})\rangle &= \langle\cos(\Delta\phi_\alpha)\cos(\Delta\phi_\beta) - \sin(\Delta\phi_\alpha)\sin(\Delta\phi_\beta)\rangle \\ &= (\langle v_{1,\alpha}v_{1,\beta}\rangle + B_{\rm IN}) - (\langle a_{1,\alpha}a_{1,\beta}\rangle + B_{\rm OUT}), \quad (2)\end{aligned}$$

reveals the difference between the *in-plane* and *out-of-plane* projections of the correlations. The first term ($\langle v_{1,\alpha}v_{1,\beta}\rangle$) in the expansion provides a baseline unrelated to the magnetic field. The background contribution ($B_{\rm IN} - B_{\rm OUT}$) is suppressed to a level close to the magnitude of v_2 in a decaying cluster scenario [72]:

$$\frac{B_{\rm IN} - B_{\rm OUT}}{B_{\rm IN} + B_{\rm OUT}} \approx v_{2,\rm cl}\frac{\langle\cos(\phi_\alpha + \phi_\beta - 2\phi_{\rm cl})\rangle}{\langle\cos(\phi_\alpha - \phi_\beta)\rangle}, \quad (3)$$

where $\phi_{\rm cl}$ is the cluster emission azimuthal angle, and ϕ_α and ϕ_β are the azimuthal angles of two decay products. Note that $v_{2,\rm cl}$ contains both flow and non-flow contributions. By "non-flow", we mean correlations not related to the reaction plane. The flowing cluster can be generalized to a larger portion of or even the whole event, through the mechanisms of transverse momentum conservation (TMC) [73, 74] and/or local charge conservation (LCC) [75].

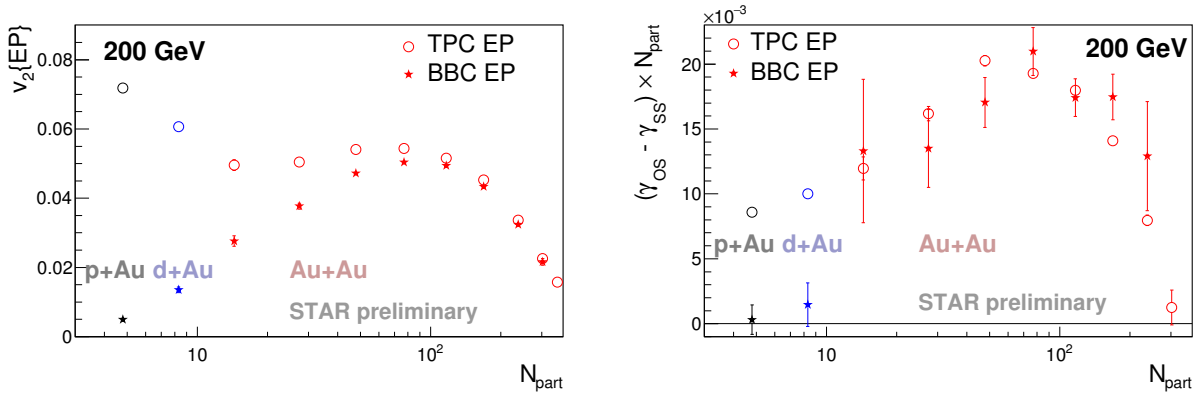

Figure 23: v_2 (left) and $(\gamma_{\rm OS} - \gamma_{\rm SS}) \times N_{\rm part}$ (right) for p+Au, d+Au and Au+Au collisions at 200 GeV, measured with event planes from both TPC and BBC.

Previous STAR measurements [76, 77, 78] have shown $\Delta\gamma(\equiv \gamma_{\rm OS} - \gamma_{\rm SS}) > 0$ for most centrality intervals in Au+Au, Cu+Cu and U+U collisions at 200 GeV, indicative of the charge separation expected from the CME. The non-flow contributions in γ have been

estimated to be non-dominant for mid-central and mid-peripheral Au+Au collisions at 200 GeV [79]. Recently collected p+Au (Run 15) and d+Au (Run 16) data have facilitated the systematic study of the non-flow effects in small systems. Figure 23 shows v_2 (left) and $\Delta\gamma * N_{\rm part}$ (right) for p+Au, d+Au and Au+Au collisions at 200 GeV, measured with event planes from both TPC and BBC. With the TPC event plane, v_2 displays an enhancement at small values of $N_{\rm part}$, demonstrating the short-range non-flow contributions, whereas with the BBC event plane, a pseudorapidity gap of at least 2.8 units is introduced between the event plane and particles of interest, and v_2 goes down monotonically with decreased $N_{\rm part}$. Likewise, $\Delta\gamma * N_{\rm part}$ measured for p+Au stops at a sizable positive value with the TPC event plane, and diminishes with the BBC event plane. The disappearance of the charge separation observable in p+Au is in line with the idea that the magnetic field direction and the second-order participant plane (Ψ_2) are so decoupled that no CME signals should be observed with Ψ_2 in p+Au.

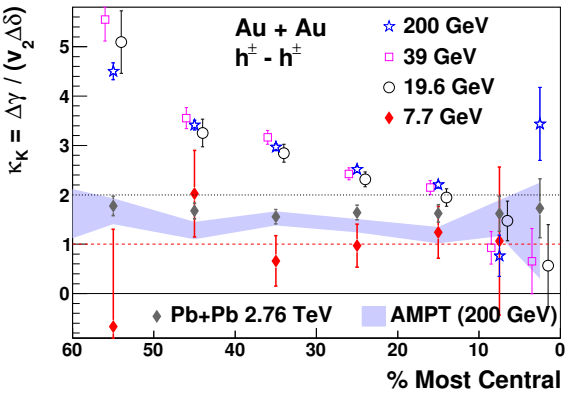

Figure 24: $\kappa_{\rm K}$ vs centrality for Au+Au collisions at 200, 39, 19.6 and 7.7 GeV [80], and for Pb+Pb collisions at 2.76 TeV [81]. The AMPT calculations are also plotted for Au+Au at 200 GeV in comparison.

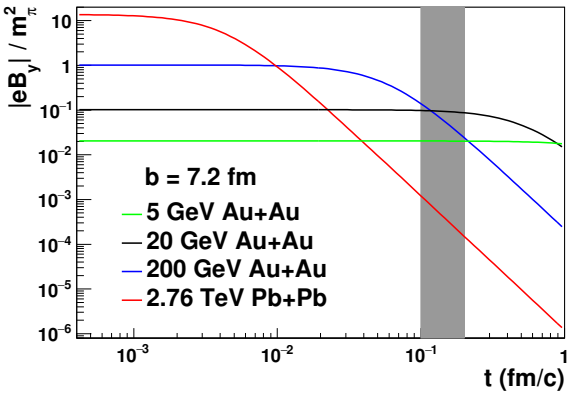

Figure 25: Magnetic field in a vacuum as a function of the evolution time for Au+Au at 5, 20 and 200 GeV and Pb+Pb at 2.76 TeV [82]. The gray band indicates the presumable initial quark production.

In mid-central and mid-peripheral Au+Au collisions at 200 GeV, the consistency between $\Delta\gamma$ measured with the TPC and the BBC event planes suggests that the charge-separation signal is a genuine correlation with respect to the reaction plane, which corroborates the conclusion in Ref [79]. However, the non-flow-suppressed charge-separation observable could still contain flow-related backgrounds. To study the flow-related backgrounds, we define a "normalized" observable, $\kappa_{\rm K} \equiv \Delta\gamma/(v_2\Delta\delta)$, to roughly scale out the influence of flow and the two-particle correlation, $\delta \equiv \langle\cos(\phi_\alpha - \phi_\beta)\rangle$. $\kappa_{\rm K}$ can be compared between data and background scenarios estimated from theoretical calculations or model simulations. Fig. 24 shows $\kappa_{\rm K}$ vs centrality for Au+Au collisions at 200, 39, 19.6 and 7.7 GeV [80], and for Pb+Pb collisions at 2.76 TeV [81]. The background estimation from AMPT stays between 1 and 2, and significantly below the measured $\kappa_{\rm K}$ in $20-60\%$ Au+Au at 200 GeV. For the time being, we assume that the background level has a very weak beam-energy dependence. The data measured at 39 GeV and 19.6 GeV look similar to the 200 GeV results, whereas $\kappa_{\rm K}$ for Au+Au at 7.7 GeV or Pb+Pb at 2.76 TeV seems to be a constant between 1 and 2, consistent with the background level. The CME signal disappears at 7.7 GeV presumably because of the dominance of the hadronic interaction over the partonic one, while it vanishes at 2.76 TeV probably owing to the quickly diminishing magnetic field. Fig. 25 demonstrates the magnetic field in a vacuum vs time for

Au+Au at 5, 20 and 200 GeV and Pb+Pb at 2.76 TeV with an impact parameter of 7.2 fm [82]. Initially the magnetic field at 2.76 TeV is about 13 times stronger than that at 200 GeV, but it decreases much faster. At $t = 0.01$ fm/c, they are almost identical, and by the time when quarks start to be produced (illustrated by the gray band), the magnetic field at 2.76 TeV is already weaker than that at 200 GeV by a few orders of magnitude. Recent ALICE results for Pb+Pb at 2.76 TeV with the event-shape engineering and the CMS comparison between p+Pb and Pb+Pb at 5 TeV [83] also confirm the smallness of the true CME signal at the LHC energies.

STAR has spared no effort to disentangle the possible CME signal and the flow-related background. We have studied central collisions where the charge-separation observable is dominated by the background; the CME should be greatly suppressed under the condition of the minimal magnetic field. Figure 1 of Ref [84] presents $\Delta\gamma$ vs v_2 for central Au+Au $(0-20\%)$ and U+U $(0-10\%)$ collisions. For both Au+Au and U+U, $\Delta\gamma$ tends to vanish at non-zero values of v_2. The dependence of $\Delta\gamma$ on v_2 in the background scenario ($\propto v_2/N$) is non-linear since v_2 decreases and N increases towards central events. It is a challenge to a pure background model to reproduce the positive intercept on the v_2-axis. On the other hand, a simultaneous description of the vanishing $\Delta\gamma$ at non-zero v_2 and its rapid linear growth can be naturally achieved by the variation of the projected magnetic field onto Ψ_2 and the ellipticity (ϵ_2) which drives v_2 [85].

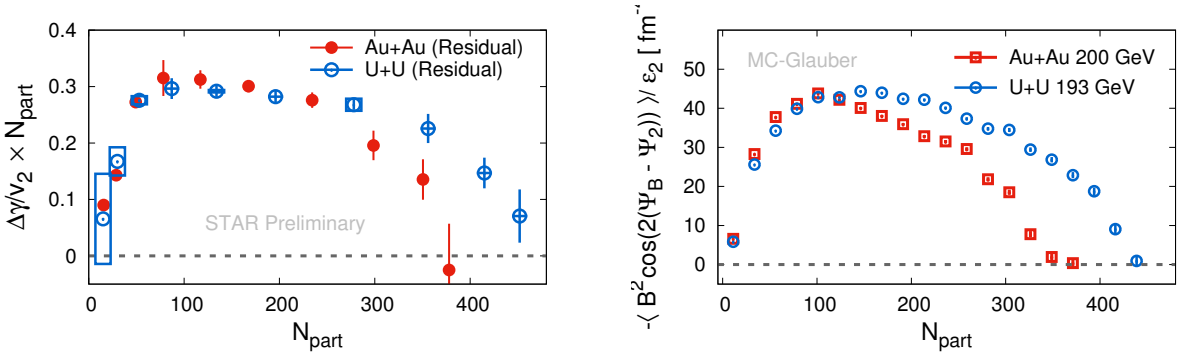

Figure 26: $\Delta\gamma/v_2 \times N_{\rm part}$ vs $N_{\rm part}$ (left) and the magnetic field projection divided by ellipticity (right) for 200 GeV Au+Au and 193 GeV U+U collisions. Positive short-range correlations have been removed from the γ measurements in the left panel.

Another test of the signal/background scenario has been carried out with the comparison of $\Delta\gamma/v_2 \times N_{\rm part}$ between 200 GeV Au+Au and 193 GeV U+U, as shown in Fig. 26 (left). Note that the γ measurements shown here have excluded the positive short-range correlations between particles α and β, which are determined with a multi-component fit to the differential measurement of γ as a function of the pseudorapidity gap between particles α and β. PHENIX has shown that at the same $N_{\rm part}$, the multiplicity is almost identical for 200 GeV Au+Au and 193 GeV U+U [86], thus $\Delta\gamma/v_2 \times N_{\rm part}$ should be constant and almost the same for these two systems, according to the background scenario. Data show two rise-and-fall trends for Au+Au and U+U, respectively. The two trends merge at lower $N_{\rm part}$, and separate at higher $N_{\rm part}$. These very features can be naturally explained by the magnetic field projection divided by ellipticity, as depicted in the right panel of Fig. 26. A uranium nucleus have 13 more protons than a gold nucleus, which in turn causes the difference in the magnetic fields in U+U and Au+Au collisions. The difference in the magnetic field is compensated by the difference in ellipticity at lower $N_{\rm part}$, but becomes overwhelming towards higher $N_{\rm part}$.

1.2.11 Chiral Magnetic Wave

Another complementary transport phenomenon to the CME has been theorized and named the chiral separation effect (CSE) [87, 88], in which chiral charges are separated along the axis of the magnetic field in the presence of finite density of vector charge: $\overrightarrow{J_5} \propto \mu_v \overrightarrow{B}$. In a chirally symmetric phase, the CME and CSE form a collective excitation, the chiral magnetic wave (CMW), a long wavelength hydrodynamic mode of chiral charge densities [89, 90]. The CMW, a signature of the chiral symmetry restoration, manifests itself in a finite electric quadrupole moment of the collision system, where the "poles" ("equator") of the produced fireball acquire additional positive (negative) charge [89]. This electric quadrupole, if boosted by radial flow, will lead to charge-dependent elliptic flow. Let's take pions as an example: on top of the baseline $v_2^{\rm base}(\pi^{\pm})$, the CMW will lead to [89]

$$v_2(\pi^{\pm}) = v_2^{\rm base}(\pi^{\pm}) \mp \frac{r}{2} A_{\rm ch}, \tag{4}$$

where $A_{\rm ch} \equiv (N_+ - N_-)/(N_+ + N_-)$ is the charge asymmetry of the collision event, $r \equiv 2q_e/\bar{\rho}_e$, and q_e and $\bar{\rho}_e$ are the quadrupole moment and the net charge density, respectively.

Previous STAR measurements of the slope in $\Delta v_2(A_{\rm ch})$, r, have shown a rise-and-fall trend as a function of centrality for Au+Au collisions at 200 GeV, as shown in Fig. 27 [91]. This feature resembles the CMW expectation, whereas the UrQMD calculations yield null slopes for $20-60\%$ collisions, where data have significant signals. Recent STAR results for p+Au and d+Au are also plotted in this figure, which are highly consistent with zero, and corroborate the falling trend previously observed at smaller systems.

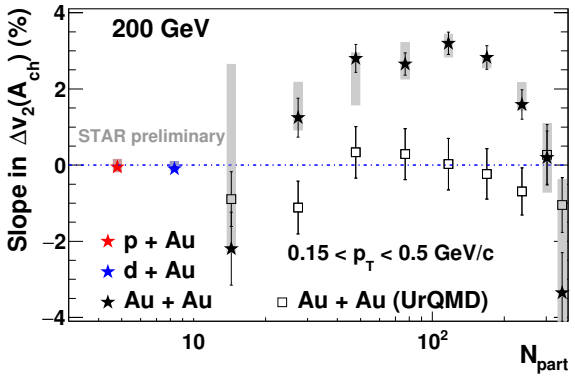

Figure 27: Slope parameter, r vs $N_{\rm part}$ for pions in p+Au, d+Au and Au+Au collisions at 200 GeV [91].

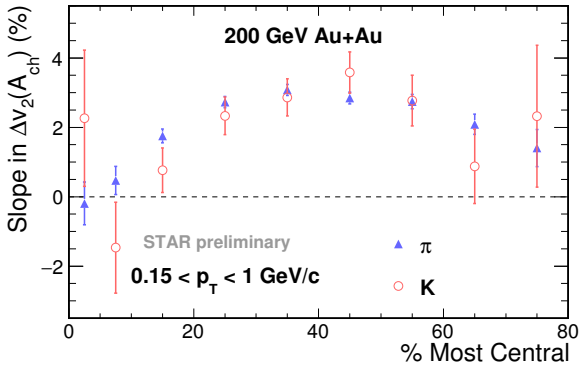

Figure 28: Slope parameter, r vs centrality for pions and kaons in Au+Au collisions at 200 GeV.

It was argued [92] that local charge conservation at freeze-out, when convoluted with the characteristic shape of $v_2(\eta)$ and $v_2(p_T)$, may provide a qualitative explanation for the finite v_2 slope observed from STAR data. A realistic estimate of the contribution of this mechanism turns out to be smaller than the measurement by an order of magnitude [91]. Ref. [92] also proposes a test with the v_3 measurement, and the corresponding slope parameters for v_3 were reported by STAR to be consistent with zero [93], which further suggests the smallness of this effect. A hydrodynamic study [94] claimed that simple viscous transport of charges, combined with certain specific initial conditions, will lead to a sizable v_2 splitting of charged pions. To have their results of pion splitting resemble data, the authors had to invoke a crucial relation between isospin chemical potential and the electric charge asymmetry, which needs to be verified. Furthermore, this model predicts

the splitting for kaons to have the opposite sign and larger magnitude than that for pions. This prediction is contradicted by STAR data, as shown in Fig. 28, where the kaon slopes have the same sign and almost identical magnitude as the pion slopes in the centrality region where the signals are significantly positive.

2 Run 18 Request

In Run 18 our primary request is two 3.5 week runs with collisions of Ruthenium-96 (Ru+Ru) and Zirconium-96 (Zr+Zr) at $\sqrt{s_{NN}}$ =200 GeV. These data will clarify the role of the magnetic field in measurements designed to probe CME and CMW effects. In addition we request 3 weeks of Au+Au collisions at $\sqrt{s_{NN}}$ = 27 GeV to allow for statistically significant Λ and $\bar{\Lambda}$ global polarization measurements. Lastly we request Au+Au collisions at $\sqrt{s_{NN}}$ = 3.2 GeV in "fixed target" mode. $\sqrt{s_{NN}}$ = 3.2 GeV running will enable fluctuation measurements at a collision energy between the HADES measurement at 2.4 GeV and STAR's lowest energy point at 7.7 GeV. More details of the physics cases that drive these requests are given below.

2.1 Collisions of Isobaric Nuclei

STAR has been searching for evidence of chiral magnetic/vortical effects for more than a decade, and so far the experimental observables support the pictures of the chiral magnetic effect and the chiral magnetic wave. To draw a firm conclusion, an effective way is needed to disentangle the signal and the background contributions, the latter of which are intertwined with collective flow. Collisions of isobaric nuclei, i.e. $^{96}_{44}$Ru+$^{96}_{44}$Ru and $^{96}_{40}$Zr+$^{96}_{40}$Zr, present a unique opportunity to vary the initial magnetic field by a significant amount while keeping everything else almost the same. Therefore, isobaric collisions will play a decisive role in verifying/falsifying the CME. Moreover, STAR has observed a significant excess of dilepton production at very low p_T at mid-rapidity in peripheral A+A collisions, which resembles the coherent photon-nucleus interactions in ultra-peripheral events. Collisions of isobaric nuclei will shed light on the origin of this excess.

2.1.1 Chiral Magnetic Effect

In the search for the CME with the γ correlator, the non-flow backgrounds can be suppressed technically, e.g. with event planes at forward rapidities, but the approaches to remove or estimate the flow backgrounds are usually model-dependent and involve large uncertainties. To quantify the CME signal and the flow-related background in the γ correlations, we propose to collide isobaric nuclei of $^{96}_{44}$Ru and $^{96}_{40}$Zr [95], where the magnetic field can be significantly varied while the backgrounds are almost fixed. Ru+Ru and Zr+Zr collisions at the same beam energy are almost identical in terms of particle production, which is illustrated with the Monte Carlo Glauber simulation in Fig. 29 [96]. The ratio of the multiplicity distributions from the two collision systems is consistent with unity almost everywhere, except in $0-5\%$ most central collisions, where the slightly larger radius of Ru ($R_0 = 5.085$ fm) plays a role against that of Zr ($R_0 = 5.02$ fm). For the CME analysis, we focus on the centrality range of $20-60\%$, so that the background difference due to the multiplicity is negligible.

The spatial distribution of nucleons in either $^{96}_{44}$Ru or $^{96}_{40}$Zr in the rest frame can be written in the Woods-Saxon form (in spherical coordinates),

$$\rho(r,\theta) = \frac{\rho_0}{1+\exp\left\{[r - R_0(1+\beta_2 Y_2^0(\theta))]/a\right\}}, \tag{5}$$

where $\rho_0 = 0.16$ fm^{-3} is the normal nuclear density, R_0 and a represent the "radius" of the nucleus and the surface diffuseness parameter, respectively, and β_2 is the deformity of the nucleus. The parameter a is almost identical for Ru and Zr: $a \approx 0.46$ fm. Our current

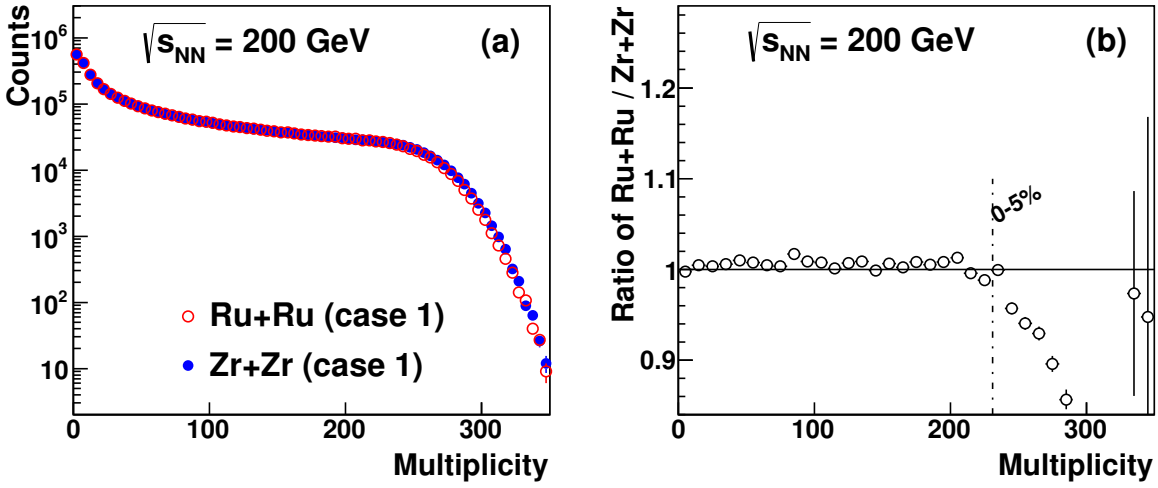

Figure 29: The Monte Carlo Glauber simulation of the multiplicity distributions for ${}^{96}_{44}$Ru+${}^{96}_{44}$Ru and ${}^{96}_{40}$Zr+${}^{96}_{40}$Zr at $\sqrt{s_{\rm NN}} = 200$ GeV (a) and their ratio (b). [96]

knowledge of β_2 of Ru and Zr is incomplete. According to e-A scattering experiments [97, 98] (which will be referred to as case 1), Ru is more deformed ($\beta_2^{\rm Ru} = 0.158$) than Zr ($\beta_2^{\rm Zr} = 0.08$); whereas comprehensive model deductions [99] (case 2) tells the opposite, $\beta_2^{\rm Ru} = 0.053$ is smaller than $\beta_2^{\rm Zr} = 0.217$. Other B(E2) experiments indicate that $\beta_2^{\rm Ru} \approx 0.1$ and $\beta_2^{\rm Zr} \approx 0.045$ [100, 101], and the difference in β_2 between Ru and Zr is very close to case 1. In the following discussion, we still use case 1 and case 2 as two extreme cases, and the most likely result should stay between the limits set by those two cases. We have checked that this uncertainty has little influence on the multiplicity distribution.

The charge difference between Ru and Zr nuclei provides a handle on the initial magnetic field (mostly produced by the spectator protons). Figure 30(a) presents a theoretical calculation of the initial magnetic field squared with correction from azimuthal fluctuations of the magnetic field orientation, $B_{sq} \equiv \langle (eB/m_\pi^2)^2 \cos[2(\Psi_{\rm B} - \Psi_{\rm RP})] \rangle$, for the two collision systems at 200 GeV, using the HIJING model [96]. B_{sq} quantifies the magnetic field's capability of driving the CME signal in the correlator γ. For the same centrality interval, the Ru+Ru collision produces a significantly stronger magnetic field than Zr+Zr.

Panel (b) of Fig. 30 shows that the relative difference in B_{sq} between Ru+Ru and Zr+Zr collisions is approaching 15% (case 1) or 18% (case 2) for peripheral events, and reduces to about 13% (case 1 and case 2) for central events. In our notation, the relative difference in a quantity F between Ru+Ru and Zr+Zr collisions is $R_F \equiv 2(F^{\rm Ru+Ru} - F^{\rm Zr+Zr})/(F^{\rm Ru+Ru} + F^{\rm Zr+Zr})$, and F can be B_{sq}, ϵ_2 or S. The effect of the deformity of the nucleus on the generation of the magnetic field is more distinctive in more peripheral collisions. In Fig. 30(b), we also show the relative difference in the initial eccentricity, R_{ϵ_2}, obtained from the Monte Carlo Glauber simulation. R_{ϵ_2} is highly consistent with 0 for peripheral events, and goes above (below) 0 for the parameter set of case 1 (case 2) in central collisions, because the Ru (Zr) nucleus is supposedly more deformed. The relative difference in v_2 should closely follow that in eccentricity, so for the centrality range of interest, $20 - 60\%$, the flow-related backgrounds stay almost the same for Ru+Ru and Zr+Zr collisions. The slightly non-zero effect will be taken into account in the significance estimation for the CME signal projection, to be discussed later.

For convenience, we define the charge-separation observable $S \equiv \Delta\gamma \times N_{\rm part}$. The focus of the isobaric collisions is to lift the degeneracy between Ru+Ru and Zr+Zr, therefore we express the corresponding S with a two-component perturbative approach to emphasize

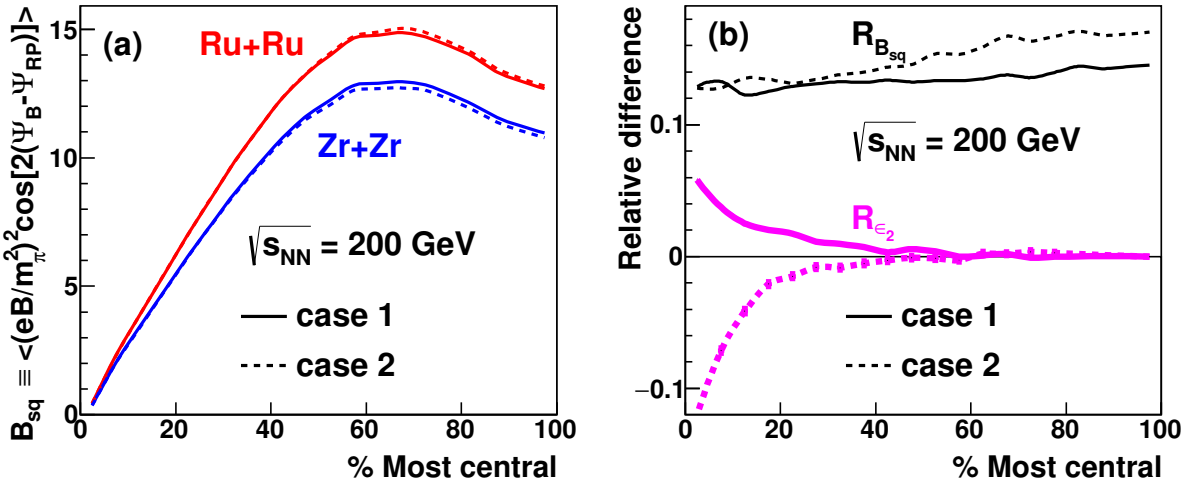

Figure 30: Theoretical calculation of the initial magnetic field squared with correction from azimuthal fluctuation for Ru+Ru and Zr+Zr collisions at $\sqrt{s_{\rm NN}} = 200$ GeV (a) and their relative difference (b) versus centrality. Also shown is the relative difference in initial eccentricity (b). The solid (dashed) curves correspond to the parameter set of case 1 (case 2). [96]

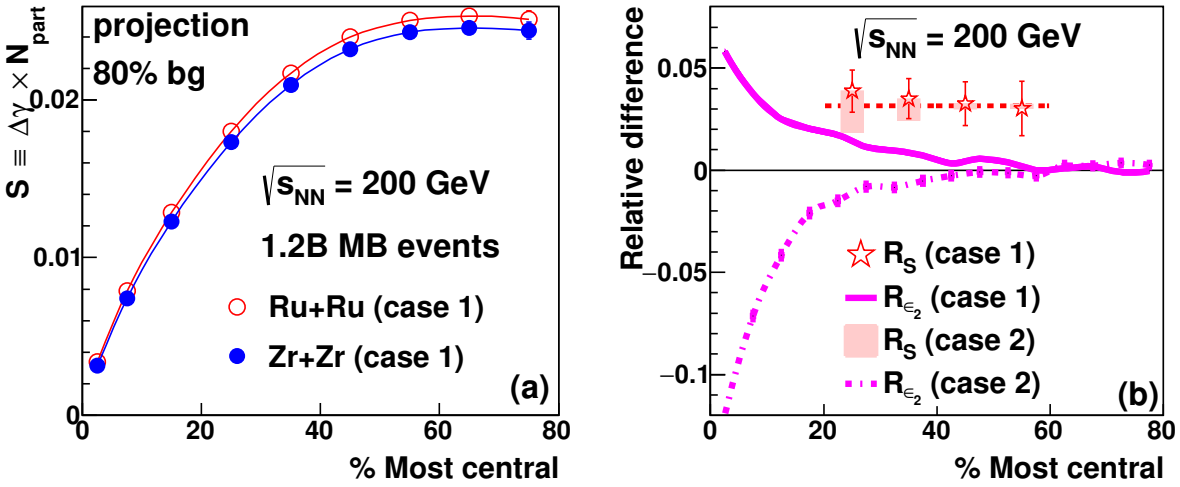

Figure 31: Projection of $S \equiv \Delta\gamma \times N_{\rm part}$ for Ru+Ru and Zr+Zr collisions at $\sqrt{s_{\rm NN}} = 200$ GeV for the parameter set of case 1 (a) and the relative difference in the two (b) versus centrality, assuming the background level to be 80%. The statistical errors are estimated from 1.2×10^9 minimum bias events for each collision type. Also shown in panel (b) is the relative difference in the initial eccentricity from the Monte Carlo Glauber simulation (pink solid and dashed curves).

the relative difference

$$
\begin{aligned}
S^{\rm Ru+Ru} &= \bar{S}\left[(1-bg)\left(1+\frac{R_{B_{sq}}}{2}\right)+bg\left(1+\frac{R_{\epsilon_2}}{2}\right)\right], \\
S^{\rm Zr+Zr} &= \bar{S}\left[(1-bg)\left(1-\frac{R_{B_{sq}}}{2}\right)+bg\left(1-\frac{R_{\epsilon_2}}{2}\right)\right],
\end{aligned}
\tag{6}
$$

where $bg \in [0,1]$ quantifies the background contribution due to elliptic flow and $\bar{S} = (S^{\rm Ru+Ru} + S^{\rm Zr+Zr})/2$. An advantage of this approach is that $R_S = (1-bg)R_{B_{sq}} + bg \cdot R_{\epsilon_2}$,

which is little affected by the detailed implementation of $\bar{S}$. Without loss of generality, we parametrize $\bar{S}$ based on the STAR measurements of $S^{\mathrm{Au+Au}}$ at 200 GeV [79] as a function of $B_{sq}^{\mathrm{Au+Au}}$, and show in Fig. 31(a) the projection of $S^{\mathrm{Ru+Ru}}$ and $S^{\mathrm{Zr+Zr}}$ at 200 GeV, as functions of centrality, with B_{sq} and ϵ_2 obtained for case 1, and the background level of 80%. The statistical errors are estimated based on 1.2×10^9 minimum bias events for each collision type.

The systematic uncertainties in the projection are largely canceled out with the relative difference between Ru+Ru and Zr+Zr, shown in Fig. 31(b); in comparison, we show again the relative difference in eccentricity. For both parameter sets of the Glauber inputs (red stars for case 1 and pink shaded boxes for case 2), the relative difference in S is about 3% for centrality range of $20-60\%$. When we combine the events of $20-60\%$ centralities, R_S is 5σ above R_{ϵ_2} for both parameter sets of the Glauber inputs. Therefore, the isobaric collisions provide a unique test to pin down the underlying physics mechanism for the observed charge separation. As a by-product, v_2 measurements in central collisions will discern which information source (case 1 or 2) is more reliable regarding the deformity of the Ru and Zr nuclei.

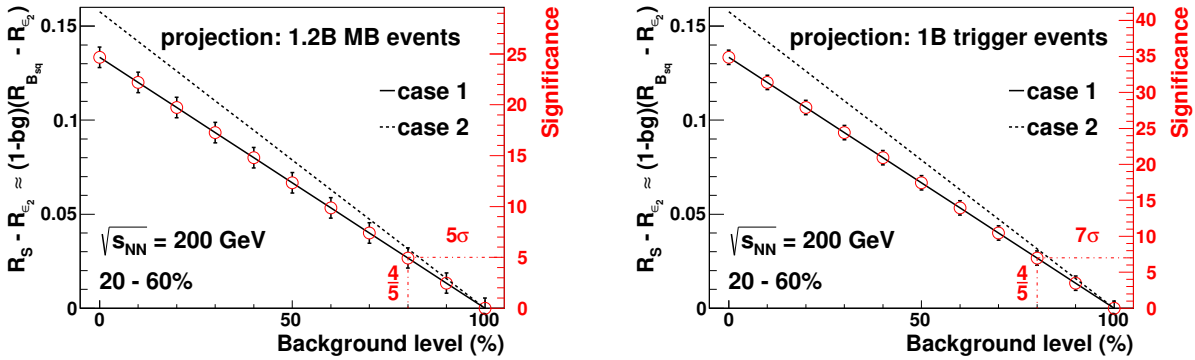

Figure 32: Magnitude (left axis) and significance (right axis) of the relative difference in the CME signal between Ru+Ru and Zr+Zr at 200 GeV, $R_S - R_{\epsilon_2}$ as a function of the background level. Results are estimated with event planes from TPC, based on $20-60\%$ collisions selected from 1.2×10^9 minimum bias events (left) or 10^9 specially triggered events (right).

Given a specific background level, the magnitude and significance of the projected relative difference between Ru + Ru and Zr+Zr can be estimated accordingly, as shown in Fig. 32 based on $20-60\%$ collisions selected from 1.2×10^9 minimum bias events (left) or 10^9 specially triggered events (right). The measurements of the isobaric collision data will determine whether there is a finite CME signal observed in the correlator γ, and if the answer is "yes", will ascertain the background contribution, when compared with this figure. The above results assume the event plane comes from the TPC.

In reality of data taking, the good event rate is about 80%, which converts the requested 1.2 billion into 1.5 billion events. A rough estimate for the RHIC operation to achieve 1.5×10^9 events will be 3.5 weeks for each collision system. For the CME analysis, the focus is on the centrality range of $20-60\%$, therefore a dedicated trigger for mid-peripheral collisions will be very helpful to increase the "useful" statistics. Both the existing Time-of-Flight and the expected EPD are fast detectors that can utilize the particle multiplicity to trigger on events within a wide centrality interval. We propose to take 1 billion events with this trigger and 200 million minimum bias events for each collision type. This trigger is expected to double the useful statistics, and improve the signal significance by a factor of $\sqrt{2}$ as shown in Fig. 32 (right).

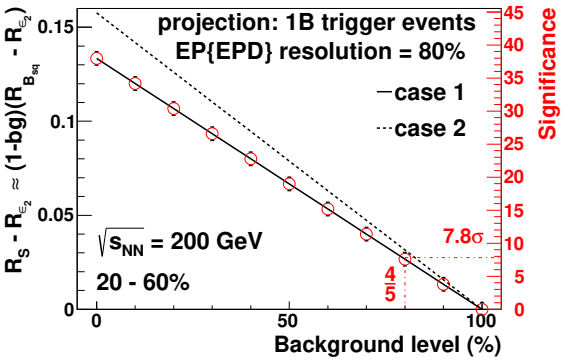

Figure 33: Magnitude (left axis) and significance (right axis) of the relative difference in the CME signal between Ru+Ru and Zr+Zr at 200 GeV, $R_S - R_{\epsilon_2}$ as a function of the background level. Results are estimated with event planes from EPD, based on 20−60% collisions selected from 10^9 specially triggered events.

In 2018, we expect the Event Plane Detector (EPD) to be installed in STAR (to be discussed in Sec 4.2). The pseudorapidity coverage of EPD ($2.1 < |\eta| < 5.1$) will better suppress the non-flow contributions than the TPC event plane, providing an important systematic check for the γ measurements. What's more, with the estimated event plane resolution of $\sim 80\%$ in the isobaric collisions, the results with the EPD event plane will achieve a better significance than those with the TPC event plane at a specific background level, as shown in Fig. 33.

2.1.2 Dilepton Production at Very Low Transverse Momenta

Dileptons (l^+l^-) are produced throughout the medium's evolution and escape with minimum interaction with the strongly interacting medium. Therefore, l^+l^- pair measurements play an essential role in the study of the hot and dense nuclear matter created in heavy-ion collisions. Dileptons in the low invariant mass region (up to $M_{ll} \sim 1$ GeV/c^2) retain information about the in-medium modification of vector mesons while dileptons in the intermediate mass region (extending out to $M_{ll} \sim 3$ GeV/c^2) predominantly originate from charm decays and thermal radiation of the medium.

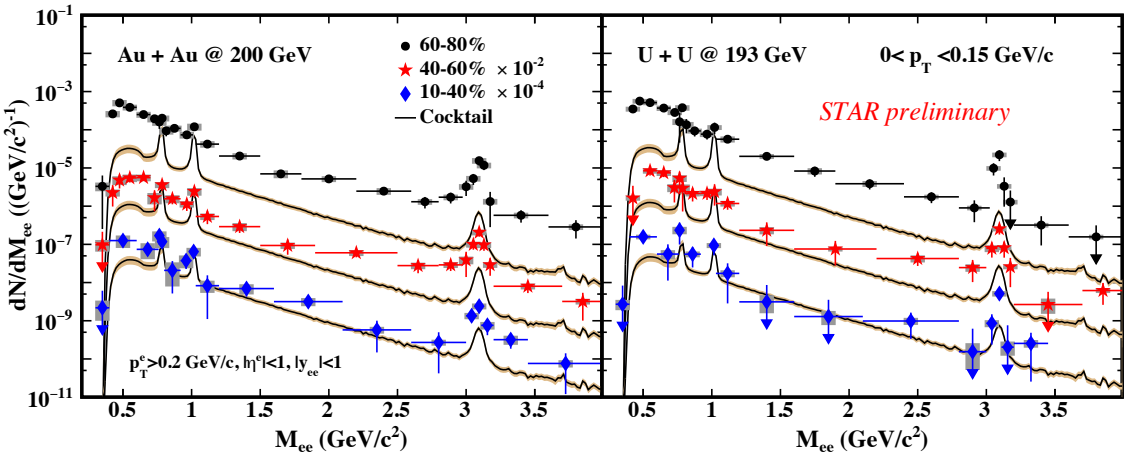

Figure 34: The low p_T ($0 < p_T < 0.15$ GeV/c) e^+e^- invariant mass distribution for Au+Au collisions at 200 GeV (left) and U+U collisions at 193 GeV (right). The invariant mass distributions for collisions with $60-80\%$, $40-60\%$, and $10-40\%$ centrality are shown. For each centrality the corresponding hadronic cocktail contribution is shown as a solid curve with the uncertainty as a shaded region.

Figure 34 shows the e^+e^- invariant mass distribution from Au+Au collisions at 200 GeV and U+U collisions at 193 GeV for $p_T < 0.15$ GeV/c. The e^+e^- invariant mass

distribution is shown for $60-80\%$, $40-60\%$, and $10-40\%$ collision centralities. For each case the expected contribution from hadronic sources (excluding the ρ meson) is shown as a solid black curve. In $60-80\%$ Au+Au and U+U collisions there is a significant excess visible with respect to the corresponding hadronic cocktail. The excess is less significant in $40-60\%$ collisions and the data from $10-40\%$ collisions are consistent with the expectation from the hadronic cocktail. The excess yield with respect to the hadronic cocktail is shown in Fig. 35 for $60-80\%$ Au+Au and U+U collisions along with the additional contributions expected from an in-medium modified ρ and thermal radiation from the QGP. The sum of these additional contributions is insufficient to explain the observed excess.

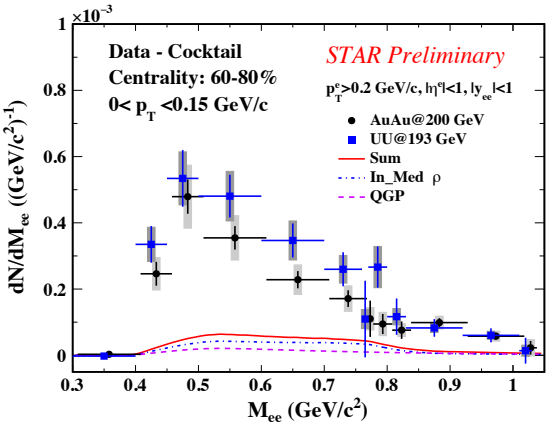

Figure 35: The low p_T e^+e^- excess yield with respect to the hadronic cocktail for Au+Au and U+U collisions with $60-80\%$ centrality. The additional contributions expected from in-medium modified ρ production, QGP thermal radiation, and the sum of the two are shown.

There could be two sources contributing to the low-p_T dielectron enhancement in peripheral collisions: photonuclear [102] and two-photon processes [103]. In the coherent vector meson photoproduction, a photon from the field of one nucleus fluctuates into a virtual quark-anti-quark pair which scatters elastically from the other nucleus, emerging as a real vector meson and then decaying into a dielectron pair. In a two-photon process, a photon from the field of one nucleus interacts from a photon from the other nucleus, emerging as a dielectron pair. These two processes have different dependences on the atomic number (Z) of the nucleus, with the photonuclear cross section proportional to Z^2 and the two-photon cross section proportional to Z^4. Hence, the isobaric collisions can help distinguish these two mechanisms.

Table 6: Results obtained from Monte Carlo Glauber calculations [85] for different collision systems. The magnetic fields are estimated at the time of the collisions ($t = 0$) and at the center of the participant zone. The multiplicity is obtained using a two-component model that is tuned to fit the Au+Au data.

Quantities	U+U	Ru+Ru	Zr+Zr
Centrality (% most central)	$60-80$	$47-75$	$47-75$
Multiplicity ($\|\eta\| < 0.5$)	$12-52$	$12-52$	$12-52$
$N_{\rm part}$	21 ± 1	21 ± 1	21 ± 1
B^2 (fm^{-1})	30.8 ± 0.1	30.1 ± 0.1	26.2 ± 0.1
B^4 (fm^{-1})	1984 ± 4	2121 ± 4	1672 ± 4

In a given heavy-ion collision, the cross sections of the above mentioned processes actually depend on the magnitude of the magnetic field produced by the protons in the

colliding nuclei. In addition to Z, the produced magnetic field also depends on the distribution of the protons inside the colliding nuclei and the impact parameter of the collisions. For realistic estimations of the magnetic field, one must take into account the event-by-event variation. From the Monte Carlo Glauber calculations, we find that $60-80\%$ U+U collisions will produce the same particle multiplicity as $47-75\%$ Zr+Zr and Ru+Ru collisions [85], and therefore the same cocktail contributions and hot medium contributions to the dielectron production. On the other hand, $\langle B^2 \rangle$ and $\langle B^4 \rangle$ are different for these three collision systems. The ratio of $\langle B^2 \rangle$ in $47-75\%$ Zr+Zr (Ru+Ru) over that in $60-80\%$ U+U is 0.85 (0.98), while the ratio of $\langle B^4 \rangle$ is 0.84 (1.07). The results obtained from Monte Carlo Glauber calculations are summarized in Table 6.

Table 7: The expected dielectron data over cocktail ratios in the mass region $0.4-0.76$ GeV/c^2 for $p_T < 0.15$ GeV/c with 1.2 billion minimum-bias isobaric collisions and the projected differences between Zr+Zr and Ru+Ru collisions for the two physics scenarios.

Physics process	data/cocktail $47-75\%$ Ru+Ru	data/cocktail $47-75\%$ Zr+Zr	Difference between Ru+Ru and Zr+Zr
Photonuclear	16.1 ± 0.4	14.3 ± 0.4	1.8 ± 0.6 (3.0σ)
Two-photon	17.4 ± 0.4	14.2 ± 0.4	3.2 ± 0.6 (5.3σ)

With all the above information, we estimate the dielectron data over cocktail ratios in the isobaric collisions with 1.2 billion good events and the projected differences between Ru+Ru and Zr+Zr collisions for the two physics scenarios. The results are shown in Table 7 and Table 8 for two different mass regions.

Table 8: The expected dielectron data over cocktail ratios in the mass region $3.0-3.2$ GeV/c^2 for $p_T < 0.15$ GeV/c with 1.2 billion minimum-bias isobaric collisions and the projected differences between Zr+Zr and Ru+Ru collisions for the two physics scenarios.

Physics process	data/cocktail $47-75\%$ Ru+Ru	data/cocktail $47-75\%$ Zr+Zr	Difference between Ru+Ru and Zr+Zr
Photonuclear	20.0 ± 1.7	17.5 ± 1.7	2.5 ± 2.4 (1.0σ)
Two-photon	17.3 ± 1.7	21.8 ± 1.7	4.5 ± 2.4 (1.9σ)

2.2 Au+Au Collisions at 27 GeV

2.2.1 Global Polarization Measurements at 27 GeV

Global polarization can arise from spin coupling to both the fireball vorticity and the spectator magnetic field. Vortical coupling aligns emitted particle spin with the total system angular momentum, which can be partially transferred to the mid-rapidity fireball. Particle spins may also (anti-)align to the short lived magnetic field (in the same direction as the total angular momentum) via intrinsic magnetic moment coupling. The vortical coupling would be even with respect to baryon number, while the magnetic coupling would

be odd. STAR has seen a positive (6σ) even signal and a small (1.5σ) odd signal for the Λ-$\overline{\Lambda}$ system in the BES-I data.

The magnetic field is poorly constrained by theory and entirely unmeasured experimentally The primary theoretical uncertainty in our understanding of B-field effects [71] concerns its time evolution, which depends strongly on the electric conductivity of the plasma. Calculations with different conductivities differ by a few orders of magnitude [89]; the calculations with conductivity determined in the lattice QCD, yields fields (at the time of a few fm/c) eB of (a few)$\times 10^{-2} m_\pi^2$, similar to our equilibrium-based estimate.

In addition to being of fundamental interest on its own merits, the vorticity and magnetic field present during the evolution of a heavy ion collision are crucial inputs to the Chiral Vortical Effect (CVE) and Chiral Magnetic Effect (CME), respectively. These two effects are among the RHIC program's most exciting and visible topics today.

A conclusive discovery of chiral effects in heavy-ion collisions will generate great attention and press. Global hyperon polarization has nothing "chiral" about it. In a theoretically well-grounded fashion, it measures the average vorticity (ω) and field (B).

To test the hypothesis of a magnetically-induced splitting between the Λ and $\bar{\Lambda}$ global polarization, we propose to focus on a single energy and obtain high statistics there. Collisions at 19.6 GeV and lower energy will be obtained in the BES-II, so we focus on $\sqrt{s_{NN}} > 19.6$ GeV. The high-statistics at one energy will also provide more differential study of possible p_T and rapidity dependence of the global polarization itself. This, in turn, would be important in clarifying potential difference in Λ and $\bar{\Lambda}$ global polarization due to stopping and final-state absorption.

At $\sqrt{s_{NN}} = 27$ GeV we observe a 0.38σ difference between the Λ and $\bar{\Lambda}$ measurements, as can be seen Fig. 36. Also shown in Fig. 36 are the expectations of the enhanced statistical precision from 1B minimum bias events and inclusion of the EPD to determine the first order event plane. The statistical errors on these measurements go as $1/(\mathrm{R}\sqrt{N})$, where N is the number of events and R is the reaction plane resolution. Given that the EPD will improve the first order event plane resolution by an approximate factor 2 at $\sqrt{s_{NN}} = 27$ GeV, its installation will have a significant impact on this analysis [104]. An approximate factor 15 increase in statistics is therefore needed to realize a 3σ splitting in the hyperon polarization (assuming the central value stays fixed) driving our request for 1B minbias events.

While similar high-statistics measurements of global hyperon polarization will eventually be performed at lower energies in BES-II, the scientific impact of getting firm measures of vorticity and B much sooner is high, given the current intensity of research and discussion of CME and CVE oriented analyses. Meanwhile an isobar run with high statistics at low energy in the further future may be necessary if a splitting of hyperon and antihyperon polarization is observed. We are interested in a 2 day test run in run 18 with Zr+Zr collisions, which will determine the luminosity and STAR's data-taking capability of low energy isobar running. These test data will allow STAR to assess the potential of probing the magnetic field on the Λ polarization at energies where observation of the global polarization effect is optimal.

2.2.2 Dilepton Measurements at 27 GeV

In Fig. 37, the preliminary acceptance-corrected excess spectrum for $\sqrt{s_{NN}} = 27$ GeV is shown. Superimposed on the data points are projections of the improved uncertainties of our measurements for two scenarios. The uncertainties for each scenario are based on the measured preliminary uncertainties from the Run 11 run at 27 GeV. Furthermore, it

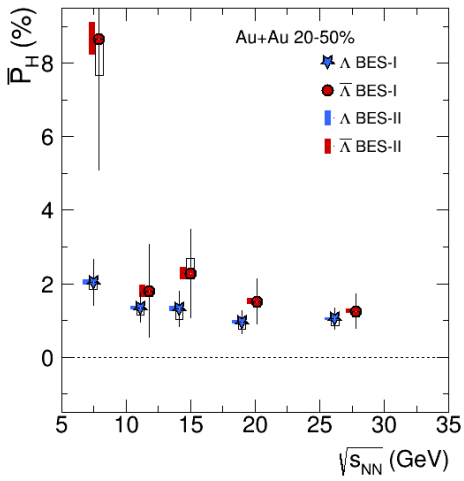

Figure 36: Comparison of the measured Λ and $\bar{\Lambda}$ global polarization as a function of $\sqrt{s_{NN}}$ to estimates of the enhanced precision of the measurements using 1B MB events and the EPD to enhance resolution of the first order plane.

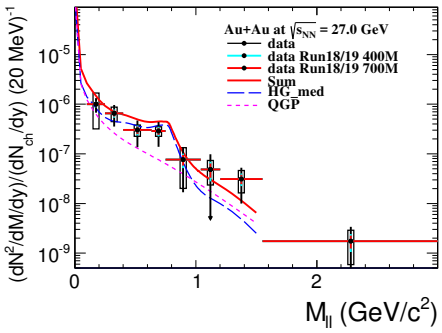

Figure 37: STAR preliminary measurement of the acceptance-corrected dielectron invariant mass spectrum for $\sqrt{s_{NN}} = 27$ GeV. The hadron cocktail has been subtracted. The dotted and striped curves depict calculations by Rapp *et al.* that include a hadron gas (HG) and quark-gluon plasma (QGP).

includes the projected improvement of ∼1.9 for the Au-beam luminosity in Run 18 at 27 GeV, as well as an estimate of the performance envelope of the STAR DAQ rates based on Run 15's performance (saturate at 1.7 kHz). The scenarios involve two cases: (i) running for 2 RHIC weeks at a data-taking efficiency comparable to what was previously achieved for the same energy during Run 11 and (ii) running for 3 full weeks. These scenarios yield approximately 400M and 700M events that pass the analysis criteria for both scenarios, respectively.

As a result, we expect the average uncertainties to reduce by a factor of 2.4 (2-week scenario) up to 3.2 (3-week scenario). Model calculations [105] show that for dielectron masses above that of the ϕ meson the main contribution to the dielectron spectra arrives from the QGP component. The projected improvements in either scenario allow for a first measurement in this intermediate mass range, thus allowing a first potential measurement of the temperature of the hot medium at this energy.

2.3 Au+Au Collisions at 3 GeV

STAR requests two days (100 M events) of running at the fixed target energy of 3.0 GeV. More details of the entire fixed target program are given in Section 3.4. While in Run 18 the forward assets of the iTPC and the eTOF will not yet be available, at this low beam energy the rapidity of the center of mass is 1.05 units and the majority of the mid-rapidity particles are well within the acceptance of the detector in its current configuration. The primary goal of this run is to make a measurement of the higher moments of the net-proton distributions. This measurement will help determine if this $\kappa\sigma^2$ returns to unity at low energy, which was not seen in the recent HADES results. It is important to make this measurement in Run 18, as a 3.5 GeV Au+Au FXT target run is scheduled at NICA for 2019. One hundred million events will be needed because the significance of the $\kappa\sigma^2$ signal has been shown to scale as N^3 (where N is the net-proton multiplicity). The multiplicity of well identified protons measured in the 4.5 GeV FXT test run from Run 15 is one third of that in the 7.7 GeV BES-I data, therefore twenty-seven times higher statistics are needed to achieve a similar level of significance. There were four million good events taken in the the 7.7 GeV BES-I run; 27×4 M ≈ 100 M events are needed. Secondary purposes of taking an FXT data set in Run 18 are to verify the required conduct of operations (i.e. how often to dump the beam and whether the TPC needs to be turned off for dumps) and to optimize the FXT triggers and software.

3 Run 19 Request

In Run 19 STAR proposes to initiate the BES-II. Specific details of the physics goals and required statistics at each energy are given below. In addition STAR is proposing a fixed target program to allow access to energies below those possible at RHIC in collider mode.

In 2014 the STAR Collaboration released a white paper [106] in which it summarized the status of the analysis results from the first phase of the Beam Energy Scan (BES-I) and a proposed a second phase dedicated to low-energy running. In the following years, this white paper was followed by several detector-upgrade proposals [107, 108, 104] which in anticipation of Phase-II will significantly improve STAR's capabilities in terms of acceptance, efficiency, and particle identification. At this time, the STAR collaboration has published 16 "BES-I results" papers, submitted 4, and has another 5 papers in advanced stages of preparation. The results of these analyses are spectacular yet while they remain intriguing they do not allow for definite conclusions.

A disappearance of QGP signatures was indeed seen in the breakdown of constituent quark scaling of elliptic flow at beam energies below 19.6 GeV, in the disappearance of high p_T suppression for energies near 27 GeV and below, and in the collapse of charge separation that is attributed to the Chiral Magnetic Effect below 11.5 GeV, to name a few. There still remains some uncertainty in the interpretation of these observations, *i.e.*, it can be a challenge to unambiguously distinguish between a scenario where QGP production itself disappears, and the alternative picture in which our sensitivity to a QGP signature fades away. Hints of a first-order phase transition are seen in directed flow for protons and net-protons [109]. The measured directed flow signature at intermediate centralities has good statistical significance, but as will detailed in one of the next sections, the best available models show poor agreement with data and a clear physics interpretation requires further study. Meanwhile, searches for critical point signatures in particle ratio fluctuations and in the analysis of higher moments (skewness and kurtosis) of the multiplicity distribution of conserved quantities remain inconclusive, but arguably the net-protons kurtosis shows departure from monotonic dependence on $\sqrt{s_{NN}}$ expected in the absence of CP. These observations narrow-down the most promising region for future searches that will involve improved detectors and higher statistics.

The BES-II proposal requests high statistics (typically 20 times higher than BES-I), as set out in Table 9 for the BES-II beam energies currently envisaged. The searches for new physics will benefit substantially from a much larger rapidity acceptance, lower p_T thresholds, and improved dE/dx resolution, all provided by the iTPC upgrade see [107] and Sect. 4.1. The endcap Time of Flight detector (eTOF) upgrade, [108] and Sect. 4.3, will enable the particle identification at higher momenta in the extended rapidity coverage. The proposed Event Plane Detector (EPD), [104] and Sect. 4.2, will allow the centrality and the event plane to be measured in the forward region, thus reducing the systematic errors due to autocorrelations from mid-rapidity analyses.

In the next subsections we describe the main goals of the proposed BES-II program.

3.1 Structure of the QCD Phase Diagram

3.1.1 Search for the Critical Point: Fluctuation Measurements

Thermodynamics indicates that QCD matter should exhibit a first-order phase transition ending in a critical point, with a crossover transition thereafter [110, 111]. The discovery of the critical point would be the most anticipated outcome of the BES program. Models

Table 9: Event statistics (in millions) needed for BES-II for various observables. Taken from [106].

Collision Energy (GeV)	7.7	9.1	11.5	14.5	19.6
μ_B (MeV) in 0-5% central collisions	420	470	315	260	205
Observables					
R_{CP} up to $p_T = 5$ GeV/c	-		160	125	92
Elliptic Flow (ϕ mesons)	100	150	200	200	400
Chiral Magnetic Effect	50	50	50	50	50
Directed Flow (protons)	50	75	100	100	200
Azimuthal Femtoscopy (protons)	35	40	50	65	80
Net-Proton Kurtosis	80	100	120	200	400
Dileptons	100	160	230	300	400
Required Number of Events	100	160	230	300	400

suggest that the critical point might be signaled by large fluctuations in event-by-event multiplicities of conserved quantities such as net-baryon number, net charge, and net strangeness. These quantities have variances $\langle (dN)^2 \rangle$ that are proportional to the correlation length (ξ) squared. Higher moments like skewness, $S \propto \langle (dN)^3 \rangle \sim \xi^{4.5}$ and kurtosis $\kappa \propto \langle (dN)^4 \rangle \ \xi^7$ vary more strongly with ξ and are argued to offer higher sensitivity to critical fluctuations [112, 113, 114].

Figure 38 presents $\kappa\sigma^2$ for for net charge and net protons [115] (a proxy for net baryons) [116] at mid-rapidity as a function of beam energy for 0-5% centrality and for 70-80% centrality in Au+Au collisions. The net-charge $\kappa\sigma^2$ do not allow us to make strong statements because of the large uncertainties.

The net-proton $\kappa\sigma^2$ values for the 0-5% centrality selection at $\sqrt{s_{NN}} = 19.6$ and 27 GeV are observed to deviate from: (a) the values from 70-80% peripheral collisions which are expected to create small systems which are dominated by two-to-two processes and do not show significant bulk properties; (b) Poisson and hadron resonance gas expectation values, which would correspond to uncorrelated emission and are close to unity; and (c) transport- model-based UrQMD [50, 117] calculations, which represent the expectations of expanding drops of finite hadronic matter which do not experience a phase transition.

Within the current statistical uncertainties we cannot reach a conclusion about fluctuations attributable to a possible critical point. It is essential to re-visit these analyses with the greatly enhanced data to be acquired in BES-II.

Model calculations [118] suggest that the sensitivity of experimental moments analyses strongly depends on the detector's acceptance. The larger the acceptance, the more accurate is the extracted information on moments. STAR acceptance in net-proton cumulants (which are a proxy for net-baryon) is about 30% of the full phase space available for the final-state protons, while in the case of net-charge, it is about half of the full phase space. Due to the upgrades of BES-II, STAR acceptance will be extended by about 50%, significantly improving both analyses. Moreover, the additional STAR coverage will substantially reduce the size of the error on the measurement, effectively reducing the number of events required.

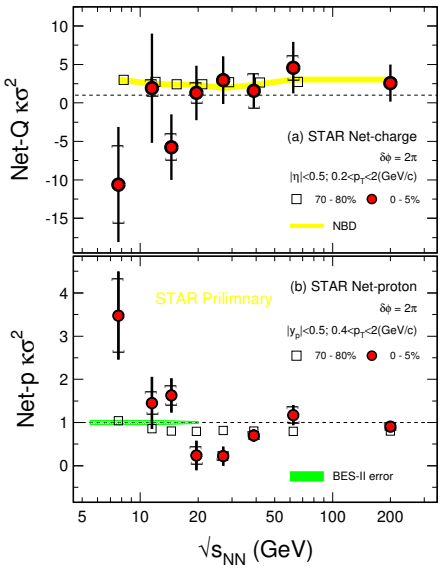

Figure 38: STAR results for beam energy dependence of $\kappa\sigma^2$ for net-protons (lower panel) and for net-charge (upper panel) in Au+Au collisions. Dotted horizontal lines are expectations from Poisson distributions. The green shaped band shows the estimated mid-rapidity statistical errors for the BES-II, assuming the requested events listed in Table 9. Thanks to the iTPC and eTOF, STAR's full capability here will be even better.

3.1.2 Search for the First-Order Phase Boundary: Measurement of Baryon Directed Flow

Directed flow excitation functions have been proposed by Frankfurt theorists as promising observables of evidence for a first-order phase transition, based on hydrodynamic calculations [40, 41, 119]. Figure 39 (left panel), based on a 3-fluid hydrodynamic model [41], presents directed flow for net-baryons as a function of beam energy. Note that the older $\langle px \rangle$ directed flow observable used here is proportional to v_1. A first-order phase transition leads to a softening of the Equation Of State (EOS), and this in turn causes the predicted proton directed flow to change sign from positive to negative near $\sqrt{s_{NN}} = 4$ GeV. The directed flow prediction crosses back to positive again as the beam energy increases further. This phenomenon is referred to in the theory literature as the "softest point collapse" of flow [41].

Directed flow measured by STAR for net-protons is presented in the right panel of Fig. 39, for Au+Au collisions at intermediate centrality [109]. The plotted quantity is the slope of $v_1(y)$ near mid-rapidity. The net-proton slope is a proxy for the directed flow slope of protons associated with baryon number transported from the initial state to the vicinity of mid-rapidity, based on the assumption that produced baryon-antibaryon pairs have similar directed flow and baryon-antibaryon annihilation does not alter the directed flow [109].

The net-proton slope shows a similar minimum to the predicted one, but at the collision energy in dv_1/dy about a factor 4 higher than the hydro prediction shown on the left in Fig. 39. In contrast, there is no hint of this non-monotonic behavior in the UrQMD hadronic transport model [50, 117] (not shown) that has a good record of reproducing observed trends at least at a qualitative level. Theory comparisons that followed the publication of STAR's measurements of directed flow have overall not strengthened either

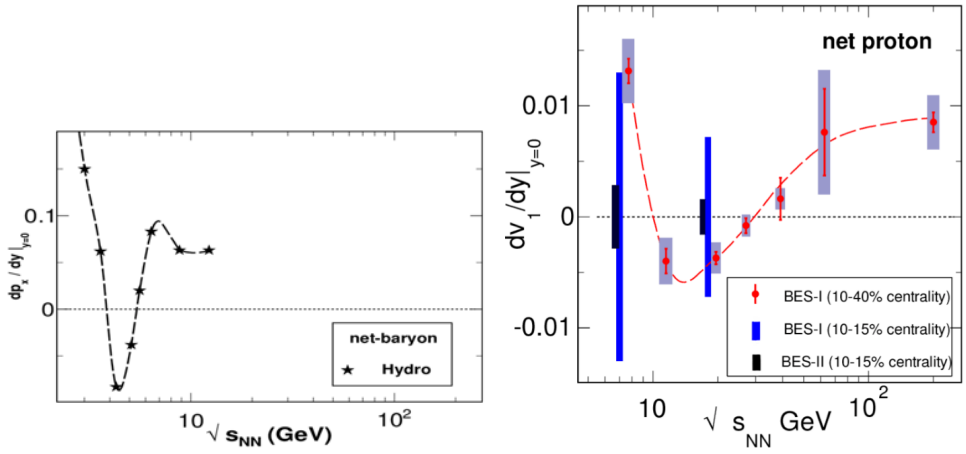

Figure 39: Left: Directed flow prediction in units of GeV/c as a function of beam energy, based on a three-fluid hydrodynamic model [41] whose EOS incorporates a first-order phase transition. Right: Comparison of BES-I 10-40% centrality measurement with 10-15% uncertainties and projected uncertainties for BES-II.

the hadronic or the phase transition interpretations. Specifically, recent hydrodynamic calculations [45] confirm the prediction on the left of Fig. 39 but with a much larger magnitude of v_1 slope than the data, while hydro with a more realistic prescription for particle freeze-out has a much reduced minimum and no sign change [45]. A recent hybrid calculation by the same authors, featuring Boltzmann transport with an intermediate hydrodynamic stage, does not show a minimum or a sign change in v_1 slope for any assumed EOS [45]. The Parton-Hadron String Dynamics transport model does not show a minimum in v_1 slope for any assumed EOS [46].

There is an important connection between the search for a first-order phase transition and the search for a critical point. A confirmed observation of a first-order phase transition would imply that a critical point must exist, by ruling out a hypothesized scenario where the boundary between hadronic matter and QGP is a smooth crossover throughout the phase diagram. Such an observation would also have implications for the allowed and excluded locations in μ_B of the critical point. While model comparisons to date have underlined the importance of further theoretical work in order to reach a confident interpretation, new experimental data are also essential for a definitive conclusion.

Because of the strong non-monotonic behavior observed for protons and net protons, other baryon species like Λs are of special interest (see Sect. 1.2.5), and will have excellent statistics in BES-II. Although BES-I statistics are insufficient for a systematic study of the centrality dependence of directed flow, it is noteworthy that at low BES energies, $v_1(y)$ magnitudes appear to increase roughly a factor of 5 when going from intermediate centralities to more peripheral centralities. Normally, anisotropic flow coefficients exhibit far less centrality dependence over this range, and so this unusual pattern is highly deserving of targeted investigation in BES-II.

After the greatly improved BES-II measurements, any possible future explanation of v_1 data in terms of purely hadronic physics would have to predict the detailed phenomenology of the centrality, rapidity, and transverse momentum dependence of directed flow for various particle species as a function of beam energy. Simulations indicate that the improved statistics and extended rapidity acceptance, in combination with improved RHIC

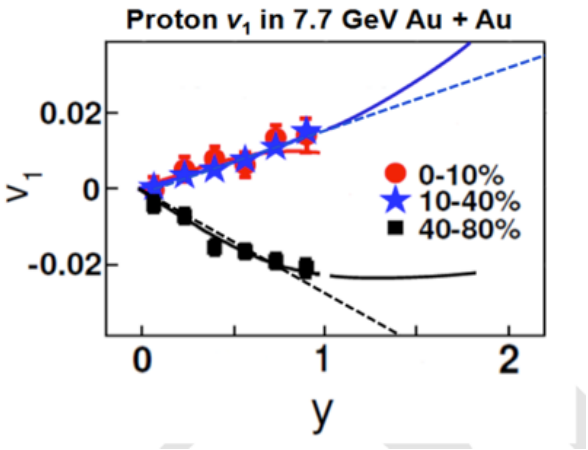

Figure 40: Plotted points show measured directed flow $v_1(y)$ for protons in three centrality bins for Au+Au collisions at $\sqrt{s_{NN}} = 7.7$ GeV. The solid curves are a cubic fit to the measured data points for intermediate and peripheral centralities while the dashed lines are linear fits. For simplicity, only positive rapidities are plotted here.

luminosity in the future, will be sufficient to meet this challenge. The restriction of measurements to the region near mid-rapidity is a serious limitation that must be overcome in order to reach a full understanding of the physics.

Figure 40 illustrates the improved rapidity coverage of the iTPC via the extrapolated cubic and linear fits to $v_1(y)$ for protons at 7.7 GeV measured in BES-I. Clearly the extrapolation to higher rapidity is a major source of systematic error in this analysis and it will be significantly reduced by the extended rapidity coverage of BES-II. The most significant point of Fig. 40 is that with the present rapidity coverage of the STAR TPC, $v_1(y)$ carries insufficient information to go much, if at all, beyond a study of a single parameter like the slope dv_1/dy averaged over the current rapidity acceptance, especially when statistics are limited. In contrast, the much wider $v_1(y)$ coverage of the iTPC opens the possibility to go well beyond a study of the single number yielded by the average slope just described. In light of the fact that proton and net-proton v_1 near $y = 0$ have proven to be a highly promising signature, it is clearly of great interest and importance to extend the same form of analysis to the adjacent regions away from $y = 0$. The BES-I v_1 measurements are based on the rather wide 10-40% centrality sample. The right-hand panel of Fig. 39 compares these measurements with the associated uncertainties for the 10-15% centrality class and the expected impact of the proposed statistics for BES-II on the v_1 measurement for the $\sqrt{s_{NN}} = 7.7$ and 19.6 GeV collision energies. It is expected that such significantly reduced uncertainties will allow for definite conclusions.

3.1.3 Onset of Deconfinement: the Disappearance of QGP Signatures

Every QGP signature will benefit from extended η coverage, improved dE/dx and lowered p_T cut–off. Here we discuss, as an example, the improvement to elliptic flow analysis, which was intensively studied signature in BES-I.

There is evidence that a partonic phase is produced in the early stages of Au+Au collisions at top RHIC energies [34, 35, 36, 37]. Charting the evolution of the established partonic signatures with $\sqrt{s_{NN}}$ from 200 to 7.7 GeV should reveal the value of $\sqrt{s_{NN}}$ where these signatures change or disappear completely. The observation that elliptic flow

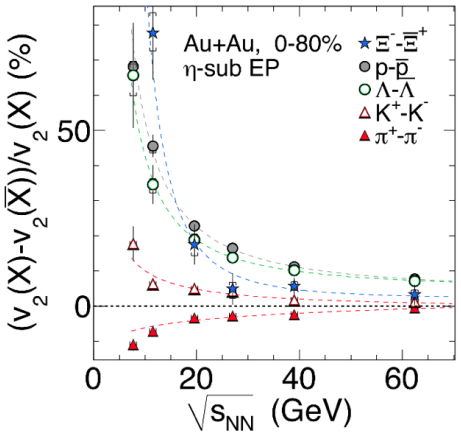

Figure 41: The difference in v_2 between particles and their antiparticles (see legend) as a function of $\sqrt{s_{NN}}$ for 0-80% central Au+Au collisions. The dashed curves are fits with a power-law function. The error bars depict the combined statistical and systematic errors.

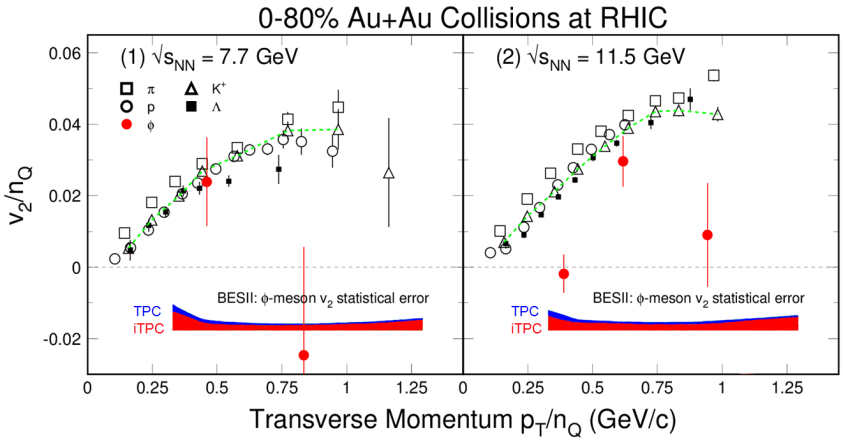

Figure 42: Scaled v_2 of the ϕ meson showing the projected error bars for BES-II with the current STAR TPC (blue band) and with the iTPC (red band).

(expressed by the anisotropy parameter v_2) scales with the number of constituent quarks (NCQ) in a given hadron species indicates that the flow is established early in the collision process, when quarks are the relevant degrees of freedom. In contrast, if the flow had been established during a hadronic phase, then the magnitude of v_2 for each hadron species would scale with its mass. In Fig. 41, the differences between particle and antiparticle v_2 for the six energies 7.7, 11.5, 19.6, 27, 39, and 62.4 GeV are shown.

The results suggest that NCQ scaling, first observed at $\sqrt{s_{NN}} = 200$ GeV [57] may no longer hold at lower energies. As the energy is lowered, the violation of NCQ scaling becomes stronger, and the splitting between mesons and baryons becomes stronger. These observations are consistent with the expectation that the system spends a smaller percentage of the collision duration in the partonic phase as the beam energy is lowered, and that at the lowest BES energies, the system might not reach the QGP phase at all.

The study of the v_2 of particles with a very small hadronic cross section may elucidate to a much higher degree the partonic dynamics and collectivity in heavy-ion collisions.

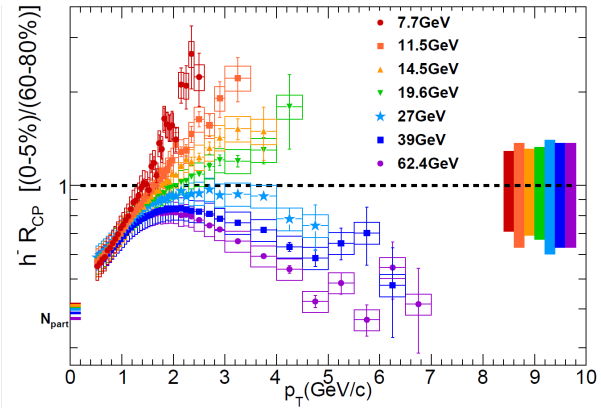

Figure 43: Nuclear modification factor versus transverse momentum for negatively charged hadrons from Au+Au collisions at various $\sqrt{s_{NN}}$ at RHIC. The yield ratios for charged hadrons are taken for 0-5% to 60-80% collision centrality.

The ϕ meson, which is a bound state of the s and $\overline{s}$ quarks, has a small interaction cross section with other hadrons, and freezes out early [120, 121]. Due to the small hadronic interaction cross section of the ϕ meson, its v_2 is almost unaffected by later-stage hadronic interactions, and will have a negligibly small value if ϕ's are not produced via s and $\overline{s}$ quark coalescence in the partonic phase [122]. Therefore the elliptic flow of ϕ meson is particularly interesting because the entire magnitude of its elliptic flow is expected to originate from the partonic phase.

Figure 42 presents $v_2(p_T)$ at 7.7 and 11.5 GeV for several identified particle types, scaled on both axes by the number of constituent quarks. The ϕ meson result, the solid red circles with error bars, illustrate the fact that BES-I statistics for the ϕ are far less than what is needed to reach a useful physics conclusion at these two beam energies. The height of the red band in the lower part of each panel illustrates the expected error with BES-II statistics and with the enhanced midrapidity acceptance of the iTPC. If BES-II were to take data without the iTPC, the errors would increase by an amount represented by the blue band.

Another broadly discussed result from BES-I related to the onset of deconfinement is the R_{CP} measurement shown in Fig. 43 (for all BES-I energies) and Fig. 44 (for 7.7, 11.5 and 19.6 GeV). The high-p_T suppression observed at the top RHIC energies is seen as an indication of the energy loss of leading partons in a colored medium, and the R_{AA} measurements are one of the clearest signatures for the formation of the quark-gluon plasma. Because there was not a comparable p+p energy scan, the BES analysis has had to resort to R_{CP} measurements as a proxy. Still the study of the shape of $R_{CP}(p_T)$ will allow us to quantitatively address the evolution of jet-quenching to lower beam energies.

A very clear change in behavior as a function of beam energy is seen in these data (see Fig. 43); at the lowest energies (7.7 and 11.5 GeV) there is no evidence of suppression for the highest p_T values that are reached. And while we do not expect to reach p_T range of $\sim$5GeV/c for the lowest BES energies, we will be able with the BES-II statistics, to investigate identified particles in the intermediate p_T range, which may allow us to better understand the Cronin effect and the evolution of R_{CP} (see Fig. 44 and Table 9.)

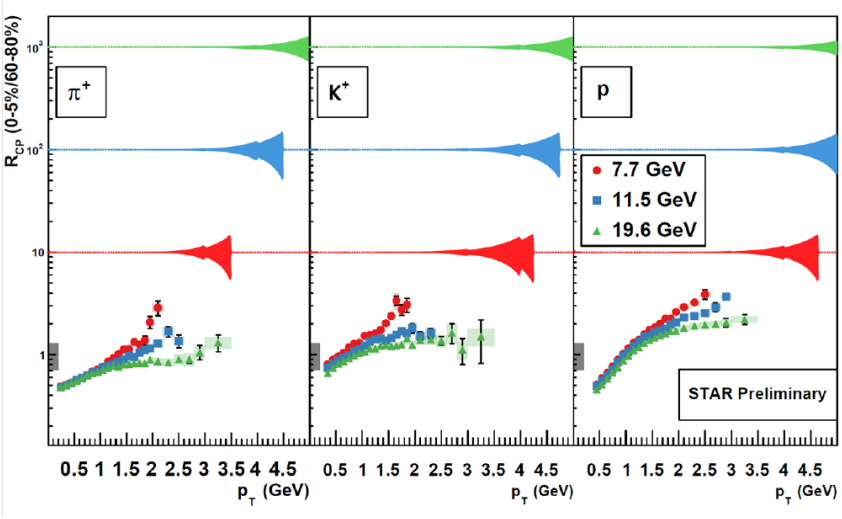

Figure 44: The BES-I $R_{\rm CP}$ data are are shown for p, K, and π for 7.7, 11.5, and 19.6 GeV. The BES-II projected error bands are for the same energies, 7.7 (red, scaled by 10), 11.5 (blue, scaled by 100), and 19.6 (green, scaled by 1000).

3.1.4 Search for Chiral Symmetry Restoration

Dileptons are a crucial probe of the strongly interacting matter created in ultrarelativistic heavy-ion collisions. Leptons are produced during the whole evolution of the created matter and can traverse the medium with minimal interactions. Different ranges in the kinematics of dilepton pairs (mass and transverse momentum ranges) can selectively probe the properties of the formed matter throughout its entire evolution. In the low invariant mass range of produced lepton pairs ($M_{ll} < 1.1$ GeV/c^2), the in-medium properties of vector meson (*i.e.* the mass and width of the $\rho(770)$, $\omega(782)$, and $\phi(1020)$ mesons) can be studied via dilepton decays and may exhibit modifications related to possible chiral symmetry restoration. Additionally, in the higher p_T range, direct photon yields have been derived through dielectron measurements at RHIC, allowing an assessment of thermal radiation. Large acceptance, precision experiments with a broad range of beam energies can provide invaluable insights in this subject.

The dilepton spectra in the intermediate mass range ($1.1 < M_{ll} < 3.0$ GeV/c^2) are expected to be directly related to the thermal radiation of the Quark-Gluon Plasma. However, significant background contributions from other sources have to be taken into account and measured experimentally. Such contributions include background pairs from correlated open heavy-flavor decays. It includes pairs of electrons or muons from the semileptonic decay of a pair of open charm or bottom hadrons, $c \rightarrow l^+l^-$ or $b \rightarrow l^+l^-$; both of which may be subject to in-medium modifications. In the high-mass region ($M_{ll} > 3.0$ GeV/c^2), J/ψ, Υ, and their excited states are used to study the color screening features of the QGP.

It has been generally accepted that the properties of the vector mesons change dramatically from vacuum to the hot and dense medium created in relativistic heavy ion collisions. Observations at SPS and RHIC indicated enhancements of the dilepton yields at low p_T and in the low invariant mass range between the π and ρ mass. These enhancements could not be described with model calculations that involve the vacuum ρ spectral function. The key question is how to connect this modification of the ρ meson to the pos-

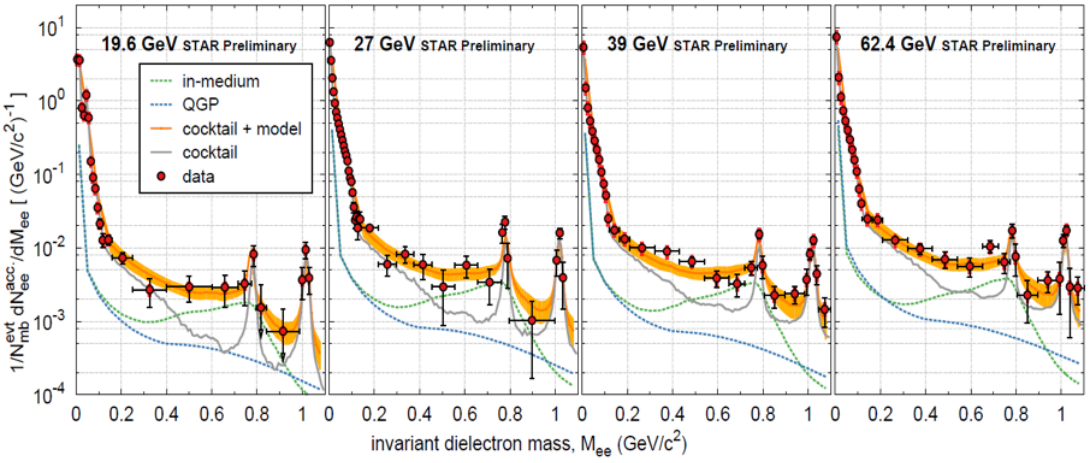

Figure 45: BES-1 preliminary results for the low-mass range dielectron invariant mass spectra at $\sqrt{s_{NN}}$ = 19.6, 27, 39, and 62.4 GeV (red circles). The curves show the empirical contributions from empirical hadronic sources and the sum with a model calculation by Rapp, *et al.* The dotted lines are the in-medium and QGP contributions.

sible chiral symmetry restoration expected at the high temperatures achieved at RHIC and LHC. Dynamic models [123] show that the broadening of the width of the ρ can be attributed to interactions with the surrounding nuclear medium, *i.e.* to the coupling of ρ to the baryons and their resonances. These interactions affect the properties of the ρ even in the cold nuclear matter. In hot nuclear matter, where temperature and/or baryon density is high, these interaction are expected to cause the width to further broaden to the extent that it becomes indistinguishable from the radiation continuum. This continuum coincides with the dilepton thermal radiation from QGP at the phase transition temperature. Measuring the temperature dependence of the dilepton yields at low mass would thus be a key observable.

In relativistic heavy ion collisions, the observed dilepton yields at low mass have contributions from many sources integrated over the entire evolution of a collision. During BES-I running, STAR has collected dielectron data for minimum-bias Au+Au collisions at $\sqrt{s_{NN}}$ = 19.6, 27, 39, and 62.4 GeV. Figure 45 shows the preliminary efficiency-corrected dielectron invariant mass spectra for these four beam energies.

To help further disentangle the various factors that play a role in measuring the dielectron production in the low mass range, we show in Fig. 46 the baryon density *vs.* the collision energy. Here, the total baryon density at freeze-out is approximated by the measured ratio of the sum of proton and antiproton yields over the sum of charged pion yields. The plot shows that above approximately 20 GeV the total baryon density remains almost independent of the beam energy. Consequently, the medium effect on the ρ meson and its dielectron spectrum are independent of beam energy when the dielectrons are emitted close to freeze-out. On the other hand, both the temperature and baryon density at the earlier stage of the collision strongly depend on the beam energy. This, and the lifetime of the system are expected to impact the measured dielectron yields, and could result in measurable anomalies [124].

The dielectron measurements in BES-I have served as an important bridge between those at top SPS and top RHIC energies, and provide an effective tool to study the temperature dependence of the ρ spectral function. These data are used to test models that

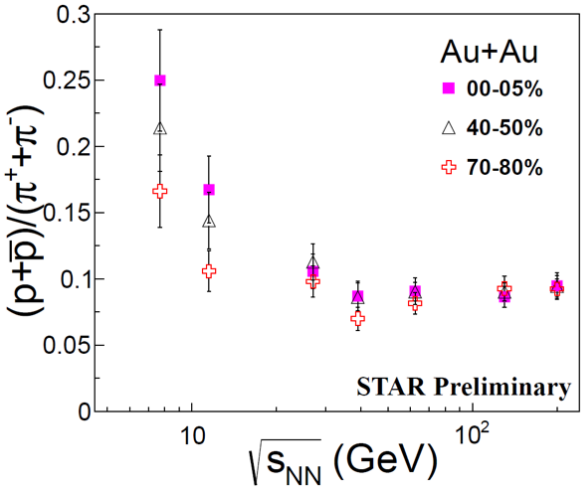

Figure 46: Total baryon density, represented by $(p + \overline{p})/(\pi^+ + \pi^-)$, *vs.* collision energy.

involve a broadened ρ meson. Using these broadened ρ spectral function, verified against inputs from Lattice QCD through Weinberg/QCD sum rules, theorists have demonstrated [125] that when the temperature reaches 170 MeV, the $a_1(1260)$ spectral function is the same as the ρ spectral function. This is a signature of chiral symmetry restoration as the axial vector meson $a_1(1260)$ is considered to be the chiral partner of the ρ meson.

As can be seen from Fig. 46, further lowering the collision energy will see, in addition to a change in temperature, a significant change in the total baryon density at freeze-out. STAR proposes to measure the low-mass range dielectron spectrum down to 7.7 GeV in order to further test the yields against models that connect the broadening of the ρ meson to chiral symmetry restoration. At the same time, measurements of the intermediate mass range will allow STAR to determine how this range may smoothly transition and match to the p_T slopes in the low-mass range. While the charm contribution in the low-mass range will significantly drop with lower collision energies, these rates continue to dominate the intermediate mass range. During BES-II the STAR's muon detection capabilities will allow for independent measurements, through $e - \mu$ correlations, of the charm contribution to the dilepton continuum. Finally, one can also change the total baryon density by shifting the analysis frame from midrapidity towards a more forward rapidity. The combination of the iTPC and eTOF will allow electron identification to be pushed out to larger rapidities (see rightmost panel of Fig. 51 in Sect. 4). The rapidity dependence of the total baryon density will provide a strong and independent observable to study the baryon density's dependence of the low-mass dielectron emission.

3.2 Improvements in the Coverage of Phase Space and the Determination of Freeze-Out Parameters

Statistical-thermal models have proven to be very successful in describing particle multiplicities observed in relativistic collisions of heavy ions and elementary particles (see Sect. 1.2.4. As discussed in Sect. 1.2.4, these models permit the use of experimental particle yields as input and can calculate corresponding thermodynamic parameters such as chemical freeze-out temperature $T_{\rm ch}$ and baryon chemical potential μ_B.

The critical region in μ_B has been predicted to span on the order of 100 MeV [126],

which suggests that the program of measurements in Phase-I of the Beam Energy Scan offers reasonable coverage along the μ_B axis from a few tens of MeV up to at least ∼400 MeV. Furthermore, this interval is predicted to encompass the location of the critical point, if it exists [126]. On the other hand, the Phase-I measurements are subject to basic limitations that strongly motivate a new set of measurements with improved capabilities. Extending the acceptance at low p_T will allow STAR to reduce the fraction of the extrapolated yield which will subsequently be reflected in a similar improvement of the extracted freeze-out parameters.

Current STAR measurements of freeze-out parameters show some deviations from other published data [38], due in part to the fact that the current TPC only offers mid-rapidity coverage. It has been well established that protons have a broader distribution in rapidity than those of mesons or anti-baryons due to partial stopping [127]. As baryon stopping is the key feature in the increase in μ_B at lower energies, it is essential to measure the full proton rapidity distributions [128]. The extended TPC coverage for BES-II will allow proton rapidity density measurements to made to 1.6 units of rapidity which (ignoring spectator protons) accounts for 70% of the proton yield at $\sqrt{s_{NN}} = 19.6$ GeV. Vertices displaced in z from the center of the detector allow one to further extend the coverage to 2.3 units of rapidity. This extended range will allow (on a statistical basis) for almost 4π measurements of particle yields, improving constraints on the thermodynamics

Improving the low p_T coverage also makes possible new physics analyses. A study that is made possible only with the lower p_T thresholds of the iTPC involves measurement of the effect of the Coulomb acceleration of the pions. The effect is seen as an enhancement of ratio of π^-/π^+ for p_T below 100 MeV [129]. By studying the details of the low-p_T pion spectra, one can determine the Coulomb potential of the source, which is related to the stopping of the protons as these participating protons bring a net positive charge to the interaction region [130].

3.3 Proposal for BES-II

The BES-I scientific program has localized the most interesting regions and has identified the observables which are likely to be the most discriminating for understanding the QCD phase structure. However, several of the key measurements were found to require higher statistics in order to provide a quantitative physics conclusion. Therefore, we propose to run a second phase of the beam energy scan (BES-II) which is driven by the precision requirements of this suite of physics observables. In Table 9 [106] we outline the event statistics that is required to make a precision measurement of each proposed observable at each proposed energy.

The main driver for the numbers of events needed in BES-II program are three observables: (1) net-proton kurtosis, (2) v_2 of ϕ meson and (3) dielectron production. The bullets below provide an overview of these observables:

Improved $\kappa\sigma^2$ for net-protons: The search for CP location requires quantitative measurements of the variation of of net-proton $\kappa\sigma^2$ with beam energy. The current measurements have large statistical uncertainty at all collision energies from $\sqrt{s_{NN}} = 7.7$ to 27 GeV. These errors preclude any conclusion of a non-monotonic or monotonic variation of the observable with beam energy. We will need to achieve a statistical error of less than 10% on $\kappa\sigma^2$ for each beam energy in order to determine if the suggestive features of the net-proton higher moments shown in Fig. 38 genuinely establish a non-monotonic behavior which is consistent with a CP. The estimated statistical errors, for the BES-II energy region $7.7 < \sqrt{s_{NN}} < 19.6$ GeV, for net-proton are shown in Fig. 38 by the green

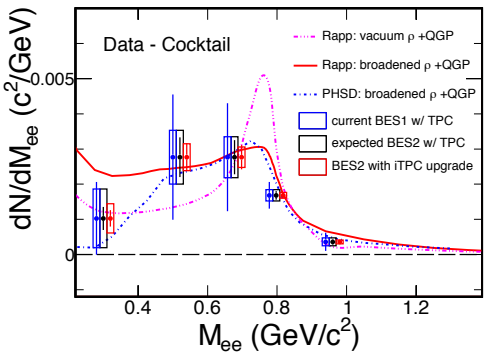

Figure 47: Dielectron invariant mass distribution for Au+Au at $\sqrt{s_{NN}} = 19.6$ GeV.

shaded band assuming the required number of events listed in Table 9. The requested high statistics will allow us to pursue the net-proton distribution studies at higher orders (higher than the 4$^{\text{th}}$) where one expects increased sensitivity to the criticality. In addition, we will also study the higher moments of the net-kaons with better accuracy.

Improvements in v_2 of ϕ mesons and testing of NCQ scaling: This measurement will allow us to quantitatively address the suspected decrease, followed by an absence, of partonic collectivity below $\sqrt{s_{NN}} = 19.6$ GeV. It is necessary to make measurements up to $p_T = 3$ GeV/c with a statistical error of less than 10% on v_2. From this resolution requirement we can estimate the statistics necessary (see Table 9) for BES-II to reach transverse momenta beyond 2.5 GeV/c even at the lowest energies. This will allow us to test in NCQ scaling detail for many particle species, including multi- strange particles.

The projection of the statistical errors for the ϕ meson v_2 for BES-II are shown by the shaded bands in both plots in Fig. 42. As shown in Table 9, 100M and 200M useful minimum-bias events are required from the Au+Au collisions at 7.7 and 11.5 GeV, respectively. These measurements will answer decisively the question how much ϕ meson flow there is compared to that of light quark hadrons. Lack of the collectivity of the ϕ meson will provide clear evidence of the hadronic interaction dominated medium in the low energy heavy ion collisions.

Improvements in the low-mass dilepton measurements: The event size of the data sets that were collected during BES-I for energies below 19.6 GeV have been too small to allow for meaningful measurements in the low-mass range of the dielectron spectrum, let alone in the intermediate mass range. The proposal for measurements in the context of BES-II would therefore not be as much as an improvement, but rather a first measurement of the dielectron invariant mass spectrum in this particular collision energy range. In Fig. 47, the measured statistical (blue error bars) and systematic (blue boxes) uncertainties are shown for $\sqrt{s_{NN}} = 19.6$ GeV. The proposed dielectron event statistics, summarized in Table 9, will allow the BES-II measurements to have statistical uncertainties (black error bars) that are comparable to those in the previously published 200 GeV papers [131, 132]. The systematic uncertainties will be improved by the iTPC upgrade (red boxes). The upgrade will also have an appreciable impact on the statistical uncertainties thanks to an increased acceptance at low p_T. The combined improvement of the systematic and statistical uncertainties will allow the BES-II data to better constraint different models that within BES-I uncertainties could otherwise not be distinguished.

The improvement needed in the intermediate mass range is estimated based on the sta-

tistical uncertainties of the dielectron mass slope from the same BES-I data set at $\sqrt{s_{NN}} =$ 19.6 GeV. A factor of 10 more (minimum-bias) events would bring that uncertainty to about 10%. This is comparable to the requested improvement in statistical uncertainty for the low-mass range measurements. During BES-II STAR's muon detection capabilities, thanks to the 2014 MTD upgrade [133], will allow for independent measurements through $e - \mu$ correlations of the charm contribution to the dilepton continuum. In addition, with its trigger capabilities, the MTD will allow to efficiently select on the dimuon channel, which suffers significantly less from the large backgrounds that complicate dielectron measurements.

3.4 The FXT Program

3.4.1 Motivation for the FXT Program

In the normal collider mode, the lowest collision energy available at RHIC is 7.7 GeV. The fixed-target (FXT) program at STAR, with the iTPC and eTOF upgrades, will enable the energy scan to be extended to also cover the range from 3.0 to 7.7 GeV. It is important to measure key observables at energies lower than 7.7 GeV for several reasons:

- There are theoretical calculations suggesting that the mixed phase is entered at energies well below 7.7 GeV [134].
- NA49 has reported that the onset of deconfinement occurs at 7.7 GeV [135].
- Some of the QGP signatures (local parity violation [80] and narrowing of balance functions [136]) show signs of disappearing at 7.7 GeV. We need to extend the energy range so that we can confirm that these signatures have indeed turned off.
- The BES-I critical point search has shown intriguing results for the net proton fluctuations (see Fig. 38). Predictions are that these fluctuations rise and fall in the region of the critical point. The rise (see at 7.7 GeV in Fig. 38) should return to the baseline of unity at lower energies. This return to unity is not seen on the recent HADES results at 2.4 GeV and needs to be checked with lower energy data at RHIC.

The BES-I program was first proposed in the Run 7 STAR BUR; at that time energies of 4.6 and 6.3 GeV were proposed. In the Run 9 STAR BUR, 100k events were requested at 5.0 GeV. The collider tried circulating beams at 5.5 (Run 9) and 5.0 GeV (Run 10), but because the luminosity is proportional to γ^3 (the relativistic γ of the individual ion beams), operating below 7.7 GeV proved to be impractical. The FXT program provides a practical way of acquiring data below 7.7 GeV and was included conceptually in the 2014 BES-II proposal.

In order to determine the best conduct of operation for a FXT program at RHIC, a gold target was installed inside the beam pipe at STAR in Run 14. The target was 1 cm in height; 6 cm in width, and 1 mm thick. The target was positioned 2 cm below the beam axis and 2.1 meters to the West of the center of the detector (see Fig. 48).

The iTPC and eTOF upgrades improve the acceptance of STAR for the FXT.

- The low-p_T threshold values are defined by energy loss in the backplane of the TPC.
- The η limit of the barrel TOF system is 1.47. The eTOF system covers $\eta = 1.52$ to 2.24.

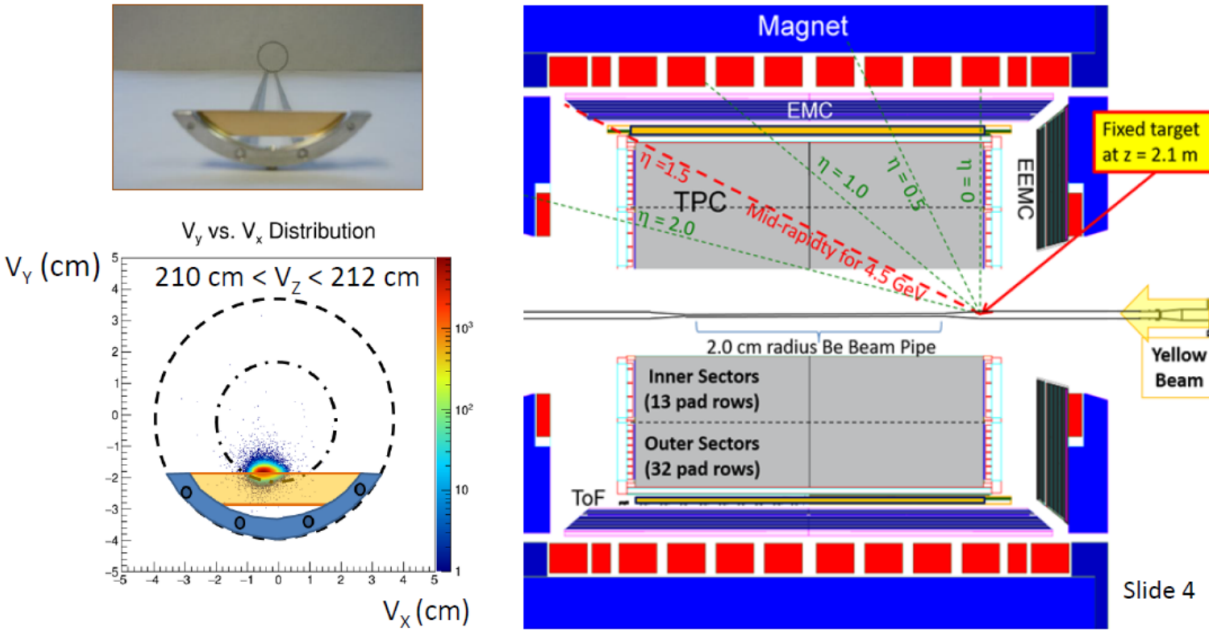

Figure 48: The top-left panel shows an image of the internal gold target. The lower-left panel shows the distribution of vertices with respect to the target. The right panel shows a side view of the STAR detector and the z location of the target.

- The track length in the STAR TPC for particles with $\eta > 0.88$ is longer in fixed-target events. Therefore, the dE/dx resolution for these tracks is better than for tracks with similar η values in collider events.
- The flight path for particles with $\eta > 0.96$ is longer in fixed-target events. Therefore, the TOF PID limits for these tracks extend to higher momentum than for tracks with similar η in collider events.

The acceptance and PID ranges for fixed-target events are shown in Fig. 49.

From the point of view of conduct of operations, it was concluded that dedicated runs in which the elevation of the circulating beam is lowered to graze the top edge of the target can safely deliver a sufficient luminosity to fill the DAQ bandwidth of STAR. For FXT events, STAR can take data at 2 kHz; therefore STAR can accumulate 50 million events per day (also data taking 60% of the time).

3.4.2 FXT Physics Program

Exploring the phase diagram of QCD matter requires that at each collision energy there is sufficient yield (both $y_{\rm CM} = 0$ and full acceptance) of each species to determine the chemical equilibrium T and μ_B values. The coverage maps shown in Fig. 49, demonstrate that we have acceptance for π, and p from $y_{\rm CM} = 0$ to $y_{\rm target}$ for all fixed-target energies except 7.7 GeV, where even with eTOF PID, the p acceptances do not reach $y_{\rm CM} = 0$ (the K acceptances fall between those of the π and p). The efficiency for hyperon reconstruction is a convolution of the single particle acceptances. This will make possible y-dependent measurements of K^0_S, Λ, and Ξ^-. Currently, there is only a single Ξ^- measurement for collision energies below 7.7 GeV [137]. The STAR fixed-target program will map out the turn on of Ξ production with collision energy. Measurements of Ω, $\bar{\Lambda}$, and $\bar{\Xi}^+$ have not

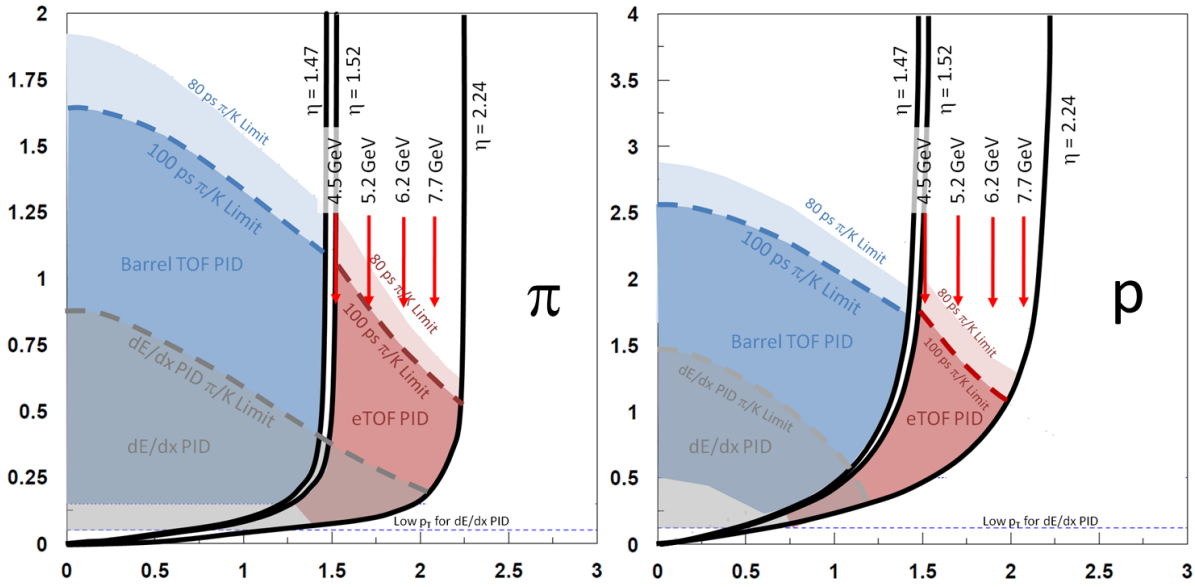

Figure 49: Acceptance maps in p_T vs. y space for the STAR detector in FXT mode. The regions in pink require the iTPC and eTOF upgrades.

been made at these energies previously. Studying the onset of the production of these species could be possible with the fixed-target program using the eTOF.

NA49 has argued that the onset of deconfinement is achieved at 7.7 GeV [135]. This result is based on a set of inclusive observables: there is a kink in the rate of increase of the pion production with collision energy, there is a step in the slope parameter of the kaon spectra, and there is a peak (horn) in the K^+/π^+ ratio. We will study all of these inclusive observables. In addition, the fixed-target program will allow us to track other QGP signature observables, studied in BES-I, spanning a collision energy range from 3.0 to 19.6 GeV (μ_B from 720 to 205 MeV). Observables that will be studied in the fixed-target program:

- Number-of-constituent-quark scaling of elliptic flow is a key QGP signature [138]. The results from BES-I show the N_{CQ} scaling is exhibited independently for particles and anti-particles [57]. At fixed-target energies, the N_{CQ} scaling for particles is expected to break. The elliptic flow is a mid-rapidity observable, and PID is necessary in order to observe the N_{CQ} scaling.

- One form of balance function is a rapidity correlator. This correlator is sensitive to QGP formation [139]. The BES-I data show the balance function narrowing signal decreases with decreasing beam energy. This signal is almost, but not quite, gone at 7.7 GeV [136]. Lower energy measurements are needed to demonstrate that this signature disappears. A key to the sensitivity of this measurement is the width of the total rapidity window.

- Strangeness enhancement is seen as an important QGP signature. The energy range covered by the fixed-target program sees the opening of several strange particle production channels. The strange particle production is maximum at mid-rapidity, and cleanly identifying weakly decaying strange hadrons requires clean PID for the daughters.

Assuming that there is a first-order phase transition, the concept of a single "onset of deconfinement" is an oversimplification. Depending on the universality class of the phase transition, there may be a spinodal decomposition which would imply a mixed-phase region with a negative compressibility. Rather than a single "onset", there may actually be several interesting onsets: the lowest energy which causes some fraction of the system to enter the mixed phase region, the energy at which the system spends the maximum amount of time in the instability regime, and the energy at which the system passes into the pure QGP phase. In order to understand the nature of the phase transition, we propose to study several observables which are expected to have sensitivity to the compressibility. These observables include:

- The directed flow of protons, which offers sensitivity to the early compressibility. Most of these particles are transported participants recoiling off the interaction region [109, 140, 45, 46, 47, 44]. We will study the evolution of the mid-rapidity "wiggle" which is particularly sensitive to compressibility and is known to be absent [141] at the lower end of the proposed fixed-target beam energy range.

- The tilt angle of the pion source, measured through femtoscopy [142, 143, 144].

- The volume of the pion source, measured through femtoscopy [145].

- The width of the pion rapidity density distribution, which has been argued to be sensitive to the speed of sound in nuclear matter [146]. This study relies on the ability to characterize the shape of the rapidity density distribution. Measurements with sufficient rapidity acceptance are required in order to understand the shape of the distribution.

- The elliptic flow of protons, which has been shown to change sign at a fixed-target beam energy of 6 AGeV ($\sqrt{s_{NN}} = 3.5$ GeV) [147]. This sign change of v_2 is explained by the transit speed of the projectile nucleus through the target nucleus matching the expansion speed from compression (speed of sound).

- The Coulomb potential of the pion source provides an independent means of assessing the source volume, being affected by the expansion velocity of the system [148].

- The life-time of the emitting source, measured through low-mass dileptons [149].

The observation of enhanced fluctuations would be the clearest evidence that the reaction trajectory of the cooling system had passed near the possible critical end point on the QGP/hadronic gas phase boundary. Recent analyses of the higher moments of the net-proton distributions have suggested the possibility of enhanced fluctuations at 7.7 GeV [115]. These results require higher statistics to improve the significance. It has also been shown that the significance of the $\kappa\sigma^2$ signal scales as N_p^3.

An important test to determine if the enhanced fluctuations are related to critical behavior would be to see the fluctuation signals return to their baseline levels at energies below 7.7 GeV. The energies of the fixed-target program will provide these important control studies, allowing critical behavior searches to be extended to higher μ_B. Clean PID is essential for this analysis and its sensitivity has been shown to depend strongly on the efficiency and acceptance. At 4.5 GeV, test run data indicate that we accept 20% of all protons using the current configuration of the TPC. This would drop to 5% for the 7.7 GeV fixed-target energy. The key mid-rapidity coverage of the eTOF raises

these acceptance numbers to 50% and 20% respectively (increasing the significance of the results by a factor of 15 to 65). Although there are some fluctuation analyses performed by the NA49 collaboration [150], the more sensitive higher moments studies have been done only by STAR [115, 151], PHENIX [152], and are being studied by HADES at 2.42 GeV. There were no critical fluctuation studies performed at the AGS so the fixed target program will provide the first data in this energy regime.

Dilepton experiments have been an important part of the physics program at almost all heavy-ion facilities, with the notable exception of the AGS. At the lowest energies, HADES measured e^+e^- productions in Au+Au collisions at $\sqrt{s_{\rm NN}} = 2.42$ GeV. In the SPS heavy-ion program, dilepton data were taken by experiments Helios-3, NA38/50, CERES, and NA60. And at RHIC, both PHENIX and STAR have dilepton capabilities. The eTOF detector will provide electron ID at mid-rapidity for all energies of the fixed-target program. This provides the first opportunity to study the evolution of the low-mass dilepton excess in this collision energy region in which the low-mass yield might be also sensitive to the emitting source temperature in addition to being sensitive to the total baryon density. These dependencies will help us to understand the mechanism of in-medium ρ broadening which is the fundamental probe of chiral symmetry restoration in hot, dense QCD matter.

The first species of hypernuclei, ${}^3_\Lambda$H and ${}^4_\Lambda$H, were discovered in the 1950s [153]. Several isotopes of hyper-helium and hyper-lithium have been found in kaon beam s-transfer reactions. In heavy-ion collisions, light nuclei are formed through coalescence of nucleons. As the energy is raised, nucleons can coalesce with hyperons to form light hypernuclei. At even higher energies, anti-nucleons can coalesce to form light anti-nuclei. This coalescence mechanism has allowed STAR to make the discoveries of anti-hyper-tritium (${}^{\overline{3}}_{\overline{\Lambda}}\overline{\rm H}$) [154] and anti-alpha ($\overline{^4{\rm He}}$) [155].

The energy regime covered by the fixed-target program (3.0 to 7.7 GeV) should be optimal for the formation of matter (as opposed to anti-matter) hypernuclei. At energies below 3.0 GeV, few hyperons are produced, whereas at energies above 8 GeV, the increased production of anti-baryons stifles formation of composites of matter particles. Meaningful samples of ${}^3_\Lambda$H and ${}^4_\Lambda$H will be observed at all the fixed-target energies. Simulations have been made assuming eTOF coverage and PID. The statistics are expected to be comparable to STAR data samples from 200 GeV collider data; this will allow a precise measurement of the light hypernuclei lifetimes and a mapping of the ${}^3_\Lambda{\rm H}/({}^3{\rm He}\times(\Lambda/p))$, and ${}^4_\Lambda{\rm H}/({}^4{\rm He}\times(\Lambda/p))$ ratios as a function of $\sqrt{s_{NN}}$. Searches for multi-strange hypernuclei (${}^5_{\Lambda\Lambda}$H and ${}^6_{\Lambda\Lambda}$He) make appealing physics goals. However, further simulations are required to determine if these measurements will be feasible with the expected integrated luminosity.

3.4.3 FXT Beam Request

The FXT program at STAR will employ energies that have already been developed for the BES-I program. Details of the sequence of energies is listed in the tables in the Executive Summary. Table 10 shows $\sqrt{s_{\rm NN}}$ set-up for the collider and the center of mass energy for FXT. Also listed is the kinetic energy of the beam as some other facilties use this describe the energy system. The center of mass rapidity is listed as this gives insight to the acceptance of STAR for a given energy, and the expected chemical potential demonstrates the region of the QCD phase diagram to be studied.

Table 10: Collider set-up and fixed-target center-of-mass energies ($\sqrt{s_{\rm NN}}$), projectile kinetic energies (AGeV), center-of-mass rapidity offset ($y_{\rm CM}$), baryon chemical potentials (μ_B) for the proposed fixed-target program.

Collider $\sqrt{s_{\rm NN}}$	FXT $\sqrt{s_{\rm NN}}$	Kinetic (AGeV)	Rapidity $y_{\rm CM}$	μ_B (MeV)
62.4	7.7	30.3	2.10	420
39	6.2	18.6	1.87	487
27	5.2	12.6	1.68	541
19.6	4.5	8.9	1.52	589
14.5	3.9	6.3	1.37	633
11.5	3.5	4.8	1.25	666
9.1	3.2	3.6	1.13	699
7.7	3.0	2.9	1.05	721

4 Status of STAR Upgrades for Runs 18 and 19

STAR has three detector upgrades planned for Run 18 and/or Run 19: the inner Time Projection Chamber (iTPC), Event Plane Detector (EPD) and endcap Time of Flight (eTOF). The iTPC will increase the acceptance of the TPC, it will improve the dE/dx resolution, and will allow tracks to be reconstructed down to p_T of ~60 MeV/c. The EPD will replace the BBC as a minimum-bias trigger detector and will allow forward measurements of both the centrality and event plane. The eTOF will be installed on one side of STAR, which will extend PID capabilities at forward rapidities. These upgrades are described in more detail below, and their overall location in the STAR detector is shown in Fig. 50.

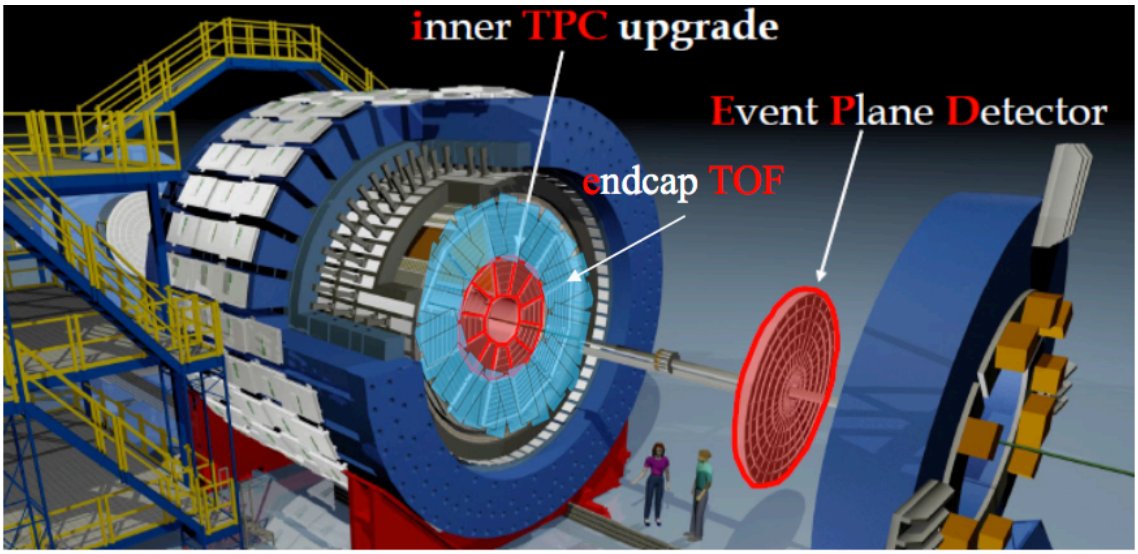

Figure 50: Rendering of the STAR detector with the upgrades highlighted in red. The EPD and iTPC are symmetric in STAR whereas the eTOF is only on the east side.

The acceptance and the limit in p_T vs. rapidity for different species using PID from either the iTPC, bTOF or eTOF are show in Fig. 51.

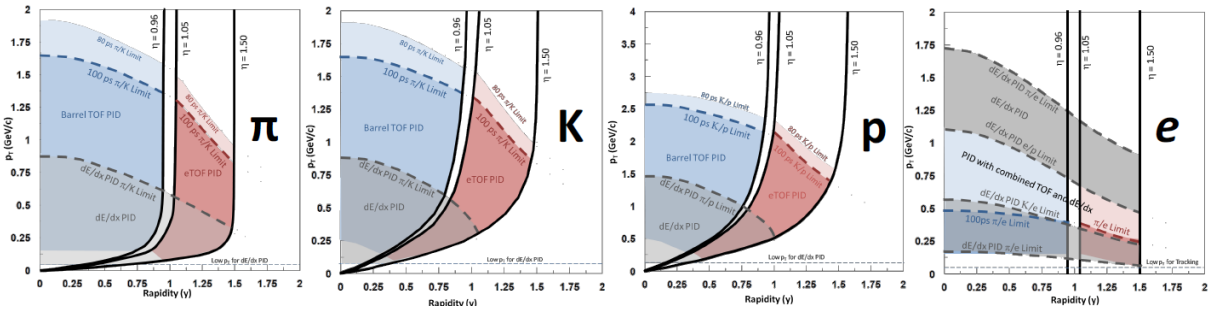

Figure 51: Acceptance and PID limits for π, K, proton and electrons with STAR instrumented with iTPC and eTOF.

These upgrades are scheduled to be phased into STAR over the next two shutdown periods. Table 11 summarizes when prototypes and final installation will take place.

STAR is also engaged in a R&D program that will enable a future Forward Physics program after the completion of the BES-II program. This program has been outlined in

the proposal[156] also submitted to the PAC as part of future opportunities with STAR at RHIC.

Year	iTPC	EPD	eTOF
2017	-	1/8 installed	1 prototype
2018	One sector	**Full Installation**	3 modules at one sector
2019	**Full Installation**	**Full Installation**	**Full Installation**

Table 11: Timeline for installation of upgrades.

4.1 The inner TPC (iTPC)

The inner sectors of the STAR TPC are being upgraded to increase the segmentation on the inner pad planes. These improvements will extend the capabilities of STAR in many ways. Most significantly, the enhanced tracking at small angles relative to the beamline will expand the TPC acceptance out to pseudorapidity $|\eta| \leq 1.5$, compared to the current limitation of $|\eta| \leq 1$. Furthermore, the detector will have better acceptance for tracks with low transverse momentum down to 60 MeV/c, as well as better resolution in both momentum ($\delta p/p$ improvement $\sim$15%) at larger momenta, and dE/dx improvement of ($\sim$25%) for full length tracks. These changes will enable the collection of data that is critical to the physics mission for the BES-II. In addition, the improved dE/dx and momentum resolution, as well as tracking at higher pseudorapidity, provide the foundation for the success of the eTOF. The iTPC project is described in detail in the Technical Design Report [107].

The iTPC upgrade was given go ahead for construction in March 2016 following a director's review to ensure that the project could complete for the Run 19. The project had a DOE NP Technical Cost Schedule and Management review in September 2016, and progress and status is now presented monthly to the DOE. The overall schedule is still tight, but significant progress has been made. The project consists of two parts: Construction of new sectors and their MWPC readout, and development of new electronics based on the SAMPA chip doubling the number of channels per FEE card. The Al strong backs and the pad planes have all been manufactured according to specifications. Prototype bonding of pad planes to the sectors, a high precision task, has been done at LBNL, and the production phase has been entered. Two prototypes of the MWPC have been constructed at Shandong University, Jinan, China (SDU) and tested. The first step in the production is to bond the pad plane with high accuracy to the strong back. Figure 52 (left) shows the second bonded pad plane to an Al sector at LBNL. Subsequent steps align the side mount that will hold the wire planes with high precision, then bare sectors are shipped to SDU where wire winding and mounting takes place. Figure 52 (right) shows a complete sector built at SDU. This sector has been tested for gain and resolution using a ^{55}Fe source. Figure 53 shows a result of such measurements on a single wire. A good resolution of 20% FWHM, better than requirements, is observed.

Significant progress has also been made with the electronics. Two prototype FEE cards with the prototype MWP2 SAMPA chip have been installed, with special adapter cards, on one of the innermost rows of the STAR TPC for the Run 17 (p+p at $\sqrt{s}$ = 500 GeV). So far the electronics are performing well. It is planned to have electronics available for a full sector test on the floor, and installed for the STAR Run 18.

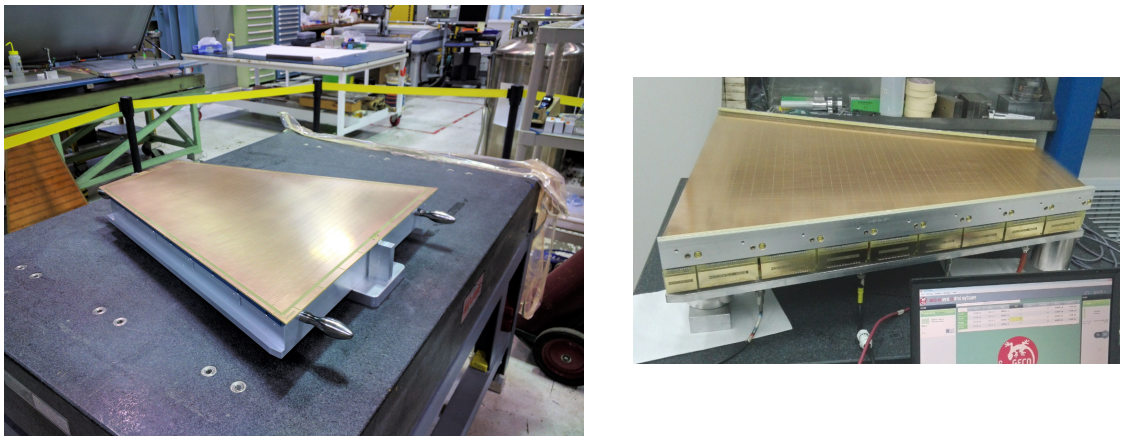

Figure 52: (left) pad plane bonded to Al strongback. (right) Complete prototype sector.

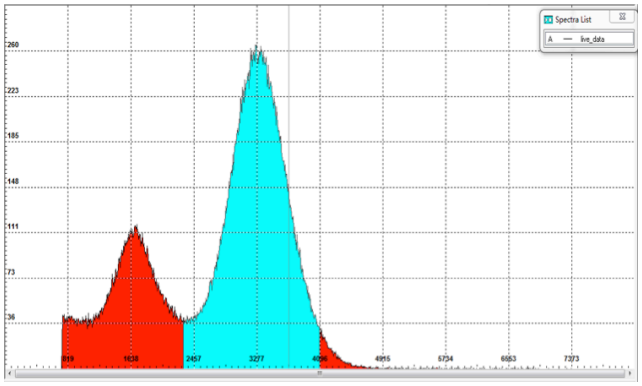

Figure 53: Energy spectrum from a ^{55}Fe source on a single anode wire of a prototype iTPC sector showing the main and escape peaks.

The current production and testing of the full complement of inner sectors is scheduled to complete in mid-summer of 2018, and the installation and testing period will take 10 months.

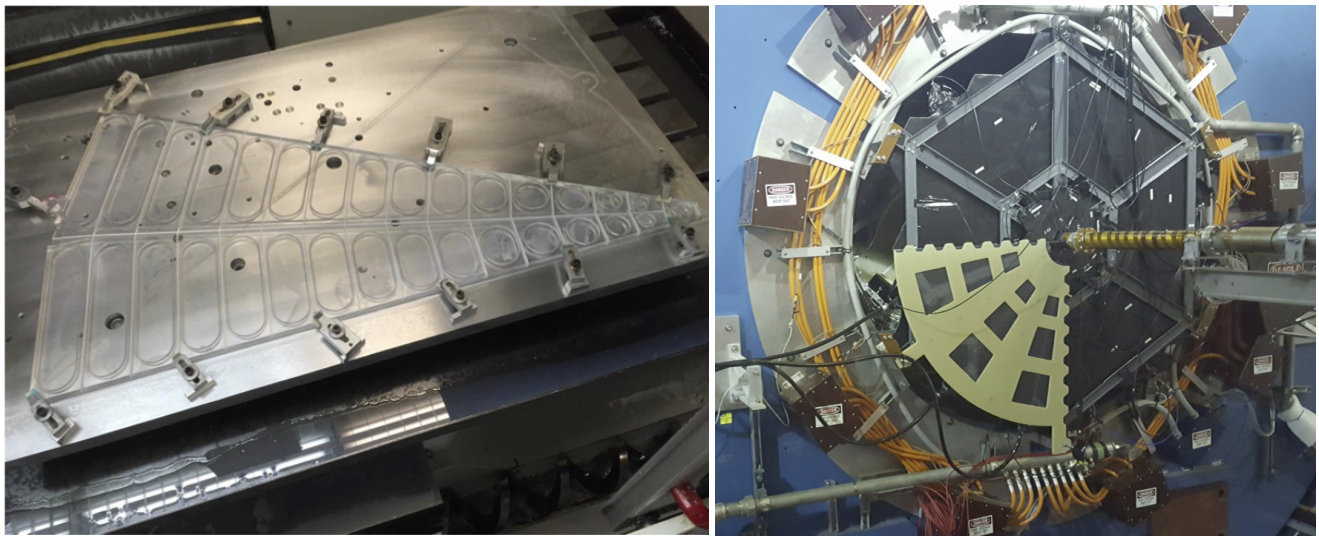

Figure 54: (left) The first EPD super-sector under construction at OSU. (right) The 1/8th detector installed for Run 17.

4.2 The Event Plane Detector (EPD)

A new, dedicated Event Plane, centrality, and trigger Detector (EPD) will be installed in the forward direction of STAR for Run 18 and beyond. This new detector will have pseudorapidity acceptance of $2.1 < |\eta| < 5.1$ with high radial and azimuthal segmentation. The EPD will allow the centrality and the event plane to be measured in the forward region, reducing the systematics due to autocorrelations from mid-rapidity analyses. The baseline detector design utilizes scintillator plastic, wavelength-shifting fibers and silicon photomultipliers (SiPMs).

The EPD consists of two disks that will be placed on either side of the STAR interaction region, in the current location of the Beam-Beam Counter (BBC). The EPD will be the same size as BBC, as it is required to sit in the same space within the STAR experiment. The EPD will extend from a radius of 4.5 cm (1.77 in) to 90 cm (35.4 in) and will be located at z = ± 375 cm. The design allows for the EPD to be installed downstream from the BBC as a contingency for Run 18, or for the EPD to be installed instead of the BBC which is the preferred mode of operation. The EPD scintillator is 1.2 cm thick and has 12 azimuthal segments, spanning an angle of 30°, which we give the label "super-sector". There are 16 segments in η, with the innermost tile spanning the entire super-sector and the other tiles dividing it in two for better ϕ resolution. This results in a total of 744 channels for the two EPD disks. The tile size was designed such that the probability of multiple particle hits in the same tile would be less than 10% at $\sqrt{s_{NN}}$ = 19.6 GeV, based on $dN/d\eta$ measurements from PHOBOS. This increases to 65% for Au+Au collisions at 200 GeV. More details on the EPD design and expected performance can be found here [104].

Two EPD prototypes were built and tested in Runs 15 and 16. These successful tests showed that the detector could be integrated with the STAR electronics, and that the basic design principles were sound. This allowed construction of the EPD to begin; the machining of the first of the super sectors can be seen in Figure 54. Shown on the right of Fig. 54 is the 1/8 of the total detector (1/4 of a single disk) installed downstream from the BBC in Run 17 for commissioning. This commissioning run will allow the quantification of the performance of the detector in terms of efficiency, and timing and test different trigger algorithms.

The first results of the EPD can be seen in Fig. 56, which shows the ADC spectra for three different tiles: 1, 3 and 9. Since the lowest numbered tiles are closest to the beam pipe, this shows data for a variety of η positions. These curves were fit by Landau distributions, which had a 1, 2 and 3 MIP contributions. For each, an average number of 50 photons per MIP was determined, with an uncertainty on the level of 40%. In Fig. 55, on the left shows the hits in the different EPD tiles when selecting for a signal in a single BBC tile. The BBC tile in question is shown as a red circle, and a good correlation between the hits can be seen. On the right of this figure is a time difference between a hit arriving at a BBC tile and an overlapping EPD tile. The width of this distribution, roughly 3.5 ns, is a convolution of the timing resolution of the EPD and of the BBC.

One of the important tests for the Run 17 commissioning of the EPD was to benchmark its performance versus the BBC. In Figure 55 the hits in the EPD tile-by-tile is shown for collisions where there was a hit in BBC PMT channel 4, and no hit in BBC PMT 5. As expected, this selection lights up the EPD tile directly behind the BBC tile, showing a nice correlation. There were no additional selections made on the collisions, so the vertex of the collision was only constrained by the STAR minimum bias trigger.

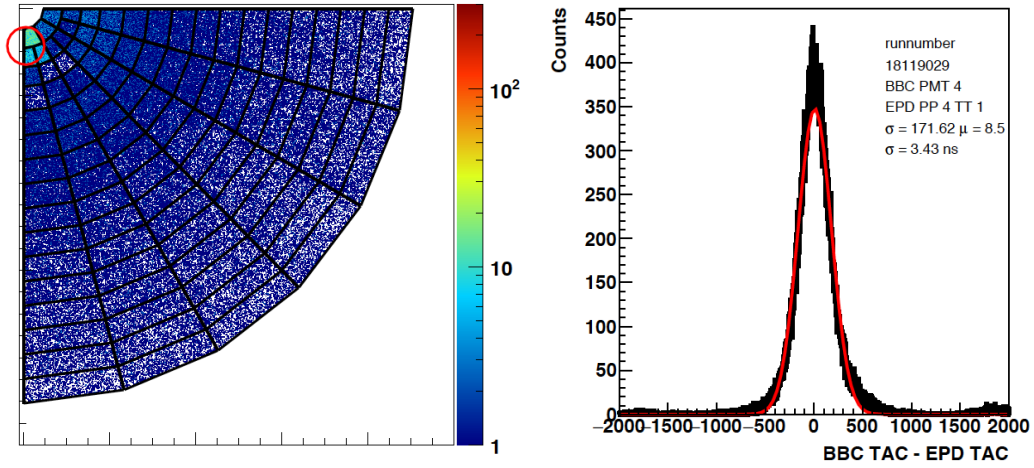

Figure 55: (left) Plot of the hits in different EPD tiles selecting collisions where there is a hit in BBC PMT channel 4, shown as an overlapping red circle, and no hit in the other BBC small tiles that overlap with the EPD. On the right is the time difference between a hit in an EPD tile and a hit in the overlapping BBC tile, the width of this curve is the convolution of the time resolution for both detectors.

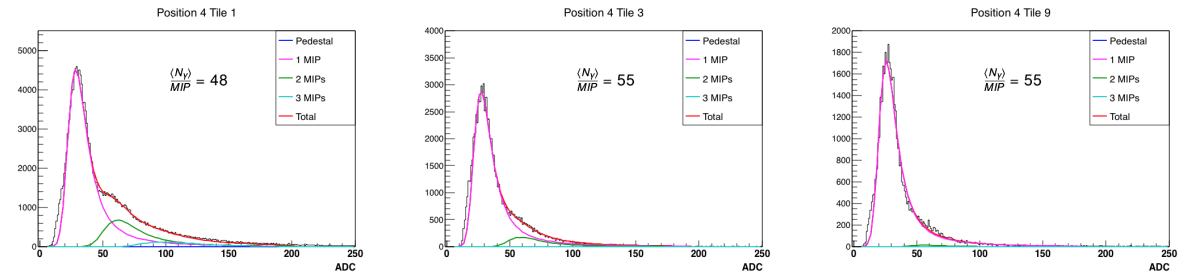

Figure 56: ADC spectra for three different tiles, from the highest η on the left to the mid-η region on the right. A valid TAC signal was required for each of these tiles.

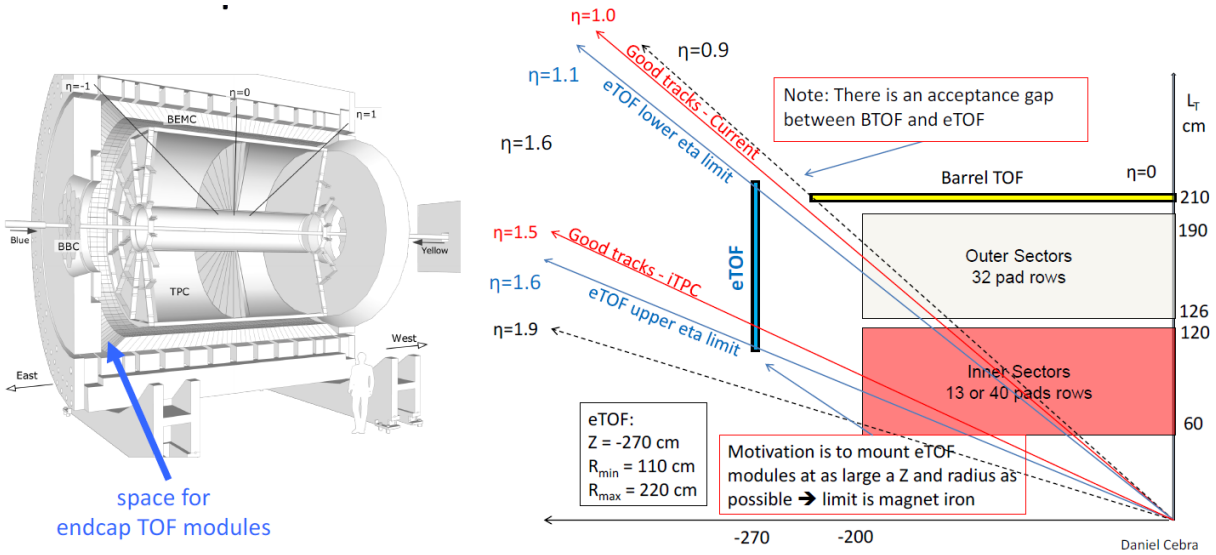

Figure 57: Placement and acceptance diagrams for the eTOF.

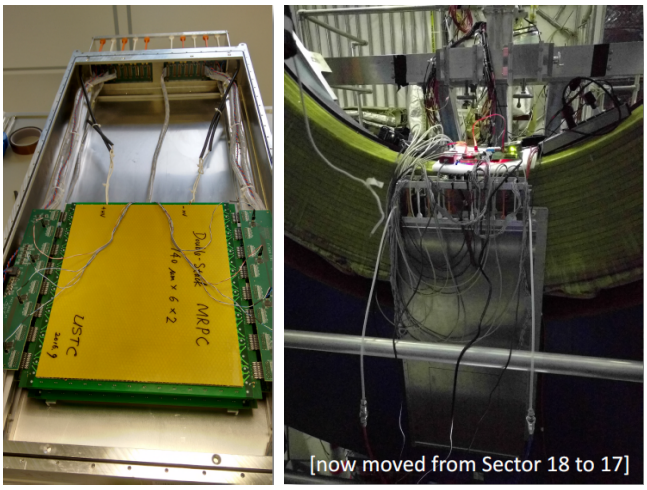

Figure 58: (left) The prototype module. (right) The installed module with services.

4.3 The endcap TOF (eTOF)

The STAR Collaboration and institutions from the CBM Collaboration: Heidelberg, Darmstadt, Tsinghua, CCNU, and USTC have agreed to install an endcap time-of-fight upgrade (eTOF) in the STAR detector for the BES-II program in 2019 and 2020. The improvements in acceptance and PID and the physics goals of the upgrade are described in detail in Ref. [108], and the technical description of the modules in Ref. [157]. The eTOF will be installed at the east end of STAR in the small gap between the poletip and the TPC; behind the readout electronics as depicted in the left cartoon of Fig. 57. The right hand side of the same figure illustrates how the coverage in η is much improved with the combination of the iTPC and the eTOF.

A prototype eTOF module was installed behind one TPC sector for the ongoing run with the aim of testing the module in the RHIC environment, and integrating the CBM electronics with the STAR trigger and DAQ systems. This initial test will be followed with the installation prior to Run 18 of 3 modules to cover a full TPC sector. Figure 58 shows the MRPC eTOF module and the cabled up installed module.

5 Computing at STAR

5.1 STAR Workflow and Computing Resources

The STAR computing resources available for data processing currently consists primarily of the resources available at the RHIC Computing Facility (RACF) where at most 14,000 CPU slots are allocated to the data production campaign and the handling of data calibration tasks. The rest of the RACF slots are reserved for user analysis jobs, with the overflow directed to opportunistically utilize unused resources from other experiments. While the number of slots used by the data production and calibration workflows is ∼14,000 on average across the year, this number fluctuates lower during RHIC run time (when additional resources are taken for near real-time incremental calibrations) and increases just after major conferences in the field (when user's jobs slightly deplete).

In the early years of RHIC STAR had the resources to produce a given run's data 2.2-2.4 times within a year after the data was taken. Severe resource constraints in past years have forced the STAR Software and Computing team (S&C) to first reduce this number to a conservative 1.2-1.5 passes. Additionally, because the computational resources have not grown for several years, S&C no longer constrains the 1.5 passes to fit with a year's schedule. Instead, planning is made and expressed in terms of delayed production and scheduled physics priorities. Processing time needed for calibration varies from 1.5 to 3 months depending on whether the collision system is well known and all calibrations follow expectations, or if the studied system is novel (i.e. isobars in Run 18) and/or presents a unique new challenge such as unusually high luminosity, additional distortions or inclusion of a new detector sub-system. Typically, the scheduling of the production of quality high priority physics datasets may occur as soon as 2 months after a given run ends. To reach this goal, incremental calibrations are performed during the run (both online and offline), allowing for rapid turn-around at run's end. At that time sub-system software leaders and designated calibration experts work on bootstrapping and correlating all calibration pieces, including particle identification.

To increase resource availability, the S&C team has attempted to make use of the unused cycles on the PHENIX farm. This effort was suggested by the 2016 PAC and initially believed to have the potential to deliver a boost of +12.5% in processing time over a period of 6 months. Unfortunately STAR jobs submitted to PHENIX resources are only allowed to run for a fraction of the time needed to complete the full reconstruction of all events in a single DAQ file (jobs running long are killed and must be re-submitted). As a result, each job must be split into N sub-tasks that can be completed within the allowed time. This then raised the need to ensure all N sub-tasks are completed before merging back into a set of single output files. Setting aside the bookkeeping complication this implies, it is worth noting that the RACF production system (a.k.a. CRS) did not allow the restoration of the same DAQ files multiple times on multiple nodes while simultaneously minimizing tape access. This issue was reported and fixed in early 2017 and we were then in a position to test the feasibility of this new paradigm. Ultimately, for reasons detailed below, we feel this mechanism is not a productive path forward for STAR.

First, such workflow does not allow our jobs to be transient. The transient property of our jobs (whether running on the Grid or on STAR's own resources) is the fact that for all jobs, data is transferred to the compute element (asynchronously to the use of the CPU cycle) and the output produced locally then moved as soon as possible to tape storage (HPSS). The data appears only temporarily onto central disk storage (for purposes of

data sanity validation and cataloging) and the storage freed as soon as this automated process has completed. Such workflow adaptation has allowed us to survive the increase in production demands over the past years under a flat-storage budget scenario. But in the case of using the PHEHIX resources, storage needs to be available to store the output of N sub-tasks before they are merged into single files and moved to tape. For this to happen, additional storage is required and we estimate we need to have at least a day worth of central storage ($\sim$15 TB) to support this mechanism. Second, the long pause of our incomplete jobs (i.e. waiting for any of the N sub-tasks from a single job to finish) would, upon resuming, restore again the raw data causing an increase access to tape resources (hence risking increase of wear-and-tear) – this has shown to be detrimental to media lifetime. Finally, due to the very unpredictable nature of the availability of those resources (if PHENIX starts a production campaign, we may be out of the queue for a long time), this does not allow for providing our Physics Working Groups (PWG) with accurate estimates of when data productions would be delivered. To add to those bookkeeping, technical and organizational issues, at the time of writing this report the unused PHENIX resources have dropped to an 8% average over the past year. Meanwhile STAR's user analysis jobs, more adapted to short time slots, continue to harvest up to 17.25% of unused PHENIX's resources.

More predictable resources provide a fast path for scientific discovery while minimizing human investment. The S&C team has therefore continued to look and focus on additional resources outside the RACF. Those include the farm available at our Dubna institutions (at most 1,000 slots or +7% increase of predictable CPU cycles) and the less-standard use of High performance Computing (HPC) resources at the NERSC/Cori Supercomputing leadership facility. In 2016, STAR demonstrated the first high efficiency use of HPC resources for real-data production in the Nuclear and Particle Physics communities. This work was presented at the CHEP 2016 conference and showed an end-to-end workflow efficiency nearing 95% and the STAR collaboration was subsequently provided with an allocation of 25 Million hours.

Those remote resources are primarily used to provide a boost to the data production workflows (lower priority datasets are moved to Dubna with predictable estimated time to delivery) or used to provide additional production passes realigning with a community standard number of production passes far greater than 1. While our workflow efficiencies are very high, for planning purposes, we will use a 93% compounded efficiency where the compounded efficiency is defined as the product of the resource utilization efficiency (our ability to saturate the available slots) times the application's run-time efficiency.

5.2 Datasets overview and Prioritization process

The STAR data production plan is an evolving prioritization process based on input from the PWG conveners, the readiness of data calibrations and the software development time invested to deliver high precision physics. Analysis of past challenges revealed that the lack of live storage was proving to be a show-stopper to either stage the MuDsts and/or store the PWG's private analysis tree necessary to pursue their analysis and publications in a timely manner. Therefore, STAR had vested interests in developing newer and more compact analysis data format and in 2016, the Data Summary file format known as a "MuDST" (micro-DST) was complemented by an emerging format known as "picoDST". The picoDST related code workflows were since integrated in the STAR framework after a successful software peer-review process verifying code compliance. The PWG were actively polled for readiness and adaptation of ongoing analysis to the new file format

Year	Species	Total #of events (M)	%tage events completed	Estimate time to delivery (months)	%tage time to completion
16	[summary]	**9126.46**	**49.44**	**3.74**	**60.45**
	Au+Au 200GeV	6543.26	63.25	3.22	
	d+Au 200GeV	1181.10	31.58	0.44	
	d+Au 62GeV	357.91	0.00	0.08	
	d+Au 39GeV	642.12	0.00	0.08	
	d+Au 20GeV	402.08	0.00	$<$ 0.08	
15	[summary]	**10997.37**	**84.31**	**0.75**	**86.89**
	p+p 200GeV	6329.66	93.70	*0.19*	
	p+Au 200GeV	3647.70	78.76	0.33	
	p+Al 200GeV	1015.11	45.61	0.24	
	fixed Target	4.76	100.00	0.00	
14	[summary]	**6718.09**	**84.66**	**0.39**	**90.85**
	Au+Au 200GeV	5045.59	96.79	*0.22*	
	He3+Au 200GeV	1260.30	31.29	0.18	
	Au+Au 14.6GeV	412.20	99.38	*0.00*	

Table 12: Production summary for the Run 14, 15 and 16 datasets. The first row within a block shows the summary for a given year, while the subsequent rows provide information broken down by species. Lighter species being processed faster, the %tage completion is given in both number of events and relative time for the year summary. Text in *italics* indicates productions considered completed (note %tages less then 100 reflect the fact that some jobs may have not been recorded).

and the picoDST was extended for a wider acceptance across all physics topics. All 2016 datasets produced both micro-DSTs and picoDSTs and STAR is in the process of converting a few selected past datasets to the new more compact format. With 10 CPU cores, we estimated we needed 4 days to convert 6 TB worth of MuDST to picoDST. The full conversion of all datasets produced prior to the 2016 data production campaign would therefore require allocation of resources. As all conversion tasks look alike (and each job is short), this may be a place where STAR can effectively utilize unused PHENIX cycles, although this remains untested at this time.

Table 12 shows the status of data production during the past year, including % completed in number of events and total time estimated to wrap up production for a given run. Since lighter systems require less time to process for an equivalent number of events, it is to be noted that we are nearly complete for Run 14, 86.9% complete for the Run 15 datasets and $\sim$ 4 months away from completing all Run 16 datasets production.

5.3 Production computing resource estimates for the purpose of the BUR

Table 13 provides estimates for DAQ, data summary ("MuDST" and "picoDST") dataset sizes for the past, not yet fully produced, RHIC runs as well as the proposed colliding species in this BUR along with the estimated time needed to process those datasets considering the currently available resources. As discussed earlier, we base our plan on 1.5 production passes, a need for time for calibration processing, and an overall workflow

Year	Species	RAW space [PB]	MuDST space [PB]	picoDST [PB]	MuDST total space [PB]	picoDST total space [PB]	Total reco time, 1.5 passes [m]	Required (+calib time) [m]
					8.5	***1.31***		
16	200 GeV Au+Au	6.96	4.88	0.70	**9.28**	**2.09**	14.04	**15.20**
	200 GeV d+Au	0.43	0.53	0.08			1.04	
	Low energy d+Au	0.14	0.06	0.01			0.12	
17	500 GeV p+p	4.85	2.65	0.41	**12.53**	**2.59**	11.4	**15.34**
	Low energy Au+Au (27 GeV or 1/2 time 62 GeV)	1.2	0.6	0.09			1.45	
18	27 GeV Au+Au	0.32	0.22	0.03	**12.76**	**2.82**	0.42	**6.48**
	200 GeV Ru+Ru	0.88	0.65	0.10			1.53	
	200 GeV Zr+Zr	0.88	0.65	0.10			1.53	
19/20	Various Au+Au BES-II	0.35	0.25	0.04	**13.01**	**2.86**	1.45	**2.95**

Table 13: Required resource summary table broken down by year and collision systems. The columns indicating "total space required" are the cumulative space necessary to keep all current datasets available for analysis (in the prefixed specific format) as well as future year's dataset in distributed storage. The first row indicates the current space usage and in italic, the usage if all datasets currently available to data analyzers (in MuDST format) would be converted to the picoDST format. Production time estimates are given in months time assuming the 2017 RACF farm size.

efficiency of 93%. The MuDST to picoDST size ratio varies from 7 (measured for all Run 16 data productions) to 6.5 (planned addition of information that would cover for most Physics Working Group's need).

The Run 18 plan as well as a Run 19 or Run 19+20 combined plan are represented for an overview of the current BUR. For the purpose of resource planning, those two scenarios (19 or 19+20 combined) provide little differences to the overall conclusion so they are grouped together.

A few conclusions emerge. First and foremost, considering the remaining time outlines in Table 12 for finishing all data production, we see that in $\sim$ 5 months' time all past data would be produced at least once (providing priorities are given to data production). With an end of the Run 17 currently planned by summer and considering a needed 2.5 months calibration time for those samples, STAR is unlikely to suffer major delays in delivering datasets from Run 17 flagged as high priority. As indicated earlier, this projection may change depending on upcoming conferences and the usage of the farm for user analysis (but the fluctuation is at most a 12% effect). Year 17 will offer the same challenge as year 16 – an extended allocation on facilities such as NERSC/Cori, or a boost of resources from one of our remote Grid facilities if available, would once again absorb the excess resources needed to fit the production campaign within a year's time. But the out years are light on resource demands and do not seem to raise significant computing resource challenges. For the BES-II datasets especially, and providing the organization of our calibration is focused during the run, STAR could even consider a near real-time processing of the data.

Particular attention is needed on columns 6&7 of Table 13 however. Those columns represent the total cumulated storage needed to keep all previously stored datasets and future datasets under the MuDST and picoDST assumption respectively. They illustrate the storage challenge the collaboration has been facing. STAR's distributed storage capacity of 8.6 PBytes is currently occupied at its near maximum capacity of 8.5 PBytes. To make the datasets from 2016 and future years available to STAR analyzers, it is clear that the only path is a full push forward toward the use of the picoDST format. Since the picoDST columns shows we would need at maximum $\sim$3 PB of storage, it is conceivable that only some of the past datasets (and not all) would be converted to the new format. The discussion of which past datasets should be converted has started within the PWG.

A final note that for data collection and run plans beyond the scope of this BUR, the storage limitations will remain a constraint limiting both the data production workflow we could envision and our ability to keep most physics datasets available for physics analysis. Large datasets, without complementary CPU resources, would further see a delay in the delivery of physics samples.

References

[1] L. Adamczyk et al. Measurement of the cross section and longitudinal double-spin asymmetry for dijet production in polarized pp collisions at $\sqrt{s} = 200$ GeV. *Phys. Rev. D*, 95:071103, Apr 2017.

[2] Daniel de Florian, Rodolfo Sassot, Marco Stratmann, and Werner Vogelsang. Evidence for polarization of gluons in the proton. *Phys. Rev. Lett.*, 113:012001, Jul 2014.

[3] Emanuele R. Nocera, Richard D. Ball, Stefano Forte, Giovanni Ridolfi, and Juan Rojo. A first unbiased global determination of polarized PDFs and their uncertainties. *Nucl. Phys.*, B887:276–308, 2014.

[4] Ting Lin. Longitudinal Double-Spin Asymmetries for Forward Di-jet Production in Polarized pp Collisions at $\sqrt{s} = 200$ GeV.

[5] L. Adamczyk et al. Measurement of longitudinal spin asymmetries for weak boson production in polarized proton-proton collisions atRHIC. *Phys. Rev. Lett.*, 113:072301, 2014.

[6] E. C. Aschenauer et al. The RHIC Spin Program: Achievements and Future Opportunities. 2013.

[7] Jincheng Mei. Transverse Spin Transfer to Λ and $\bar{\Lambda}$ Hyperons in Transversely Polarized p+p Collisions at $\sqrt{s} = 200$ GeV at RHIC.

[8] B. I. Abelev et al. Longitudinal spin transfer to Λ and $\overline{\Lambda}$ hyperons in polarized proton-proton collisions at $\sqrt{s} = 200$GeV. *Phys. Rev. D*, 80:111102, 2009.

[9] M. Aghasyan et al. First measurement of transverse-spin-dependent azimuthal asymmetries in the Drell-Yan process. 2017.

[10] L. Adamczyk et al. Measurement of the transverse single-spin asymmetry in $p^{\uparrow}+p \to W^{\pm}/Z^0$ at RHIC. *Phys. Rev. Lett.*, 116(13):132301, 2016.

[11] Zhong-Bo Kang and Jian-Wei Qiu. Testing the Time-Reversal Modified Universality of the Sivers Function. *Phys. Rev. Lett.*, 103:172001, 2009.

[12] Miguel G. Echevarria, Ahmad Idilbi, Zhong-Bo Kang, and Ivan Vitev. QCD Evolution of the Sivers Asymmetry. *Phys. Rev.*, D89:074013, 2014.

[13] L. Adamczyk et al. Measurement of D^0 azimuthal anisotropy at mid-rapidity in Au+Au collisions at $\sqrt{s_{NN}} = 200\,\text{GeV}$. *accepted by Phys. Rev. Lett.*, 2017.

[14] V. Greco, C. M. Ko, and P. Levai. Parton coalescence at RHIC. *Phys. Rev.*, C68:034904, 2003.

[15] V. Greco, C. M. Ko, and P. Levai. Parton coalescence and anti-proton/pion anomaly at RHIC. *Phys. Rev. Lett.*, 90:202302, 2003.

[16] Yongseok Oh, Che Ming Ko, Su Houng Lee, and Shigehiro Yasui. Heavy baryon/meson ratios in relativistic heavy ion collisions. *Phys. Rev.*, C79:044905, 2009.

[17] Min He, Rainer J. Fries, and Ralf Rapp. $\mathbf{D_s}$-Meson as Quantitative Probe of Diffusion and Hadronization in Nuclear Collisions. *Phys. Rev. Lett.*, 110(11):112301, 2013.

[18] L. Adamczyk et al. Energy dependence of J/ψ production in Au+Au collisions at $\sqrt{s_{NN}}$ = 39, 62.4 and 200 GeV. 2016.

[19] M. C. Abreu et al. Evidence for deconfinement of quarks and gluons from the J/ψ suppression pattern measured in Pb + Pb collisions at the CERN SPS. *Phys. Lett.*, B477:28–36, 2000.

[20] Betty Bezverkhny Abelev et al. Centrality, rapidity and transverse momentum dependence of J/ψ suppression in Pb-Pb collisions at $\sqrt{s_{\rm NN}}$=2.76 TeV. *Phys. Lett.*, B734:314–327, 2014.

[21] Xingbo Zhao and Ralf Rapp. Charmonium in Medium: From Correlators to Experiment. *Phys. Rev.*, C82:064905, 2010.

[22] Xingbo Zhao and Ralf Rapp. Medium Modifications and Production of Charmonia at LHC. *Nucl. Phys.*, A859:114–125, 2011.

[23] Yun-peng Liu, Zhen Qu, Nu Xu, and Peng-fei Zhuang. J/ψ Transverse Momentum Distribution in High Energy Nuclear Collisions at RHIC. *Phys. Lett.*, B678:72–76, 2009.

[24] Kai Zhou, Nu Xu, Zhe Xu, and Pengfei Zhuang. Medium effects on charmonium production at ultrarelativistic energies available at the CERN Large Hadron Collider. *Phys. Rev.*, C89(5):054911, 2014.

[25] Yan-Qing Ma and Raju Venugopalan. Comprehensive Description of J/ψ Production in Proton-Proton Collisions at Collider Energies. *Phys. Rev. Lett.*, 113(19):192301, 2014.

[26] Hua-Sheng Shao, Hao Han, Yan-Qing Ma, Ce Meng, Yu-Jie Zhang, and Kuang-Ta Chao. Yields and polarizations of prompt J/ψ and $\psi(2S)$ production in hadronic collisions. *JHEP*, 05:103, 2015.

[27] Yan-Qing Ma and Ramona Vogt. Quarkonium Production in an Improved Color Evaporation Model. *Phys. Rev.*, D94(11):114029, 2016.

[28] E. G. Ferreiro, F. Fleuret, J. P. Lansberg, N. Matagne, and A. Rakotozafindrabe. Centrality, Rapidity, and Transverse-Momentum Dependence of Gluon Shadowing and Antishadowing on J/ψ Production in dAu Collisions at $\sqrt{s}$=200 GeV. *Few Body Syst.*, 53:27–36, 2012.

[29] Jean-Philippe Lansberg and Hua-Sheng Shao. Towards an automated tool to evaluate the impact of the nuclear modification of the gluon density on quarkonium, D and B meson production in proton–nucleus collisions. *Eur. Phys. J.*, C77(1):1, 2017.

[30] Jaroslav Adam et al. Measurement of an excess in the yield of J/ψ at very low $p_{\rm T}$ in Pb-Pb collisions at $\sqrt{s_{\rm NN}}$ = 2.76 TeV. *Phys. Rev. Lett.*, 116(22):222301, 2016.

[31] L. Adamczyk et al. Suppression of Υ production in d+Au and Au+Au collisions at $\sqrt{s_{NN}}$=200 GeV. *Phys. Lett.*, B735:127–137, 2014. [Erratum: Phys. Lett.B743,537(2015)].

[32] L. Adamczyk et al. Di-Jet Imbalance Measurements at $\sqrt{s_{NN}} = 200$ GeV at STAR. 2016.

[33] L. Adamczyk et al. Measurements of jet quenching with semi-inclusive hadron+jet distributions in Au+Au collisions at $\sqrt{s_{NN}} = 200$ GeV. 2017.

[34] I. Arsene et al. Quark–gluon plasma and color glass condensate at RHIC? The perspective from the BRAHMS experiment. *Nucl. Phys.*, A757:1–27, 2005.

[35] B. B. Back et al. The PHOBOS perspective on discoveries at RHIC. *Nucl. Phys.*, A757:28–101, 2005.

[36] J. Adams et al. Experimental and theoretical challenges in the search for the quark–gluon plasma: The STAR Collaboration's critical assessment of the evidence from RHIC collisions. *Nucl. Phys.*, A757:102–183, 2005.

[37] K. Adcox et al. Formation of dense partonic matter in relativistic nucleus–nucleus collisions at RHIC: Experimental evaluation by the PHENIX Collaboration. *Nucl. Phys.*, A757:184–283, 2005.

[38] L. Adamczyk et al. Bulk Properties of the Medium Produced in Relativistic Heavy-Ion Collisions from the Beam Energy Scan Program. 2017.

[39] B.-J. Schaefer and J. Wambach. Susceptibilities near the QCD (tri)critical point. *Phys. Rev.*, D75:085015, 2007.

[40] D. H. Rischke et al. The Phase transition to the quark-gluon plasma and its effects on hydrodynamic flow. *Heavy Ion Phys.*, 1:309–322, 1995.

[41] H. Stöcker. Collective flow signals the quark–gluon plasma. *Nucl. Phys.*, A750:121–147, 2005.

[42] Arthur M. Poskanzer and S. A. Voloshin. Methods for analyzing anisotropic flow in relativistic nuclear collisions. *Phys. Rev.*, C58:1671–1678, 1998.

[43] L. Adamczyk et al. Beam-energy dependence of the directed flow of protons, antiprotons, and pions in Au+Au collisions. *Phys. Rev. Lett.*, 112:162301, 2014.

[44] Yasushi Nara, Akira Ohnishi, and Horst Stoecker. Directed flow as a signature of the softest point of the equation of state in QCD matter. 2016.

[45] J. Steinheimer, J. Auvinen, H. Petersen, M. Bleicher, and H. Stöcker. Examination of directed flow as a signal for a phase transition in relativistic nuclear collisions. *Phys. Rev. C*, 89:054913, May 2014.

[46] V. P. Konchakovski, W. Cassing, Yu. B. Ivanov, and V. D. Toneev. Examination of the directed flow puzzle in heavy-ion collisions. *Phys. Rev. C*, 90:014903, Jul 2014.

[47] W. Cassing, V. P. Konchakovski, A. Palmese, V. D. Toneev, and E. L. Bratkovskaya. . *EPJ Web Conf.C*, 95:01004, 2014.

[48] P. Shanmuganathan. Beam-energy and centrality dependence of directed flow of identified particles. *Nucl. Phys.*, A956:260–263, 2016.

[49] S. Singha. Directed flow of Λ, $\bar{\Lambda}$, $K^{\pm}$, K^0_s, and ϕ mesons from Beam Energy Scan Au+Au collisions using the STAR experiment. *J. Phys.: Conf. Ser.*, 779:012066, 2017.

[50] S. Bass et al. Microscopic models for ultrarelativistic heavy ion collisions. *Prog. Part. Nucl. Phys.*, 41:255–369, 1998.

[51] Y. Hirono, M. Hongo, and T. Hirono. Estimation of the electric conductivity of the quark gluon plasma via asymmetric heavy-ion collision. *Phys. Rev.*, C90:021903, 2014.

[52] V. Voronyuk, V. D. Toneev, S. A. Voloshin, and W. Cassing. Charge-dependent directed flow in asymmetric nuclear collisions. *Phys. Rev.*, C90:064903, 2014.

[53] L. Adamczyk et al. Charge-dependent directed flow in Cu+Au collisions at $\sqrt{s_{NN}}$=200 GeV. *Phys. Rev. Lett.*, 118:012301, 2017.

[54] L. Adamczyk et al. Centrality and transverse momentum dependence of elliptic flow of multistrange hadrons and ϕ meson in Au+Au collisions at $\sqrt{s_{NN}}$=200 GeV. *Phys. Rev. Lett.*, 116:062301, 2016.

[55] S. Takeuchi, K. Murase, T. Hirano, P. Huovinen, and Y. Nara. Effects of hadronic rescattering on multistrange hadrons in high-energy nuclear collisions. *Phys. Rev.*, C92:044907, 2015.

[56] Z.-W. Lin, C. M. Ko, B.-A. Li, B. Zhang, and S. Pal. Multiphase transport model for relativistic heavy ion collisions. *Phys. Rev.*, C72:064901, 2005.

[57] L. Adamczyk et al. Observation of an Energy-Dependent Difference in Elliptic Flow between Particles and Antiparticles in Relativistic Heavy Ion Collisions. *Phys.Rev.Lett.*, 110(14):142301, 2013.

[58] L. Adamczyk et al. Centrality dependence of identified particle elliptic flow in relativistic heavy ion collisions at $\sqrt{s_{NN}}$ = 7.7-62.4 GeV. *Phys. Rev.*, C93:014907, 2016.

[59] L. Adamczyk et al. Measurement of elliptic flow of light nuclei at $\sqrt{s_{NN}}$ = 200, 62.4, 39, 27, 19.6m 11.5 and 7.7 GeV at RHIC. *Phys. Rev.*, C94:034908, 2016.

[60] A. Andronic, P. Braun-Munzinger, J. Stachel, and H. Stocker. Production of light nuclei, hypernuclei and their antiparticles in relativistic nuclear collisions. *Phys. Lett.*, B697:203–207, 2011.

[61] Adam Bzdak and Derek Teaney. Longitudinal fluctuations of the fireball density in heavy-ion collisions. *Phys. Rev.*, C87:024906, 2013.

[62] J. Jia, S. Radhakrishnan, and M. Zhou. Forward-backward multiplicity fluctuation and longitudinal harmonics in high-energy nuclear collisions. *Phys. Rev.*, C93:044905, 2016.

[63] S. Jowzaee. Rapidity correlations in the RHIC Beam Energy Scan Data (in publishing). *Nucl. Phys.*, A, 2017.

[64] Liang Z.-T. and X.-N. Wang. Globally polarized quark-gluon plasma in noncentral A+A collisions. *Phys. Rev. Lett.*, 94:102301, 2005.

[65] F. Becattini, F. Piccinini, and J. Rizzo. Angular momentum conservation in heavy ion collisions at very high energy. *Phys. Rev.*, C77:024906, 2008.

[66] L.-G. Pang, H. Petersen, Q. Wang, and X.-N. Wang. Vortical fluid and Λ spin correlations in high-energy heavy-ion collisions. *Phys. Rev. Lett.*, 117:192301, 2016.

[67] L. Adamczyk et al. Global Λ hyperon polarization in nuclear collisions: evidence for the most vortical fluid.

[68] B. I. Abelev et al. Global polarization measurement in Au+Au collisions. *Phys. Rev.*, C76:024915, 2007.

[69] F. Becattini, I. Karpenko, M. A. Lisa, I. Upsal, and S. A. Voloshin. Global hyperon polarization at local thermodynamic equilibrium with vorticity, magnetic field and feed-down.

[70] Dmitri Kharzeev. Parity violation in hot QCD: Why it can happen, and how to look for it. *Phys. Lett.*, B633:260–264, 2006.

[71] Dmitri E. Kharzeev, Larry D. McLerran, and Harmen J. Warringa. The Effects of topological charge change in heavy ion collisions: 'Event by event P and CP violation'. *Nucl. Phys.*, A803:227–253, 2008.

[72] Sergei A. Voloshin. Parity violation in hot QCD: How to detect it. *Phys. Rev.*, C70:057901, 2004.

[73] Scott Pratt, Soeren Schlichting, and Sean Gavin. Effects of Momentum Conservation and Flow on Angular Correlations at RHIC. *Phys. Rev.*, C84:024909, 2011.

[74] Adam Bzdak, Volker Koch, and Jinfeng Liao. Charge-Dependent Correlations in Relativistic Heavy Ion Collisions and the Chiral Magnetic Effect. *Lect. Notes Phys.*, 871:503–536, 2013.

[75] Soren Schlichting and Scott Pratt. Charge conservation at energies available at the BNL Relativistic Heavy Ion Collider and contributions to local parity violation observables. *Phys. Rev.*, C83:014913, 2011.

[76] B. I. Abelev et al. Azimuthal Charged-Particle Correlations and Possible Local Strong Parity Violation. *Phys. Rev. Lett.*, 103:251601, 2009.

[77] B. I. Abelev et al. Observation of charge-dependent azimuthal correlations and possible local strong parity violation in heavy ion collisions. *Phys. Rev.*, C81:054908, 2010.

[78] Gang Wang. Search for Chiral Magnetic Effects in High-Energy Nuclear Collisions. *Nucl. Phys.*, A904-905:248c–255c, 2013.

[79] L. Adamczyk et al. Fluctuations of charge separation perpendicular to the event plane and local parity violation in $\sqrt{s_{NN}} = 200$ GeV Au+Au collisions at the BNL Relativistic Heavy Ion Collider. *Phys. Rev.*, C88(6):064911, 2013.

[80] L. Adamczyk et al. Beam-energy dependence of charge separation along the magnetic field in Au+Au collisions at RHIC. *Phys. Rev. Lett.*, 113:052302, 2014.

[81] Betty Abelev et al. Charge separation relative to the reaction plane in Pb-Pb collisions at $\sqrt{s_{NN}} = 2.76$ TeV. *Phys. Rev. Lett.*, 110(1):012301, 2013.

[82] Shuzhe Shi and Jinfeng Liao. private communication.

[83] Vardan Khachatryan et al. Observation of charge-dependent azimuthal correlations in pPb collisions and its implication for the search for the chiral magnetic effect. *Phys. Rev. Lett.*, 2016. [Phys. Rev. Lett.118,122301(2017)].

[84] Prithwish Tribedy. Disentangling flow and signals of Chiral Magnetic Effect in U+U, Au+Au and p+Au collisions. In *26th International Conference on Ultrarelativistic Nucleus-Nucleus Collisions (Quark Matter 2017) Chicago,Illinois, USA, February 6-11, 2017*, 2017.

[85] Sandeep Chatterjee and Prithwish Tribedy. Separation of flow from the chiral magnetic effect in U + U collisions using spectator asymmetry. *Phys. Rev.*, C92(1):011902, 2015.

[86] A. Adare et al. Transverse energy production and charged-particle multiplicity at midrapidity in various systems from $\sqrt{s_{NN}} = 7.7$ to 200 GeV. *Phys. Rev.*, C93(2):024901, 2016.

[87] D. T. Son and Ariel R. Zhitnitsky. Quantum anomalies in dense matter. *Phys. Rev.*, D70:074018, 2004.

[88] Max A. Metlitski and Ariel R. Zhitnitsky. Anomalous axion interactions and topological currents in dense matter. *Phys. Rev.*, D72:045011, 2005.

[89] Yannis Burnier, Dmitri E. Kharzeev, Jinfeng Liao, and Ho-Ung Yee. Chiral magnetic wave at finite baryon density and the electric quadrupole moment of quark-gluon plasma in heavy ion collisions. *Phys. Rev. Lett.*, 107:052303, 2011.

[90] G. M. Newman. Anomalous hydrodynamics. *JHEP*, 01:158, 2006.

[91] L. Adamczyk et al. Observation of charge asymmetry dependence of pion elliptic flow and the possible chiral magnetic wave in heavy-ion collisions. *Phys. Rev. Lett.*, 114(25):252302, 2015.

[92] Adam Bzdak and Piotr Bozek. Contributions to the event-by-event charge asymmetry dependence for the elliptic flow of pi^+ and pi^- in heavy-ion collisions. *Phys. Lett.*, B726:239–243, 2013.

[93] Qi-Ye Shou. Charge asymmetry dependence of π/K anisotropic flow in $Au + Au$ and $U + U$ collisions at RHIC. *Nucl. Phys.*, A931:758–762, 2014.

[94] Yoshitaka Hatta, Akihiko Monnai, and Bo-Wen Xiao. Elliptic flow difference of charged pions in heavy-ion collisions. *Nucl. Phys.*, A947:155–160, 2016.

[95] Sergei A. Voloshin. Testing the Chiral Magnetic Effect with Central U+U collisions. *Phys. Rev. Lett.*, 105:172301, 2010.

[96] Wei-Tian Deng, Xu-Guang Huang, Guo-Liang Ma, and Gang Wang. Test the chiral magnetic effect with isobaric collisions. *Phys. Rev.*, C94:041901, 2016.

[97] S. Raman, C. W. G. Nestor, Jr, and P. Tikkanen. Transition probability from the ground to the first-excited 2+ state of even-even nu clides. *Atom. Data Nucl. Data Tabl.*, 78:1–128, 2001.

[98] B. Pritychenko, M. Birch, B. Singh, and M. Horoi. Tables of E2 Transition Probabilities from the first 2^+ States in Even-Even Nuclei. *Atom. Data Nucl. Data Tabl.*, 107:1, 2016.

[99] P. Moller, J. R. Nix, W. D. Myers, and W. J. Swiatecki. Nuclear ground state masses and deformations. *Atom. Data Nucl. Data Tabl.*, 59:185–381, 1995.

[100] A. Hennig et al. Collective excitations of Ru96 by means of (p,p′ γ) experiments. *Phys. Rev.*, C92(6):064317, 2015.

[101] Tomoaki Togashi, Yusuke Tsunoda, Takaharu Otsuka, and Noritaka Shimizu. Quantum Phase Transition in the Shape of Zr isotopes. *Phys. Rev. Lett.*, 117(17):172502, 2016.

[102] B. I. Abelev et al. Observation of Two-source Interference in the Photoproduction Reaction Au Au —> Au Au rho0. *Phys. Rev. Lett.*, 102:112301, 2009.

[103] J. Adams et al. Production of e+ e- pairs accompanied by nuclear dissociation in ultra-peripheral heavy ion collision. *Phys. Rev.*, C70:031902, 2004.

[104] STAR. SN0666 - An Event Plane Detector for STAR.

[105] N. Brambilla et al. Heavy quarkonium: progress, puzzles, and opportunities. *Eur. Phys. J.*, C71:1534, 2011.

[106] STAR. SN0598- Studying the Phase Diagram of QCD Matter at RHIC. March 2014. STAR Note SN0598.

[107] STAR. SN0644 - Technical Design Report for the iTPC Upgrade.

[108] Physics Program for the STAR/CBM eTOF Upgrade. 2016.

[109] L. Adamczyk et al. Beam-Energy Dependence of the Directed Flow of Protons, Antiprotons, and Pions in Au+Au Collisions. *Phys. Rev. Lett.*, 112(16):162301, 2014.

[110] Y. Aoki, Z. Fodor, S. D. Katz, and K. K. Szabo. The QCD transition temperature: Results with physical masses in the continuum limit. *Phys. Lett.*, B643:46–54, 2006.

[111] Y. Aoki, D. Endrodi, Z. Fodor, S. D. Katz, and K. K. Szabo. The order of the quantum chromodynamics transition predicted by the standard model of particle physics. *Nature*, 443:675–678, 2006.

[112] M. A. Stephanov. Non-Gaussian fluctuations near the QCD critical point. *Phys. Rev. Lett.*, 102:032301, 2009.

[113] Masayuki Asakawa, Shinji Ejiri, and Masakiyo Kitazawa. Third moments of conserved charges as probes of QCD phase structure. *Phys. Rev. Lett.*, 103:262301, 2009.

[114] M. A. Stephanov. On the sign of kurtosis near the QCD critical point. *Phys. Rev. Lett.*, 107:052301, 2011.

[115] L. Adamczyk et al. Energy Dependence of Moments of Net-proton Multiplicity Distributions at RHIC. *Phys. Rev. Lett.*, 112:032302, 2014.

[116] F. Karsch and K. Redlich. Probing freeze-out conditions in heavy ion collisions with moments of charge fluctuations. *Phys. Lett.*, B695:136–142, 2011.

[117] M. Bleicher et al. Relativistic hadron-hadron collisions in the ultra-relativistic quantum molecular dynamics model. *J. Phys.*, G25:1859, 1999.

[118] Adam Bzdak and Volker Koch. Acceptance corrections to net baryon and net charge cumulants. *Phys. Rev.*, C86:044904, 2012.

[119] J. Brachmann, S. Soff, A. Dumitru, Horst Stoecker, J. A. Maruhn, W. Greiner, L. V. Bravina, and D. H. Rischke. Antiflow of nucleons at the softest point of the EoS. *Phys. Rev.*, C61:024909, 2000.

[120] B. Mohanty and N. Xu. Probe the QCD phase diagram with phi-mesons in high energy nuclear collisions. *J. Phys.*, G36:064022, 2009.

[121] Md. Nasim, Bedangadas Mohanty, and Nu Xu. Elliptic flow of ϕ mesons as a sensitive probe for the onset of the deconfinement transition in high energy heavy-ion collisions. *Phys. Rev.*, C87(1):014903, 2013.

[122] B. I. Abelev et al. Energy and system size dependence of phi meson production in Cu+Cu and Au+Au collisions. *Phys. Lett.*, B673:183–191, 2009.

[123] R. Rapp. Signatures of thermal dilepton radiation at RHIC. *Phys. Rev.*, C63:054907, 2001.

[124] Ralf Rapp and Hendrik van Hees. Thermal Dileptons as Fireball Thermometer and Chronometer. *Phys. Lett.*, B753:586–590, 2016.

[125] Paul M. Hohler and Ralf Rapp. Is ρ-Meson Melting Compatible with Chiral Restoration? *Phys. Lett.*, B731:103–109, 2014.

[126] R. V. Gavai and S. Gupta. QCD at finite chemical potential with six time slices. *Phys. Rev.*, D78:114503, 2008.

[127] T. Anticic et al. Centrality dependence of proton and antiproton spectra in Pb+Pb collisions at 40A GeV and 158A GeV measured at the CERN SPS. *Phys. Rev.*, C83:014901, 2011.

[128] Jean Cleymans. Recent developments around chemical equilibrium. *J. Phys.*, G37:094015, 2010.

[129] B. I. Abelev et al. Systematic measurements of identified particle spectra in pp, d+Au, and Au+Au collisions at the STAR detector. *Phys. Rev.*, C79:034909, 2009.

[130] D. Cebra, S. G. Brovko, C. E. Flores, B. A. Haag, and J. L. Klay. Coulomb effect in Au+Au and Pb+Pb collisions as a function of collision energy. 2014.

[131] L. Adamczyk et al. Dielectron Mass Spectra from Au+Au Collisions at $\sqrt{s_{\rm NN}}$ = 200 GeV. *Phys. Rev. Lett.*, 113(2):022301, 2014. [Addendum: Phys. Rev. Lett.113,no.4,049903(2014)].

[132] L. Adamczyk et al. Measurements of Dielectron Production in Au+Au Collisions at $\sqrt{s_{\rm NN}}$ = 200 GeV from the STAR Experiment. *Phys. Rev.*, C92(2):024912, 2015.

[133] T. C. Huang et al. Muon Identification with Muon Telescope Detector at the STAR Experiment. *Nucl. Instrum. Meth.*, A833:88–93, 2016.

[134] Jan Steinheimer and Jorgen Randrup. Spinodal amplification of density fluctuations in fluid-dynamical simulations of relativistic nuclear collisions. *Phys. Rev. Lett.*, 109:212301, 2012.

[135] C. Alt et al. Pion and kaon production in central Pb + Pb collisions at 20-A and 30-A-GeV: Evidence for the onset of deconfinement. *Phys. Rev.*, C77:024903, 2008.

[136] L. Adamczyk et al. Beam-Energy Dependence of Charge Balance Functions from Au+Au Collisions at RHIC. Submitted Jul. 13, 2015.

[137] P. Chung et al. Near threshold production of the multistrange xi- hyperon. *Phys. Rev. Lett.*, 91:202301, 2003.

[138] J. Adams et al. Multi-strange baryon elliptic flow in Au + Au collisions at s(NN)**(1/2) = 200-GeV. *Phys. Rev. Lett.*, 95:122301, 2005.

[139] Scott Pratt. General Charge Balance Functions, A Tool for Studying the Chemical Evolution of the Quark-Gluon Plasma. *Phys. Rev.*, C85:014904, 2012.

[140] Horst Stoecker. Collective flow signals the quark gluon plasma. *Nucl. Phys.*, A750:121–147, 2005.

[141] H. Liu et al. Sideward flow in Au + Au collisions between 2-A-GeV and 8-A-GeV. *Phys. Rev. Lett.*, 84:5488–5492, 2000.

[142] Michael Annan Lisa, Ulrich W. Heinz, and Urs Achim Wiedemann. Tilted pion sources from azimuthally sensitive HBT interferometry. *Phys. Lett.*, B489:287–292, 2000.

[143] M. A. Lisa et al. Azimuthal dependence of pion interferometry at the AGS. *Phys. Lett.*, B496:1–8, 2000.

[144] M. A. Lisa, E. Frodermann, G. Graef, M. Mitrovski, E. Mount, H. Petersen, and M. Bleicher. Shape analysis of strongly-interacting systems: The Heavy ion case. *New J. Phys.*, 13:065006, 2011.

[145] Michael Annan Lisa, Scott Pratt, Ron Soltz, and Urs Wiedemann. Femtoscopy in relativistic heavy ion collisions. *Ann. Rev. Nucl. Part. Sci.*, 55:357–402, 2005.

[146] Hannah Petersen and Marcus Bleicher. Longitudinal flow and onset of deconfinement. *PoS*, CPOD2006:025, 2006.

[147] C. Pinkenburg et al. Elliptic flow: Transition from out-of-plane to in-plane emission in Au + Au collisions. *Phys. Rev. Lett.*, 83:1295–1298, 1999.

[148] G. Baym and P. Braun-Munzinger. *Nucl. Phys. A*, 610:286c, 1996.

[149] Ralf Rapp and Hendrik van Hees. Thermal dileptons as fireball thermometer and chronometer. *Physics Letters B*, 753:586 – 590, 2016.

[150] S. V. Afanasiev et al. Event-by-event fluctuations of the kaon to pion ratio in central Pb + Pb collisions at 158-GeV per nucleon. *Phys. Rev. Lett.*, 86:1965–1969, 2001.

[151] L. Adamczyk et al. Beam energy dependence of moments of the net-charge multiplicity distributions in Au+Au collisions at RHIC. *Phys. Rev. Lett.*, 113:092301, 2014.

[152] A. Adare et al. Measurement of higher cumulants of net-charge multiplicity distributions in Au+Au collisions at $\sqrt{s_{NN}} = 7.7 - 200$ GeV. 2015.

[153] Yataro Sekido and Harry Elliot. *Early History of Cosmic Ray Studies*, page 323. D. Reidel Publishing Company, 1985.

[154] B. I. Abelev. Observation of an Antimatter Hypernucleus. *Science*, 328:58–62, 2010.

[155] H. Agakishiev et al. Observation of the antimatter helium-4 nucleus. *Nature*, 473:353, 2011. [Erratum: Nature475,412(2011)].

[156] STAR. SN0648 - The STAR Forward Calorimeter System and Forward Tracking System beyond BES-II.

[157] Norbert Herrmann, editor. *Technical Design Report for the CBM Time-of-Flight System (TOF)*. GSI, Darmstadt, 2014.